Zentrale Einrichtung Elektronenmikroskopie

(Leiter Prof. Dr. Paul Walther)

Universität Ulm

Novel electron tomographic methods to study the three dimensional keratin filament networks of pancreatic canceroid cells

Dissertation

Zur Erlangung des Doktorgrades (Dr. biol. hum.)

An der Medizinischen Fakultät der Universität Ulm

vorgelegt von Michaela Maria Sailer

Ulm 2010

Amtierender Dekan der Medizinischen Fakultät:
Prof. Dr. Thomas Wirth

Erstgutachter:
Prof. Dr. Paul Walther, Zentrale Einrichtung Elektronenmikroskopie, Universität Ulm

Zweitgutachter:
Dr. Michael Beil, Innere Medizin I, Uniklinik Ulm

Datum der Promotion:
27.05.2011

Die Arbeiten im Rahmen der vorgelegten Dissertation wurden in der Zentralen Einrichtung Elektronenmikroskopie der Universität Ulm durchgeführt und von Prof. Dr. Paul Walther betreut.

Contents

1. Summary

The aim of this study was to expand already existing methods for two dimensional data acquisition of the keratin filament network with the goal to obtain three dimensional datasets. For this purpose different novel electron microscopical methods were applied and compared. Thin sections of high-pressure-frozen and freeze-substituted Panc1 cells (by Katharina Höhn) were analyzed using high and low voltage STEM at accelerating voltages of 300 and 30 kV. Using this approach, it was not possible to unambiguously track the thin filaments, since they are hidden by other cell compounds. Therefore, these cell compounds were removed by an extraction method using Triton X-100, so that only the keratin filaments remained. These samples were then analyzed simultaneously in STEM and SEM mode. Since keratin filaments have a diameter of only about 12 nm, the volume-dependent STEM signal did not yield enough contrast of the thin filaments. The signal to noise ratio of filaments compard to unextracted cell compounds was, however, increased, when imaging with the surface-dependent secondary electron signal, which is strong from the thin filaments. As a new approach, tomograms using the secondary electron signal were recorded in the SEM at an accelerating voltage of 5 kV by tilting the sample with 2° step size to a maximum tilt of -60° to +60°. For this purpose a special pre-tilted holder was developed. The resulting image series was reconstructed into a three-dimensional model and could then be analyzed with statistical methods.

To investigate whether artifact formation occurred during critical point drying, control samples were prepared using a freeze drying protocol. When comparing freeze dried keratin filament networks with critical point dried samples, no differences in network characteristics could be found. In both cases the filaments showed similar branching and directional distribution. We conclude, therefore, that the keratin filament network is more robust than the actin network and thus less affected by disturbances during extraction, fixation, dehydration and drying.

2. Introduction

2.1 The Pancreas

The pancreas is a gland organ belonging to the digestive and endocrine system of vertebrates. It is located in the retroperitoneum and has both endocrine and exocrine functions. The smaller endocrine part is producing several hormones such as insulin or glucagon, whereas the bigger exocrine part secrets digestive enzymes. Injury or diseases of the pancreas are potentially severe and very often leads to death. Typical examples of these diseases are diabetes mellitus, pancreatitis and, of course, pancreatic cancer.

Pancreatic cancer is considered as one of the most fatal types of cancer and one of the main reasons of cancer death. When pancreatic cancer is diagnosed, more than 80% of patients already suffer from either locally advanced or metastatic disease, leading to a high mortality rate. The majority of patients die within one year after diagnosis, only 1-4% of all patients with adenocarcinoma of the pancreas survive five years (Ellenrieder et al. 1999). The cause of this rapid death is the aggressive growth of the cancer and the expansion into adjacent tissue, as well as early lymphatic and hematogenous metastasis. For this reason, the control of cell motility is a first step towards developing more effective diagnostic and therapeutic strategies (Ellenrieder et al., 1999).

2.2 Keratin Filaments

Vertebrate cells contain three types of fibrous individual biopolymers: microtubules, actin filaments and intermediate filaments (Janmey et al., 1991). These filament types form the cytoskeleton, a network of proteins in the cytoplasm, responsible for different cell properties and functions. Whereas microtubules are involved in mitosis and intracellular transport, actin and intermediate filaments play an important role concerning mechanical stabilization, shape, and active movement of the cell as a whole. In contrast to microtubules and actin filaments, intermediate filaments are more flexible and more stable when exposed to shear forces and have a better resistance to breakage (Herrmann & Aebi, 2004). Furthermore, unlike actin and microtubules which are polymers of single types of protein, intermediate filaments are composed of more than 50 different proteins, expressed in different types of cells. Also,

intermediate filaments are insoluble in physiological buffers and resistant to extraction with detergents such as 1% Triton X-100.

Keratin filaments are the most complex group of the intermediate filament system and the characteristic part in epithelial cells and cells of epithelial origin. They form a self assembling scaffold, defining the shape and the mechanical properties of a cell (Herrmann et al., 2003), such as cell motility, elasticity and protection against mechanical stress. Keratins are obligate heteropolymers of type I (CK9-20; acidic) and type II (CK1-8; neutral/basic) keratin polypeptides (Hatzfeld & Franke, 1985) forming coiled-coil molecules, which then associate in shifted antiparallel tetramers. The tetramers then assemble to build a unit length filament (ulf) and at last, several ulfs then are assembled end to end and represent the final intermediate filament with a diameter of about 10 nm (Figure 1).

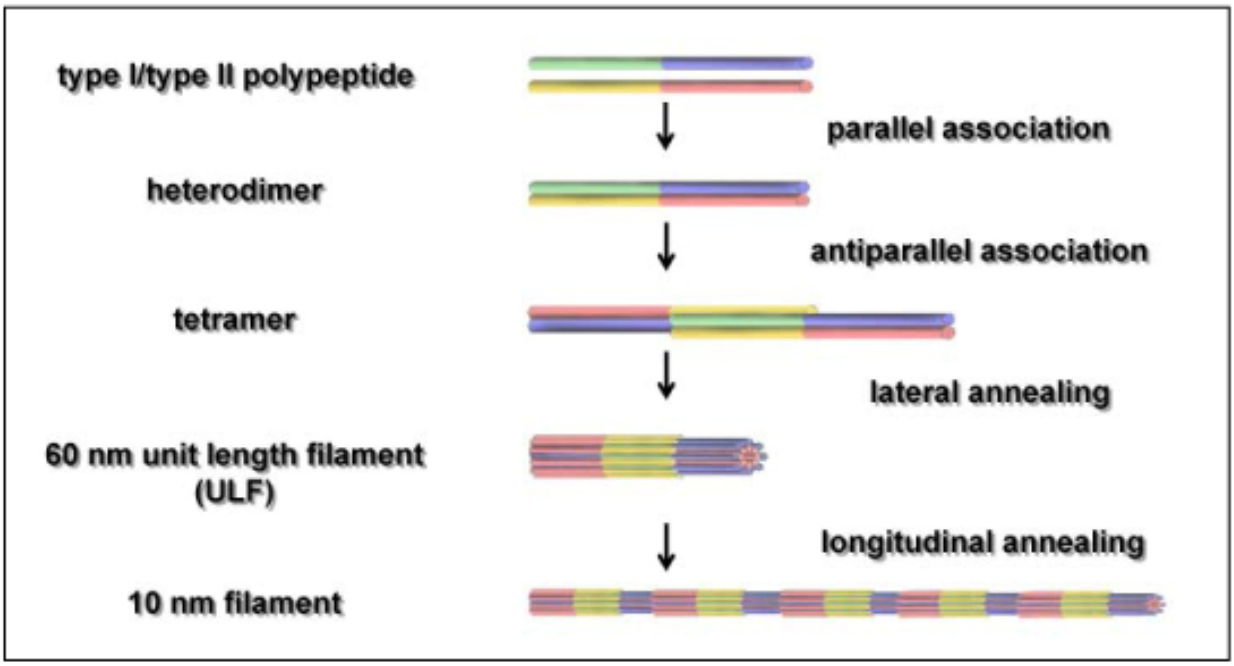

Fig. 1: *Schematic drawing of the assembling of keratin intermediate filaments (kindly provided by: Prof. Dr. med. Rudolf Leube, Institute for Molecular and Cellulare Anatomy, Aachen, reproduced with permission)*

The small keratin monomers can be regulated posttranslational by i.e. phosphorylation and glycosylation, which influences the network architecture (Coulombe & Omary, 2002; Beil et al., 2005). CK8 and CK18 are the basic keratin forms expressed in simple epithelia (Fuchs & Weber, 1994) and their tumors, such as pancreatic carcinoma.

2.3 Electron Microscopy

Electron microscopy works with electrons to create a magnified image of a sample. According to Abbé's equation (Abbé, 1873), the wavelength of light limits the resolution of a conventional light microscope to about 200 nm. Since the wavelength of accelerated electrons (between 5keV and 300 keV, as used in this study) is several orders of magnitude smaller, an electron microscope can achieve resolutions of better than 0.1nm (the present "resolution record" of our Titan is about 0.06 nm). In modern life science microscopy different types of electron microscopes are applied, they all consist of an electron gun, special electromagnetic lenses, a vacuum system, and a sample holder. They differentiate mainly in beam projection and signal collection: in a classical transmission electron microscope (TEM), the beam projection is very similar to a light microscope and electrons are transmitted through the sample. For this purpose the sample needs to be very thin to keep the amount of inelastically scattered electrons small. Inelastically scattered electrons would cause chromatic aberration when passing through the projective lenses. The scanning electron microscope (SEM) in contrast, produces images by scanning the usually bulk sample with a focused electron beam. This process causes the release of different kind of electrons and other signals from the sample that can be collected with adequate detectors, and an image is formed on a display screen by integrating the signal over time. Usually the signal is formed by usage of the secondary electrons, low energetic electrons released from the sample by inelastic scattering events of the electron beam, and the back scattered electrons, beam electrons reflected from the sample by elastic and inelastic scattering. The scanning transmission electron microscope (STEM) is a type of a TEM, where the electron beam is focused to a narrow spot, scanning a thin sample in a raster similar to the SEM. In this type of microscope, however, the electrons passing through the sample are used for image formation. STEM images are usually formed by collecting scattered electrons using an annular dark-field detector.

Due to the vacuum and the electron beam in the electron microscopical column, biological samples with high water content need to be prepared by special methods before they can be analyzed. Generally, it is necessary to fix the specimen so that it is immobilized, and to dehydrate it, since water would evaporate in the vacuum and interfere with the electron beam. Furthermore, it is important to improve electrical conductivity to prevent charge-up by the electron beam. Contrast can be enhanced by staining or coating with heavy metals. The preparation steps vary depending on the type of microscope used. There are two main

preparation methods, chemical fixation and cryo fixation, each with different advantages and disadvantages making the structures of interest amenable to the electron beam. With the chemical fixation the molecules of a sample are connected irreversibly (covalent) among themselves by a fixative, e.g. glutaraldehyde. This method is the older one and it is easier to accomplish. But since penetration of the fixatives into the sample is relatively slow (seconds to minutes) the ultrastructure of the sample might change during fixation (Szczesny et al., 1994). After fixation the samples are dehydrated with alcohol and then critical point dried. The cryo fixation method is based on freezing a sample with a thickness up to 200 µm in milliseconds with liquid nitrogen under high pressure (about 2000 bar; Moor and Riehle, 1968). With this method it is supposed to conserve the natural state of the sample much better than with chemical fixation (Walther, 2003). After freezing the water in the samples is substituted by acetone with solved heavy metals for contrasting media and the sample is embedded in resin.

Former electron microscopical experiments with keratin filaments have shown that they need to be prepared in a special way before they can be imaged. All lipids and soluble proteins have to be removed from the cells, so that only the keratin filament network remains. Otherwise it is nearly impossible to analyze the whole network and to track single filaments. For this purpose a special extracting method, partially based on the protocol of Svitkina & Borisy (1998) can be used. Hereby all cell components except the keratin filaments are washed out by using Triton X-100. The keratin filaments are resistant to extraction with detergents such as 1% Triton X-100.

Samples undergo strong disturbances during the different preparation steps. Particularly, in all steps where chemicals are used, like in extraction, chemical fixation or freeze substitution, there always is the risk, that the sample's natural state might be changed (Walther, 2008). All of this could of course also happen to the keratin filament network, in a way that it no longer conforms to the original state in the living cell. But there are also other possibilities, where artifact formation could arise: Ris (1985) described artifact formation ("microtrabecular lattice") in actin filaments caused by traces of water or ethanol remaining in the sample during critical point drying, which led to distortions and fusions of fibers. Small (2010) made similar experiences concerning actin filaments in lamellipodia. Furthermore, Resch et al. (2002) showed that actin filaments fracture and branch artificially during critical point drying.

Keratin filament networks are three-dimensional, as all biological structures. The most adequate way for the three-dimensional recording of a small biological structure is electron tomography. For this purpose, a sample is tilted gradually and images are recorded under different tilt angles. (Self-shadowing of the sample as well as the increasing path length of the electrons at high tilts limits tilting to about ± 70°.) This procedure results in an image series which can be back projected into a three-dimensional model (Hoppe et al., 1974). A few years ago scanning transmission electron microscope (STEM) tomography, a new imaging technology based on TEM tomography, was introduced (Midgley et al., 2001; Midgley & Dunin-Borkowski, 2009). This technique provides better contrast and signal-to noise ratio than bright field-TEM tomography (Yakushevska et al., 2007) and can be applied to thicker sections up to 1 µm (Aoyama et al., 2008; Hohmann-Marriott et al., 2009).

2.4 Aim of the studies

In previous studies of our group image analysis of the keratin filament network was based on two-dimensional electron microscopical images (Beil et al., 2005, 2006). These analyses were restricted to the peripheral very flat parts of the adherent cells, where the network is almost planar. In other parts of the cell closer to the nucleus, however, the keratin network exhibits a three-dimensional form. Consequently, the aim of this promotion work was to develop, improve and apply novel electron microscopical methods allowing the three-dimensional description of the keratin filament network at a nanometer scale. The results were compared with data obtained by other methods and possible artifact formation could be critically reviewed.

3. Results

3.1 Novel electron tomographic methods for three-dimensional analysis of keratin filament networks

Authors: **M. Sailer**, K. Höhn, S. Lück, V. Schmidt, M. Beil and P. Walther
Microscopy and Microanalysis (2010) Vol. 16, pp. 462-471.

The keratin filament network of human pancreatic cancer cells was analyzed using different electron microscopical methods. In STEM-tomography of semi thin sections of high pressure frozen and freeze substituted Panc1 human pancreatic cancer cells it was very difficult to track the filaments in three dimensions. Better results were obtained when the cells were extracted using a pre-fixation extraction method partially based on the protocol of Svitkina & Borisy (1998), where most of the cell components are removed and only the finely woven keratin filaments remain. The same area of a cell was then imaged simultaneously in an SEM at 30 kV using the transmission dark field signal and the secondary electron signal. The contrast of the thin filaments was considerably higher in the secondary electron image than in the transmission image. The electrons used for contrast formation in dark field transmission imaging are scattered in function of the mass density, which is low in these thin filaments. Therefore, contrast in STEM is low and the filaments are almost vanishing beside unextracted cell compounds having a larger volume and hence high contrast. The secondary electron signal, however, is a function of the surface area exposed to the electron beam (Seiler, 1967). The secondary electron emission of the filaments is high, because they have a large surface compared to the volume (Figure 2). Basing on these results we decided to use the secondary electron and not the transmission signal for SEM tomography. Tomograms were recorded at 5 kV and all single images of one tilt series were back-projected into a three-dimensional model. The filaments are displayed not round but oval in the reconstructed tomogram, this is a well-known artifact from tomographic reconstructions with a missing wedge of tilt angles, which also occurs in computed tomography from regular TEM tilt series (Midgley & Dunin-Borkowski, 2009).

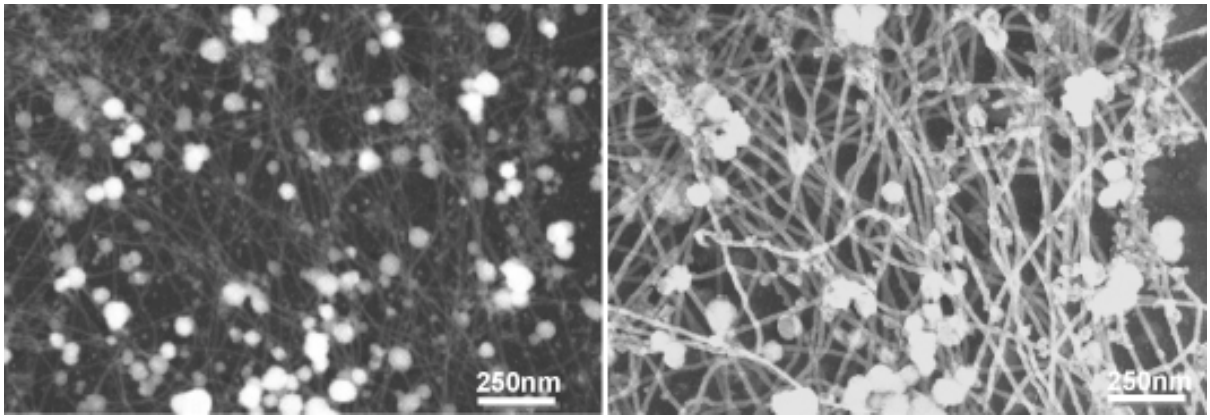

Fig. 2: *Same area of an extracted Panc 1 cell imaged simultaneously in an SEM at 30 kV. The left image was recorded using the transmission dark field signal whereas the right one is the image of the secondary electron signal. The contrast of the filaments is higher in the secondary electron image than in the transmission image.*

Fracturing of actin filaments leading to branch-like structures is described in the literature by e.g. Resch et al. (2002) or by Vignal & Resch (2003). To investigate whether this kind of artifact formation also happens to the keratin filament system, control samples were prepared using a freeze drying protocol. When comparing images of freeze dried keratin filament networks with critical point dried samples, we could not observe morphological differences. In both cases the filaments showed similar branching and directional distribution. We assume, therefore, that the keratin filament network is more robust than the actin network and thus less affected by extraction, fixation, dehydration and drying methods.

3.2 Three-dimensional analysis of intermediate filament networks using SEM-tomography

Authors: S. Lück, **M. Sailer**, V. Schmidt and P. Walther
(The first two authors contributed equally)
Journal of Microscopy (2010), Vol. 239, pp1-16.

In previous studies a correlation between keratin filament network structures and the migration ability of cells (Beil et al., 2003) was detected based on quantitative analyzes of two-dimensional electron microscopical images of the keratin network (Beil et al., 2005). The aim of the current study was to expand these data to three-dimensional tomographic datasets.

For this purpose different methods for imaging and cell preparation were compared. First the samples were analyzed with TEM, 300 kV STEM and 30 kV STEM, but unfortunately the individual filaments surrounded by other cell compounds could not be tracked easily. So the next step was the analyzation of keratin filament networks obtained from detergent-extracted cells. When then imaged using a 300 kV STEM and a 30 kV STEM, the volume-dependent STEM signal did not give enough contrast of the filaments in comparison to the strong signal from unextracted cell compounds, since the thin filaments have only a small volume. The signal was, however, increased when using the secondary electron signal, which is surface-dependent and therefore relatively strong from these filaments. Tomograms were recorded with an Hitachi S-5200 in-lens SEM (Hitachi, Tokyo) at an accelerating voltage of 5 kV by tilting the sample with 2° step size to a maximum tilt of -60° to +60° using a newly developed pre-tilted holder. The resulted image series then could be back projected into a three-dimensional model using the imod software (Kremer et al., 1996; Fig. 3). Although the tilt series does not strictly conform to the projection requirements of tomographic reconstruction, this method was possible due to specific properties of the detergent extracted samples. These data were analyzed with mathematical approaches. After noise reduction the tomograms were binarized by a semi automatical thresholding procedure and skeletonized by using the Avizo software package (Fig. 4). It was taken into account that the missing tilt wedge and shadowing effects lead to oval stretched filament profiles in the binarized tomograms, which was compensated by a special algorithm. To reduce artifacts like loops and dead-ends, several corrections were made. For morphological analysis of the filament network, parameters that can influence the elasticity of the network, namely network density, mean segment length and

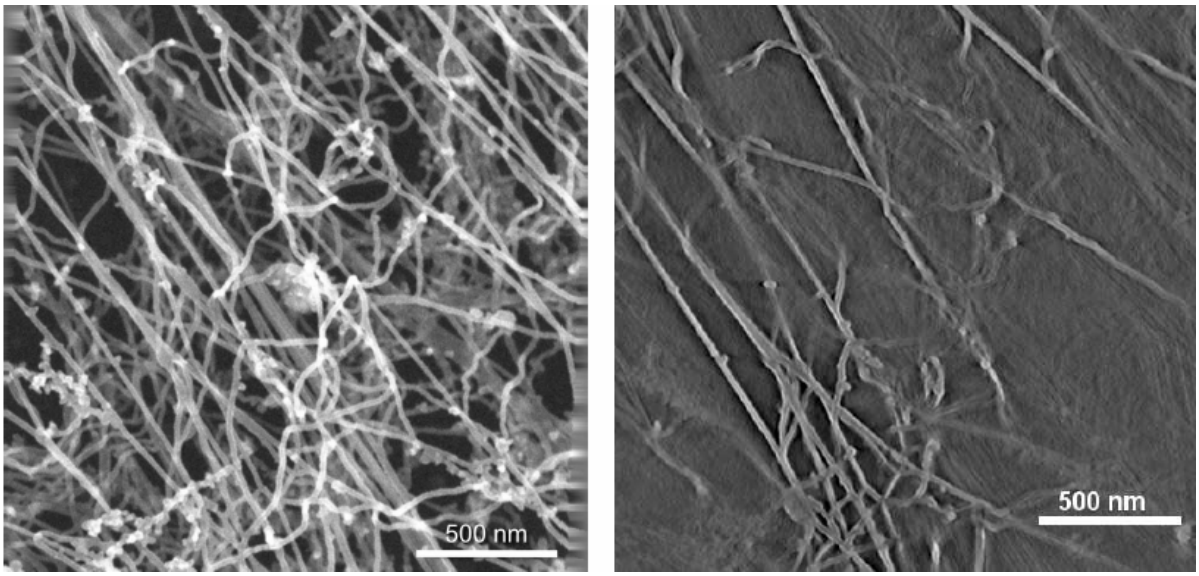

Fig. 3: *0°-image of a tilt series of the keratin filament network of an extracted Panc1 cell (left) and one layer of the reconstructed tomogram (right).*

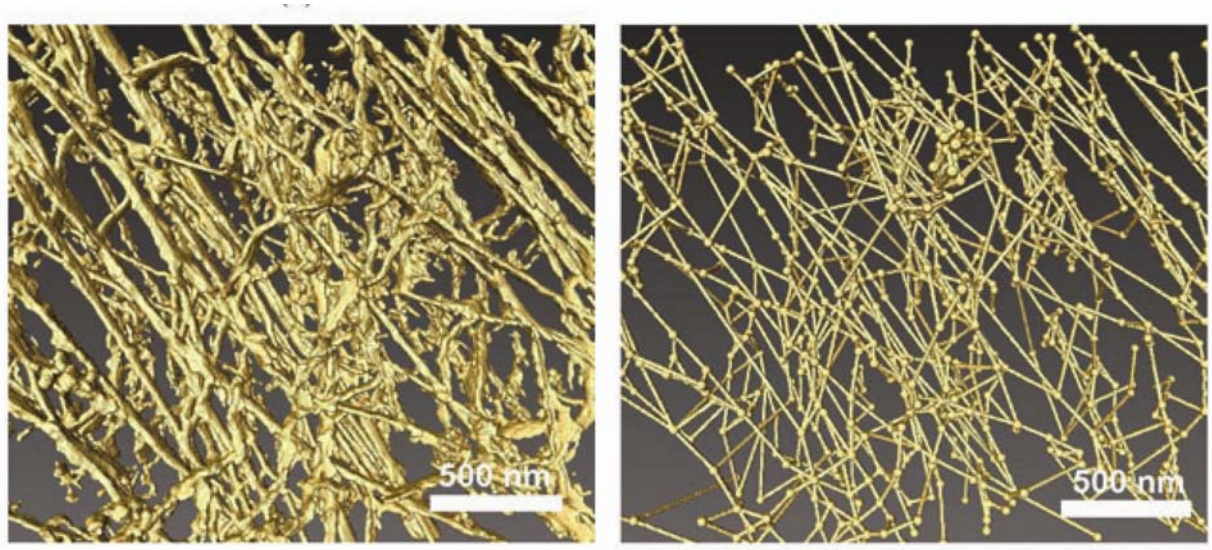

Fig. 4: *Reconstructed tomogram after binarization (left) and network graph extracted from the tomogram (right).*

mean vertex degree were statistically tested. It turned out that there was no significant correlation between network density and mean vertex degree, as well as between network density and mean segment length, but a negative correlation between mean segment length and mean vertex degree. These results may be a hint that the mechanically relevant structural characteristics connectivity and mean segment length do not depend on network density. Panc 1 cells apparently can influence mechanical properties not only by the amount of intermediate filament protein but also by the network architecture.

3.3 Statistical analysis of the intermediate filament network in cells on mesenchymal lineage by greyvalue-oriented image segmentation

Authors: Lück, S., Fichtl, A., **Sailer, M.**, Joos, H., Brenner, R.E., Walther, P., & Schmidt, V. (Submitted to Computational Statistics)

In this study the morphology of the keratin intermediate filament network of different cell types of mesenchymal origin was analyzed. Undifferentiated mesenchymal stem cells, chondrocytes and osteoblasts were used. Mesenchymal stem cells have the potential to differentiate into chondrocytes or osteoblasts. Intermediate filaments, microtubules and the actin filament network form the cytoskeleton, which is involved in signal transduction, thereby influencing cellular differentiation and function, and also in cell migration. Intermediate filaments in cells from mesenchymal lineage consist mainly of the protein vimentin and thus have certain viscoelastic properties, e.g. protecting cellular integrity from mechanical deformations. These viscoelastic properties are regulated by their morphological properties (Heussinger and Frey 2007, Huisman et al. 2007, Lin et al. 2010, MacKintosh et al. 1995) and even small alterations in morphology can have an influence on cell mechanics. Hence, it is very important to study this network architecture at the level of single filaments and their cross-links. For this purpose detergent extracted cells were imaged using a scanning electron microscope (SEM). The varying greyscale of filament pixels which were bright in the top filament layer and rather dark in the bottom layer, made it necessary to use greyscale-oriented methods for image binarization. In this situation simple binarization by thresholding would have either resulted in a loss of filaments in lower network layers or background noise would have been classified as foreground. As a remedy, an algorithm was applied to compute a lower λ-leveling kernel (Couprie et al., 2001), which extracts the crest-lines of the grey-value topology in the image. The resulting image of crest lines accounts for lower-level filaments but is distorted not by image noise. An artefact occurring in the crest line images was a certain oversegmentation in the upper filament layer, which was due to local greyscale minima within thicker filaments. To reduce the oversegmentation the binarized crest lines (Fig. 3 c) were in a first step dilated by 2 pixels, which means that all pixels whose distance to a crest line did not exceed two pixels were classified as foreground and colored white. The dilation closed small network meshes resulting from oversegmentation but still contained the lower level information of the crest line extraction. The dilated image was added to a binarized version of the original SEM image, which had been computed by simple

thresholding with a high threshold parameter. The latter reliably detected the bright upper-layer filaments without the oversegmentation in the crest-line images caused by local minima. This way a binarization containing lower-level information without substantial contributions of noise and hardly oversegmentation in upper network layers was achieved. This binarization was finally thinned to pixel trajectories of width 1 by the standard skeletonization algorithm in ImageJ (Rasband, 1997-2010). A network graph was constructed establishing linear connections between junctions of pixel trajectories in the skeletonized images. Based on the network graphs extracted from the SEM image data the network morphology was statistically analyzed and compared between different cell types. Samples were analyzed separately for the cell periphery and the perinuclear cellular compartment. A total of 138 images was statis-

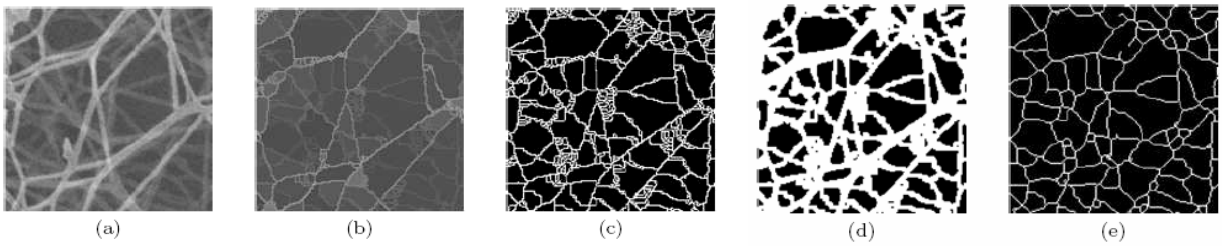

Fig. 5: *a, Original image; b, Lower λ-leveling kernel; c, Extracted crest lines; d, Superposition of dilated crest lines and intermode threshold of a,; e, Skeleton of d,.*

tically analyzed, where sample sizes varied between 15 and 20 images per cell type and cellular compartment. For each image the total network length per unit area and the mean edgelength was computed. It turned out that in chondrogenic direction there is a substantial decrease in network density and a corresponding increase of the mean edge length in the cell periphery, whereas osteoblasts exhibit an intermediate filament network which is not very different from mesenchymal stem cells. Some of the stem cells, however, showed a high network density in their periphery, which could not be found in the other cell types. This indicates that the intermediate filament network is a dynamical system showing substantial local variations of its morphology even within single cells. By modifications of the network structure cells are able to adapt their mechanical properties to their needs during migration and mitosis.

3.4 Morphological analysis of CK20 transfected Panc1 cells

Cytokeratin 20 (CK20) belongs to the intermediate filament protein family and there to the type I keratins and it is expressed in epithelia of the stomach, the intestine, the uterus, the bladder and in Merkel cells (Zhou et al., 2006). It can be used as a biomarker for the detection of metastatic origin in patients with colonic, gastric, and pancreatic carcinomas.

The aim of this experiment was to elucidate possible morphological differences in the keratin filament network of CK20 transfected Panc 1 cells in comparison with normal Panc 1 cells.

CK20-DNA was amplified in *E. coli*, extracted and purified. Panc1 cells were transfected with CK20 using $CaPO_4$ with Geneticin resistance as selection marker. The clones were cultivated in an incubator at 310 K and 5% CO_2. For electron microscopical analyzes the cells were extracted using Triton X-100, chemically fixed with glutar aldehyde, critical point dried and coated with a thin layer of carbon (about 5nm). When comparing these cells with normal Panc1 cells, in fact, there seemed to be differences concerning cell shape and size. The keratin network of the transfected cells, however, seemed to be similar to the network of untransfected cells, it showed similar branching and directional distribution of the filaments. Though, for an exact conclusion mathematical analysis would be needed.

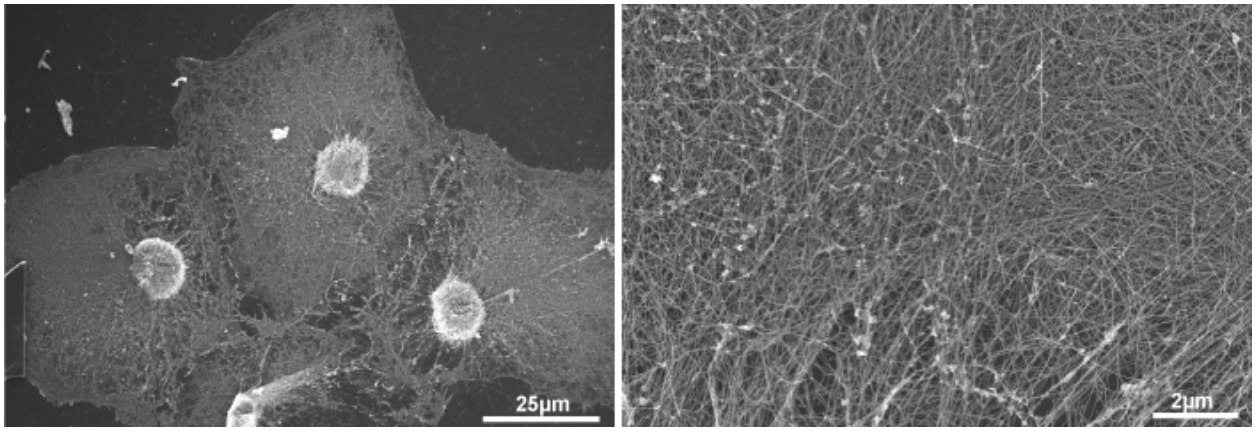

Fig. 6: *Starved transfected Panc1 cells. Keratin network of starved transfected Panc1 cell at magnification.*

3.5 Analysis of the keratin filament network with helium ion microscopy

A new only recently developed kind of microscope exists for examining surfaces, the scanning helium ion microscope (HIM). In contrast to a SEM, which uses electrons, a HIM possesses a stable helium ion beam with extremely high intensity for scanning the surface of a sample (Scipioni et al., 2008). With this kind of microscope it is theoretically possible to reach a better resolution due to the very short De Broglie wavelength of the helium ions. Furthermore, with this kind of microscope it is possible to analyze uncoated samples.

The motivation for this experiment was the ability of the HIM to examine uncoated filaments. By comparing these data with our SEM data, we wanted to check if the unnatural thickness of coated filaments of about 20 nm actually was caused by the coating. Panc1 cells were extracted using 1% Triton X-100, chemically fixed with glutar aldehyde and critical point dried. Half of the samples were coated with a thin layer of carbon, the other half were left uncoated. Images of these cells were taken using an Orion microscope, (Zeiss, Oberkochen) with a stable helium ion beam with extremely high brightness.

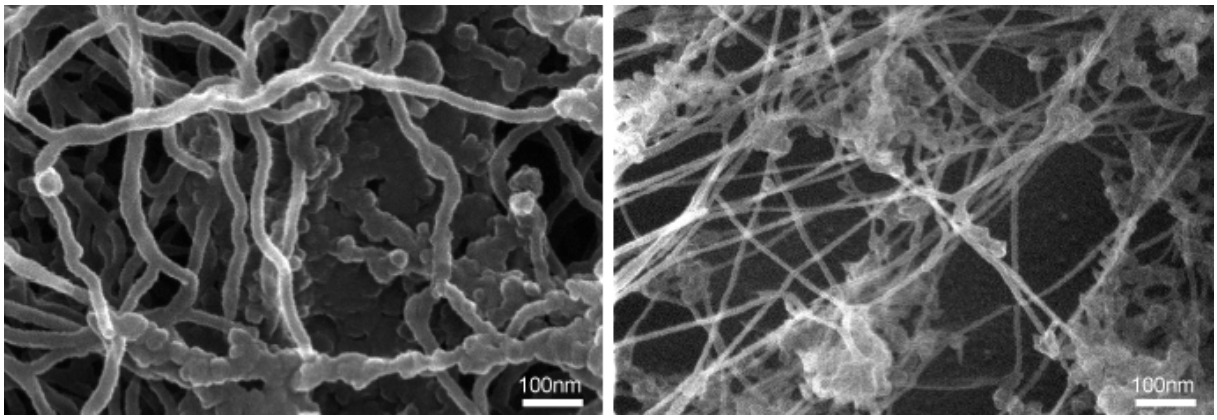

Fig. 7: *Carbon coated (left) and uncoated (right) samples from extracted Panc1 cells.*

Fig. 7 shows carbon coated keratin filaments (left) and uncoated ones (right). Both images were recorded using the same magnification and the same accelerating voltage of 32 kV. The filaments from the coated sample possessed a diameter of about 20 nm, which was in agreement with our SEM data. The diameter of the uncoated filaments, however, was about the expected value of 10-12 nm known from the literature (Alberts et al., 2008). Observation of uncoated filament networks in an SEM would be difficult to impossible due to electrical charge-up of the sample.

3.5 Preparation of cryofixed cells for improved 3D ultrastructure with scanning transmission electron tomography

Höhn, K., **Sailer, M.**, Wang, L., Lorenz, M., Schneider, M. & Walther, P.

Histochemistry and Cell Biology, 2010 (E-Pub ahead of print)

Scanning transmission electron microscopical (STEM) tomography is based on transmission microscopical (TEM) tomography, where the sample is scanned by a fine focused electron beam providing enhanced contrast and where depth of focus and inelastic scattering is not a limitation. Samples up to 1µm thickness can be analyzed by tilting the sample gradually. For this work high pressure freezing, freeze substitution, plastic embedding and thin sectioning were used as an established preparation protocol that can be easily applied to many different biological systems (reviewed by McDonald, 2007). STEM tomograms of mitochondria, hemophagocytes, microvilli of Panc 1 cells and intermediate filaments also of Panc 1 cells were recorded. Intermediate filaments were also recorded using SEM tomography. The inner and outer mitochondrial membranes as well as the membranes in the cristae appeared in very close apposition with a minimal intermembrane space. In 880 nm thick sections of hemophagocytes, the three dimensional structure of membrane sheets could be observed in the virtual sections of the tomogram. A fundamental problem of analyzing intermediate filaments with STEM tomography is that contrast of the thin filaments is not high enough to clearly decide whether the filaments are connected with each other, or whether they just cross each other in a short distance.

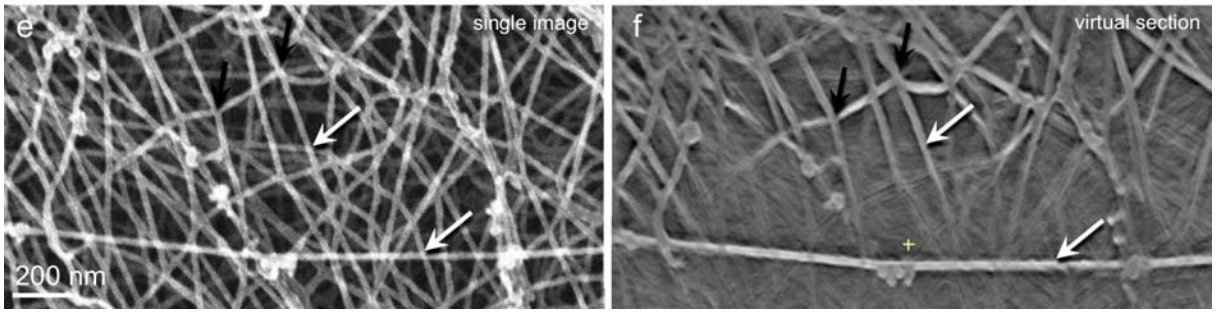

Fig. 8: *Intermediate filament network of Panc 1 cells. Left: one single image of a tilt series; right: reconstructed tomogram of the tilt series. Arrows mark the same filament crossing.*

When using SEM tomography (Figure 8), however, filaments are imaged with much higher contrast and in a virtual section it can be clearly decided, whether the filaments cross in different planes (white arrows) or touch each other (black arrows).

4. General Conclusions

The main aim of this work was to expand already existing data of the keratin intermediate filament system of Panc 1 cells to three-dimensional datasets. This was achieved by applying a new technique, SEM tomography, a certain kind of electron tomography. For this purpose a new sample holder was created, which allows tilting the sample to ± 60°. In combination with the extraction protocol, it was possible to record tomograms where the filaments could be tracked even in deeper layers. With these tomograms it was possible to analyze the keratin filament network mathematically regarding to parameters like network density and filament length. These results can offer valuable clues about the migration ability of pancreatic caneroid cells and furthermore also for other cell types.

5. References

Alberts, B., Johnson, A., Lewis, L., Raff, M., Roberts, K. & Walter, P. *Molecular Biology of the Cell,* fifth edition. Garland Publishing, New York, NY (2008).

Abbe, E. (1873). Beiträge zur Theorie des Mikroskops und der mikroskopischen Wahrnehmung. *Archiv für mikroskopische Anatomie* **9**, 418-440.

Aoyama, K., Takagi, T., Hirase, A, Miyazawa, A. (2008). STEM tomography for thick biological specimens. *Ultramicroscopy* **109**, 70–80.

Beil, M., Micoulet, A., von Wichert, G., Paschke, S., Walther, P., Omary, M.B., Van Veldhoven, P.P., Gern, U., Wolff-Hieber, E., Eggermann, J., Waltenberger, J., Adler, G., Spatz, J. & Seufferlein, T. (2003). Sphingosylphosphorycholine regulates keratin network architecture and viscoelastic properties of human cancer cells. *Nat Cell Biol* **5**, 803-811.

Beil, M., Braxmeier, H., Fleischer, F., Schmidt, V. & Walther, P. (2005). Quantitative analysis of keratin filament networks in scanning electron microsopy images of cancer cells. *J Microsc* **220**, 84-95.

Beil, M., Eckel, S., Fleischer, F., Schmidt, H., Schmidt, V. & Walther, P. (2006). Fitting of random tessellation models to keratin filament networks. *J Theor Biol* **241**, 62-72.

Couprie, M., Bezerra, F.N. & Bertrand, G. (2001). Topological operators for grayscale processing. *J Electron Imaging* **10**, 1003–1015

Fuchs, E. & Weber, K. (1994). Keratin (intermediate) filaments: structure, dynamics, function and disease. *Annu Rev Biochem* **63**, 345-82.

Ellenrieder, V. Adler, G. & Gress, T.M. (1999). Invasion and metastasis in pancreatic cancer. *Ann Oncol* **10**, 46-50.

Hatzfeld, M. & Franke, W.W. (1985). Pair formation and promiscuity of cytokeratins: formation in vitro of heterotypic complexes and keratin (intermediate)-sized filaments by homologous and heterologous recombinations of purified polypeptides. *J Cell Biol* **101**, 1826-1841.

Herrmann, H. & Aebi, U. (2004). Intermediate filaments: molecular structure, assembly mechanism, and integration into functionally distinct intracellular Scaffolds. *Annu Rev Biochem* **73**, 749-89.

Herrmann, H., Hesse, M., Reichenzeller, M., Aebi, U. & Magin, T.M. (2003). Functional complexity of keratin (intermediate) filament cytoskeletons: from structure to assembly to gene ablation. *Int Rev Cytol* **223**, 83-175.

Heussinger, C. & Frey, E. (2007). Role of architecture in the elastic response of semiflexible polymer and fiber networks. *Phys Rev E* **75**, 011917

Hohmann-Marriott, M.F., Sousa, A.A., Azari, A.A., Glushakova, S., Zhang, G., Zimmerberg, J. & Leapman, R.D. (2009). Nanoscale 3D cellular imaging by axial scanning transmission electron tomography. *Nat Methods* **6**, 729-731.

Hoppe, W., Gassmann, J., Hunsmann, N., Schramm, H.J. & Sturm, M. (1974). Three-dimensional reconstruction of individual negatively stained yeast fatty-acid synthetase molecules from tilt series in the electron microscope. *Z Physiol Chem* **355**, 1483-1487.

Huisman, E.M., van Dillen, T.M., Onck, P.R. & Van der Giessen, E. (2007). Three-dimensional cross-linked F-actin networks: Relation between network architecture and mechanical behavior. *Phys Rev Lett* **99**, 208103

Janmey, P.A., Euteneuer, U., Traub, P., Schliwa, M. (1991). Viscoelastic properties of vimentin compared with other filamentous biopolymer networks. *J Cell Biol*. **113**, 155-60.

Kremer, J.R., Mastronarde, D.N. & McIntosh, J.R. (1996). Computer visualization of three-dimensional image data using IMOD. *J Struct Biol* **116**, 71–76.

Ladinsky, M.S., Mastronarde, D.N., McIntosh, J.R., Howell K.E. & Staehelin, L.A. (*1999*) Golgi structure in three dimensions: functional insights from the normal rat kidney cell. *J Cell Biol* **144***,* 1135–1149.

Lin, Y., Broedersz, C.P., Rowat, A.C., Wedig, T., Herrmann, H., MacKintosh, F.C. & Weitz, D.A. (2010). Divalent cations crosslink vimentin intermediate filament tail domains to regulate network mechanics. *J Mol Biol* **399**, 637–644

McDonald, K. (2007). Cryopreparation Methods for Electron Microscopy of Selected Model Systems. In: J. R. McIntosh (Ed) Cellular Electron Microscopy. (Methods in Cell Biology) Elsevier **79**, 23-56.

MacKintosh, F., Käs, J. & Janmey, P.A. (1995). Elasticity of semiflexible biopolymer networks. *Phys Rev Lett* **75**, 4425-4428

Midgley, P.A., Weyland, M., Thomas, J. M., Johnson, B.F.G. (2001). Z-contrast tomography: A technique in 3-dimensional nanostructural analysis based on Rutherford scattering. *Chem Comm* **18,** 907-908.

Midgley, P.A. & Dunin-Borkowski, R.E. (2009). Electron tomography and holography in materials science. *Nat Mater* **8**, 271-280.

Moor, H. & Riehle, U. (1968) Snap-freezing under high pressure: a new fixation technique for freeze-etching. Proc. 4th European Reg. Conf. Electron Microscopy. **2**, 33-34.

Rasband, W.S. (1997-2010). ImageJ. U.S. National Institutes of Health, Bethesda, Maryland, USA. http://rsb.info.nih.gov/ij/

Resch, G.P., Goldie, K.N., Krebs, A., Hoenger, A. & Small, J.V. (2002) Visualisation of the actin cytoskeleton by cryo-electron microscopy. *J. Cell Sci.* **115**, 1877-1882.

Ris, H. (1985) The cytoplasmic filament system in critical point dried whole mounts and plastic embedded sections. *J Cell Biol* **100**, 1474-1487.

Scipioni, L., Sanford, C.A., Notte, J., Thompson, B. & McVey, S. (2008). Understanding imaing modes in the helium ion microscope. *J Vac Sci Technol* **27**, 3250-3255

Seiler, H. (1967). Einige aktuelle Probleme der Sekundärelektronenemission. *Z angew Phy* **22,** 249-263.

Svitkina, T.M. & Borisy, G.G. (1998). Correlative light and electron microscopy of the cytoskeleton of cultured cells. *Method Enzymol* **298**, 570-592.

Szczesny, P.J., Walther, P. & Müller, M. (1996). Light damage in rod outer segments: The effects of fixation on ultrastructural alterations. *Current Eye Res* **15,** 807-814.

Urban., E., Jacob, S., Nemethova, M., Resch, G.P & Small, J.V. (2010). Electron tomography reveals unbranched networks of actin filaments in lamellipodia. *Nat Cell Biol* **12**, 429-35.

Vignal, E. & Resch, G. (2003). Shedding light and electrons on the lamellipodium: imaging the motor of crawling cells. *Biotechniques* **34**, 780-4, 786, 788-9.

Walther, P. (2003). Recent progress in freeze fracturing of high-pressure frozen samples. *J Microsc* **212**, 34-43.

Walther, P. (2008). High Resolution Cryoscanning Electron Microscopy of Biological Samples. Book article in: Schatten H, Pawley J. B. (eds) Biological Low-Voltage Scanning Electron Microscopy. Springer New York. ISBN 978-0-387-72970-1 (Print) 978-0-387.72972-5 (Online). pp 245-261.

Yakushevska, A.E., Lebbink, M.N., Geerts, W.J., Spek, L., van Donselaar, E.G., Jansen, K.A., Humbel, B.M., Post, J.A., Verkleij, A.J. & Koster, A.J. (2007). STEM tomography in cell biology. *J Struct Biol* **159**, 381-391.

Zhou, Q., Cadrin, M., Herrmann, H., Chen, C-H., Chalkley, R.J., Burlingame, A.L. & Omary, M.B. (2006). Keratin 20 serine 13 phosphorylation is a stress and intestinal goblet cell marker. *J Biol Chem* **281**, 16453-16461.

6. List of own publications

6.1 Full size articles in peer reviewed journals

Sailer, M., Höhn, K., Lück, S., Schmidt, V., Beil, M. & Walther, P. (2010). Novel electron tomographic methods for three-dimensional analysis of keratin filament networks. *Microsc Microanal* **16**, 462-471.

Lück, S., **Sailer, M.**, Schmidt, V. & Walther, P. (2010). Three-dimensional analysis of intermediate filament networks using SEM-tomography. *J Microsc* **239**, 1-16.

Höhn, K., **Sailer, M.**, Wang, L., Lorenz, M., Schneider, M.E. & Walther, P. (2010). Scanning transmission electron tomography for improved 3D ultrastructure of cryofixed cells. *Histochem Cell Biol* (E-Pub ahead of publication)

Lück, S., Fichtl, A., **Sailer, M.**, Joos, H., Brenner, R.E., Walther, Paul, & Schmidt, V. (20XX). Statistical analysis of the intermediate filament network in cells on mesenchymal lineage by grayvalue-oriented image segmentation. (Submitted to Computational Statistics)

6.2 Abstracts

Sailer, M., Lück, S., Schmidt, V., Beil, M., Adler, G. & Walther, P. (2008). Three-dimensional analysis of the keratin (intermediate) filament network using SEM-tomography. In: A. Aretz, B. Hermanns-Sachweh, J. Mayer (Eds.), *Proceedings of EMC 2008*, pp. 91-92. Springer-Verlag Berlin Heidelberg.

Sailer, M., Lück, S., Schmidt, V., Beil, M., Adler, G. & Walther, P. (2009). Three-dimensional analysis of the intermediate filament network using SEM-tomography. In: M.A. Pabst and G. Zellnig (Eds), *Proceedings of MC 2009*, pp. LI.P603-604. Verlag der TU Graz.

Lück, S., Fichtl, A., **Sailer, M.**, Joos, H., Brenner, R.E., Walther, P. and Schmidt, V. (2010) Quantitative analysis of the intermediate filament network in scanning electron microscopy images by grayvalue-oriented segmentation methods. Statistical Computing 2010, Schloss Reisensburg, Günzburg.

7. Acknowledgement

First of all I want to express my gratitude to my supervisor Paul Walther for accepting me as PhD student and for his continuous help and encouragement throughout this work. He was always there to meet and talk about my work and solve any problems. I've learned a lot from him and without his support I could not have finished my dissertation successfully.

Furthermore, I also want to thank Michael Beil, Volker Schmidt and Sebastian Lück for scientific input and constructive teamwork.

Many thanks to Elke Wolff-Hieber, Iris Repple, Renate Kunz, Chris Hormann, Eberhard Schmid and Reinhard Weih for that I always could count on them and their technical support. Also thanks to all the other members of the lab and their friendly help.

Special thanks go to all the „Jufos"of the lab: Holger Krisp, Katharina Höhn, Li Wang, Christian Soor, Bastian Seidl, Martin Dass, Julia Huber, Christopher Schmid, Martin Schauflinger, Sukhum Ruangchai, Jacinthe Gagnon, Helena Ederle and Heiko Gregorius. With their know-how and ideas they always gave me the necessary push during difficult moments and they were always up for a little fun!

Last but not least, I want to thank Kay Averhoff and my family, who always stood behind me. Without their encouragement and understanding it would have been impossible for me to finish this work.

8. Appendix

Microsc. Microanal. 16, 462–471, 2010
doi:10.1017/S1431927610093657

Microscopy AND Microanalysis

Novel Electron Tomographic Methods to Study the Morphology of Keratin Filament Networks

Michaela Sailer,[1] Katharina Höhn,[1] Sebastian Lück,[2] Volker Schmidt,[2] Michael Beil,[3] and Paul Walther[1,*]

[1]*Electron Microscopy Facility, Ulm University, D-89069 Ulm, Germany*
[2]*Institute of Stochastics, Ulm University, D-89069 Ulm, Germany*
[3]*Department of Internal Medicine I, University Hospital Ulm, D-89070 Ulm, Germany*

Abstract: The three-dimensional (3D) keratin filament network of pancreatic carcinoma cells was investigated with different electron microscopical approaches. Semithin sections of high-pressure frozen and freeze substituted cells were analyzed with scanning transmission electron microscope (STEM) tomography. Preservation of subcellular structures was excellent, and keratin filaments could be observed; however, it was impossible to three-dimensionally track the individual filaments. To obtain a better signal-to-noise ratio in transmission mode, we observed ultrathin sections of high-pressure frozen and freeze substituted samples with low-voltage (30 kV) STEM. Contrast was improved compared to 300 kV, and individual filaments could be observed. The filament network of samples prepared by detergent extraction was imaged by high-resolution scanning electron microscopy (SEM) with very good signal-to-noise ratio using the secondary electron signal and the 3D structure could be elucidated by SEM tomography. In freeze-dried samples it was possible to discern between keratin filaments and actin filaments because the helical arrangement of actin subunits in the F-actin could be resolved. When comparing the network structures of the differently prepared samples, we found no obvious differences in filament length and branching, indicating that the intermediate filament network is less susceptible to preparation artifacts than the actin network.

Key words: keratin (intermediate) filaments, SEM tomography, STEM tomography, pancreas, keratin, actin, electron microscopy

Introduction

Biological structures such as cytoskeletal networks are three-dimensional (3D); classical electron microscopy, however, provides only two-dimensional (2D) images. To fill this gap, a number of techniques have been developed to record 3D datasets. Although the origins of these methods lay several decades in the past, these methods became more widely used only recently because more efficient computer and storage devices greatly facilitate the handling of large datasets.

Three-Dimensional Imaging by Electron Microscopy

The most widely used approach to record electron tomographical datasets in a transmission-type electron microscope (TEM) is tilting the sample over a large angular range of about ±70° with small increments (about 2°) and thereby acquiring a series of 2D projection images. This tilt series is then back-projected into a 3D model (Hoppe et al., 1974 and others; recently reviewed by Baumeister, 2004). A further development of TEM tomography is scanning transmission electron microscopical (STEM) tomography (Midgley et al., 2001; Midgley & Dunin-Borkowski, 2009). Yakushevska et al. (2007) introduced this new technique to life science, highlighting that high-angle annular dark-field (HAADF)–STEM tomography gives a five times better contrast and signal-to-noise ratio than bright-field–TEM tomography. In TEM tomography the imaging of relatively thick sections (e.g., 600 nm) suffers from inelastic scattering that blurs the image due to chromatical aberration in the projective lenses. This effect is especially pronounced at high tilt, where the path length of the electron beam in the sample increases (by about a factor of 3 at 70°). When a scanning beam and a STEM detector are used, however, inelastic scattering does not reduce resolution. The resolution is now mainly limited by widening of the primary beam due to scattering in the sample. Using this method with a 300 kV field emission microscope, we have been able to make tomographic reconstructions of 600 nm thick sections, in which the two leaflets of membrane lipid bilayers are still clearly resolved (Höhn et al., 2009). Thus, we considered STEM tomography a consequential method for the 3D analysis of keratin filament networks. The disadvantage of using 300 kV

Received December 10, 2009; accepted April 24, 2010
*Corresponding author. E-mail: paul.walther@uni-ulm.de

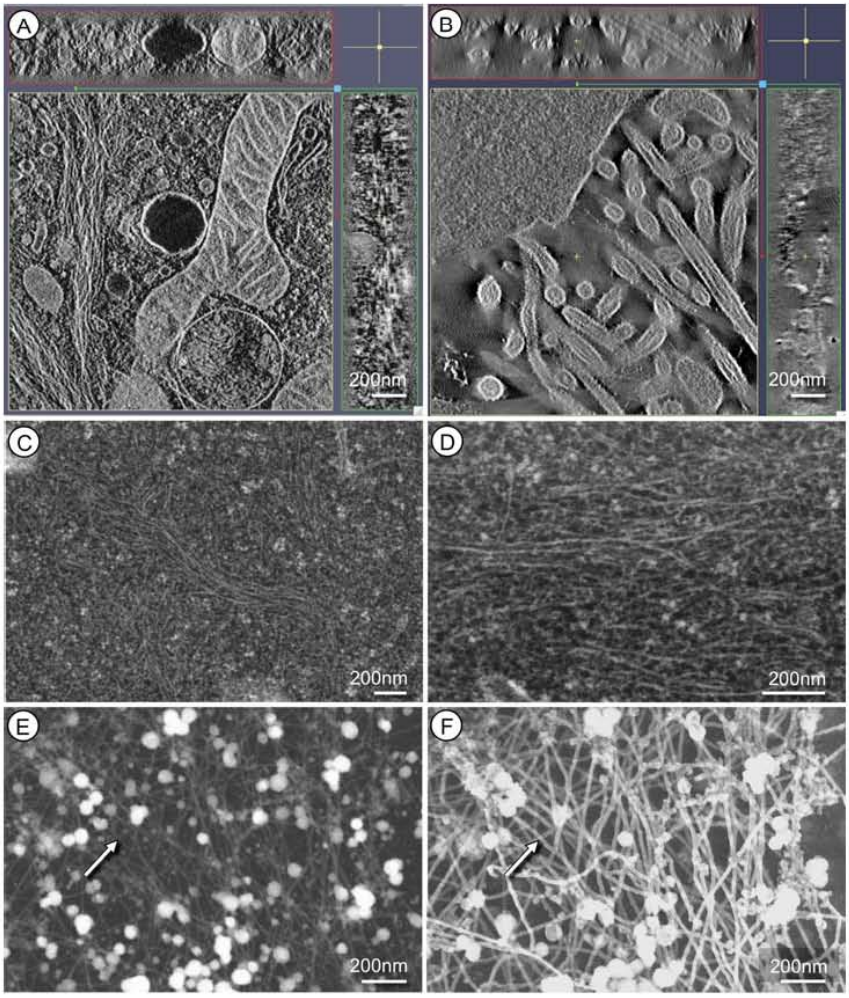

Figure 1. A,B: Computed sections of 300 kV STEM tomograms of high-pressure frozen and freeze substituted Panc 1 cells. Panel **A** was recorded in the perinuclear area whereas panel **B** represents a peripheral area of a cell. **C,D:** Thin sections (80 nm) recorded with an SEM at 30 kV with a dark-field STEM detector. The contrast of the filaments is reasonably good, but obviously 3D information is missing. **E,F:** The same area of an extracted Panc 1 cell imaged simultaneously in an SEM at 30 kV. Panel **E** was recorded using the transmission dark-field signal, whereas panel **F** is the image of the secondary electron signal. The contrast of the thin filaments is considerably higher in the secondary electron image **(F)** than in the transmission image **(E)**. Arrows depict the same filament.

accelerating voltage is the low contrast. We, therefore, also investigated the potential of using low voltage (30 kV) for STEM imaging (Sailer et al., 2009). Another approach with great potential for special samples is scanning electron microscopical (SEM) tomography using the secondary electron signal (Sailer et al., 2008; Lück et al., 2010).

Keratin Filament Networks

Keratin filaments belong to the intermediate filaments, a part of the cytoskeleton, which forms a network of protein fibers in the cytoplasm of eukaryotic cells. The scaffold of the intermediate filaments defines the shape and mechanical properties of a cell (Herrmann et al., 2003), such as elasticity (Beil et al., 2003). Keratins are specifically expressed in epithelial cells and form heteropolymers of type I (K9-20) and type II (K1-8) keratin (Hatzfeld & Franke, 1985). Posttranslational modifications of keratin monomers, i.e., phosphorylation and glycosylation, regulate the solubility of keratins and thus network architecture (Coulombe & Omary, 2002; Beil et al., 2005). K8 and K18 are the basic keratins expressed in simple epithelia (Fuchs & Weber, 1994) and their tumors, such as pancreatic carcinoma, which are the subject of this study.

Microscopy of Keratin Filament Networks

Keratin filament networks have been extensively studied with light microscopical methods, with special emphasis on fluorescent microscopy. Windoffer et al. (2004) demonstrated that the keratin filament system is not homogenous but is organized into temporally and spatially distinct subdomains. They provide further evidence that continuous *de novo* formation of keratin fibers in the cell periphery is a general principle in epithelial cells. When comparing fluorescence microscopy data with electron microscopical data of the keratin filament network, it is striking that the electron microscopical images contain much more structural details due to the improved resolution of the electron microscope (Figs. 1, 2). We believe that these images reflect

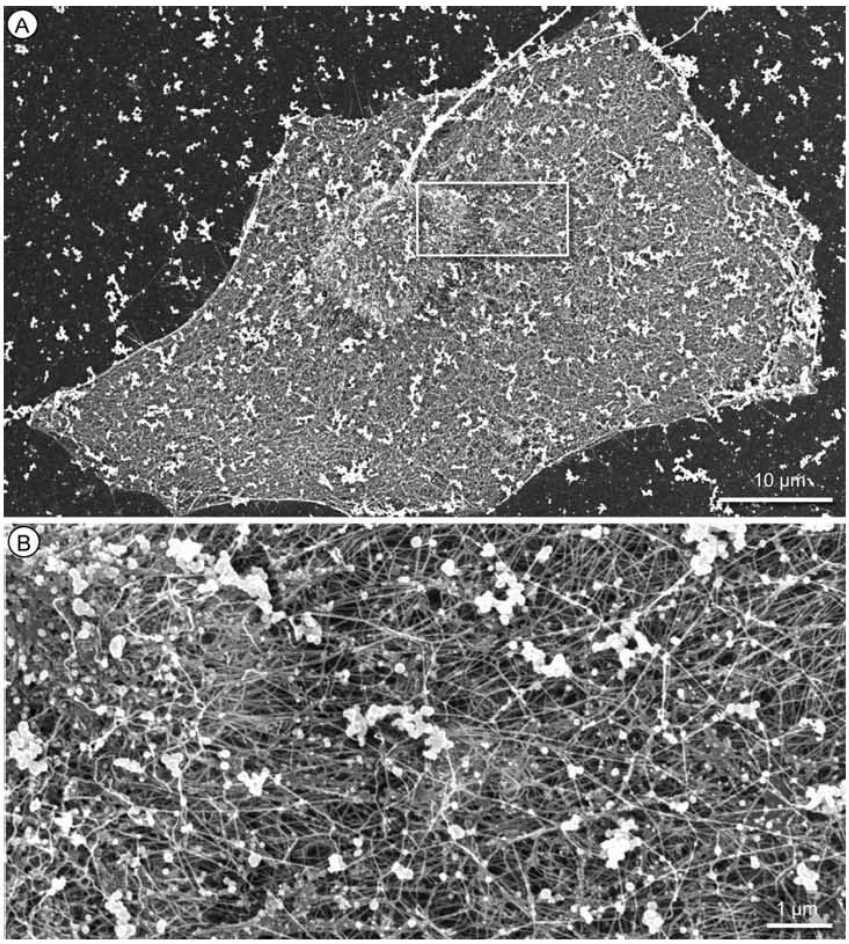

Figure 2. A: An overview of an extracted Panc 1 cell. The rectangular marked area is displayed at higher magnification in panel **B**. These cells exhibit an extremely complex and dense filament network. Some agglomerated cell components are still left because they were not completely removed during extraction. Both images were recorded with an SEM at 5 kV using the secondary electron signal.

the complexity of eukaryotic cells that consist of about 10^{10} protein molecules of about 10^4 different kinds (Alberts et al., 2008). Unfortunately, this complexity makes the life of an electron microscopist difficult because simple and clear interpretation of the information overflow is often not possible. Electron microscopists, therefore, are seeking strategies to make the complex relations of biological ultrastructure understandable. One of these strategies is the use of extraction protocols (Svitkina, 2007). Most of the cell compounds are, thereby, removed, and only the finely structured cytoskeleton remains. In previous studies we have analyzed the keratin network of pancreatic cancer cells using these extraction protocols. The samples have been two-dimensionally imaged in the SEM using the secondary electron signal and quantitatively analyzed by methods from spatial statistics (Beil et al., 2003, 2005, 2006). In our recent work we have expanded these studies to visualize the 3D structure of the network by SEM tomography (Sailer et al., 2008, 2009; Lück et al., 2010).

In this study we investigate and compare different preparation and imaging protocols for preservation and recording of 3D keratin filament networks in pancreatic canceroid cells, including high-pressure freezing, freeze substitution, embedding, and thin sectioning as well as extraction protocols. We analyzed these samples with 300 kV STEM-tomography, with (30 kV) low-voltage STEM and, finally, with secondary electron SEM tomography.

Material and Methods

Sample Preparation

Cell Culture

Panc 1 human pancreatic cancer cells (American Type Culture Collection, Manassas, VA, USA) were seeded (5×10^4 cells/mL) and cultivated in an incubator at 310 K and 5% CO_2. For the experiments, cells were grown as a monolayer on glow discharged sapphire discs coated with carbon. For the low-voltage STEM experiments of Fig. 1E,F, cells were grown on electron transparent carbon coated and glow discharged 200 mesh gold grids.

Preparation of High-Pressure Frozen and Freeze Substituted Cells

The cells on sapphire discs were frozen using a Wohlwend HPF Compact 01 high-pressure freezer (Engineering Office M. Wohlwend GmbH, Sennwald, Switzerland) as described by Buser and Walther (2008). During the following freeze substitution, water was replaced by the freeze substitution medium consisting of acetone, osmium tetroxide, uranyl acetate, and 5% of water (Walther & Ziegler, 2002). This procedure lasted about 16–18 h during which the temperature was slowly increased from 183 to 273 K. After substitution the samples were kept at room temperature for 30 min and then washed twice with acetone. After embedding of the samples in epon (polymerization at 333 K within 72 h), they were cut with a microtome (Leica Ultracut UCT ultramicrotome) using a diamond knife (Diatome, Biel, Switzerland) in ultrathin sections of a thickness of 80 nm for low-voltage SEM and about 500 nm for STEM tomography and mounted on copper grids. For low-voltage STEM the sections were post-stained with lead citrate and uranyl acetate. Finally the samples were coated with a thin layer of carbon (5 nm) on both sides.

Preparation of Extracted Cells by Critical Point Drying

To visualize the intermediate filament network by high-resolution SEM, a prefixation extraction method was applied, based on the protocols of Svitkina and Borisy (1998) and Svitkina (2007). After washing with phosphate-buffered saline (PBS; pH 7.3), the cells were extracted for 25 min at around 281 K with 1% Triton X-100 (in PBS). Afterward, cells were washed again with PBS and chemically fixed with 2.5% glutaraldehyde (in PBS and 1% saccharose) for 1 h at room temperature. After washing with PBS, the cells were contrasted with OsO_4 (2% in PBS) for 1 h at room temperature. After repeated washing with PBS, the samples were gradually dehydrated in 30%, 50%, 70%, 90%, and 100% Propanol for 5 min. Then the cells were critical-point dried using carbon dioxide as translation medium (Critical Point Dryer CPD 030, BalTec, Principality of Liechtenstein). Finally, the samples were coated with a 5 nm layer of carbon in a freeze etching device (Baf 300, BalTec, Principality of Liechtenstein). The thickness was controlled with a quartz crystal monitor.

Preparation of Extracted Cells by Freeze Drying

Cells grown on sapphire discs were extracted with 1% Triton as described above with 10 μM phalloidin added (to stabilize the actin network during preparation), and chemically fixed with 2.5% glutaraldehyde in PBS and 1% saccharose. Then they were washed with distilled water, and 10% of ethanol was added to prevent ice crystal formation during freezing. The samples were frozen by immersion in liquid propane, supercooled by liquid nitrogen. The frozen samples were mounted on a holder that fits into the Gatan cryo stage and cryo-transferred to a Baf 300 freeze-etching device (Bal-Tec, Principality of Liechtenstein). The samples were partially freeze dried for 30 min at 180 K and then for 10 min at 185 K. Finally, the samples were coated with 2 nm of tungsten by electron beam evaporation at the same temperature (Walther, 2008). The samples were never warmed up but kept cold during liquid-nitrogen transfer to the cryo-stage of the SEM.

Electron Microscopy

STEM Tomography

STEM tomography of semithin sections (500 nm) of high-pressure frozen and freeze substituted Panc 1 cells was done with a Titan 80-300 field emission STEM (FEI, Eindhoven, Netherlands) at an accelerating voltage of 300 kV and a convergence angle of 10 mrad. Tilt series ($-72°$ to $+72°$) were recorded in scanning mode (1024×1024 pixels) with a HAADF detector (Fischione, Export, PA, USA). The camera length was 301 mm. Tomograms were reconstructed with the IMOD software (Kremer et al., 1996) by weighted back projection (Fig. 1A,B).

Low-Voltage STEM

Low-voltage STEM of 80 nm ultrathin sections of high-pressure frozen and freeze substituted Panc 1 cells was performed with a cold-field emission SEM (Hitachi S-5200 in-lens SEM, Tokyo, Japan) equipped with a transmission detector that was used in dark-field mode for best contrast. Images (1280×800 pixels) were recorded in STEM mode at an accelerating voltage of 30 kV (Figs. 1C–E, 5B).

SEM Tomography

SEM tomography of extracted cells was also performed with a Hitachi S-5200 in-lens SEM (Tokyo, Japan). For this purpose a holder pretilted by 30° was constructed that allows tilting over a range from $-60°$ to $+60°$, though the holder has to be turned by 180° and the sample needs to be remounted after recording half of the tilt series. Tomographical datasets were obtained at tilt angles from $-60°$ to $+60°$ at an increment of 2° with a magnification of 50,000 and an accelerating voltage of 5 kV using the secondary electron signal. This procedure resulted in 61 input images for the computation of a single tomogram. Tomograms were reconstructed with the IMOD software by weighted backprojection (Figs. 3, 4, 5A).

Low-Temperature SEM of Freeze-Dried Samples

For low-temperature SEM the extracted and freeze-dried samples were transferred under liquid nitrogen to the cold stage (Gatan, Inc., Pleasanton, CA, USA.) of the Hitachi S-5200 SEM and quickly inserted into the microscope. Specimens were investigated at a temperature of 173 K at an accelerating voltage of 30 kV using the secondary electron

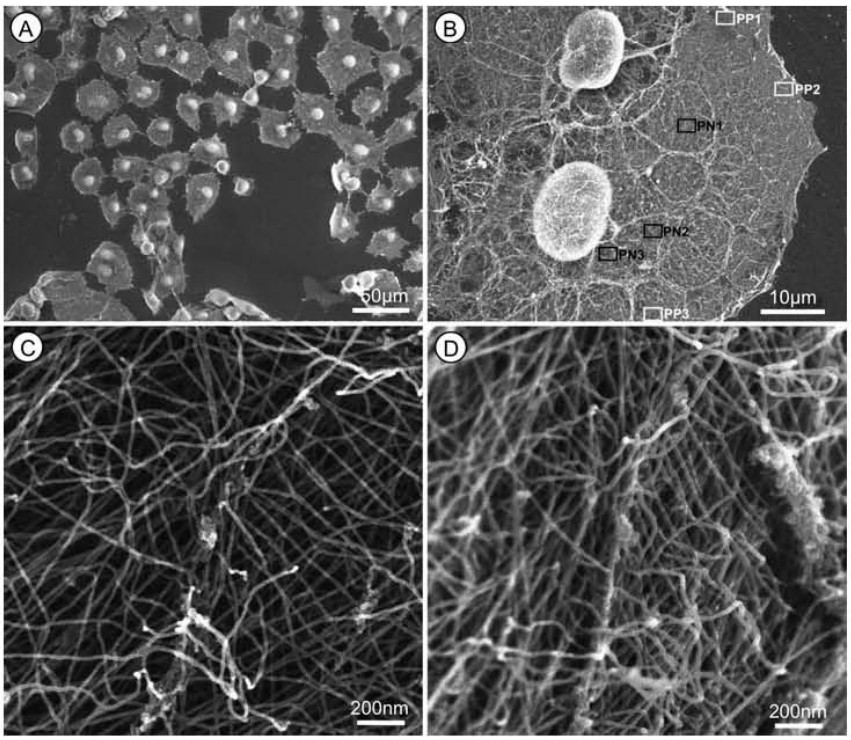

Figure 3. **A:** An overview of extracted Panc 1 cells. **B:** A cell where several tomograms were recorded at different perinuclear (PN, black boxes) and peripheral (PP, white boxes) areas. **C,D:** Images at 0° tilt angle (**C**) and at 60° tilt angle (**D**) of the recorded tilt series (60° +60°; 2° steps) of tomogram PP2 in panel **B**. All images were recorded with an SEM at 5 kV using the secondary electron signal.

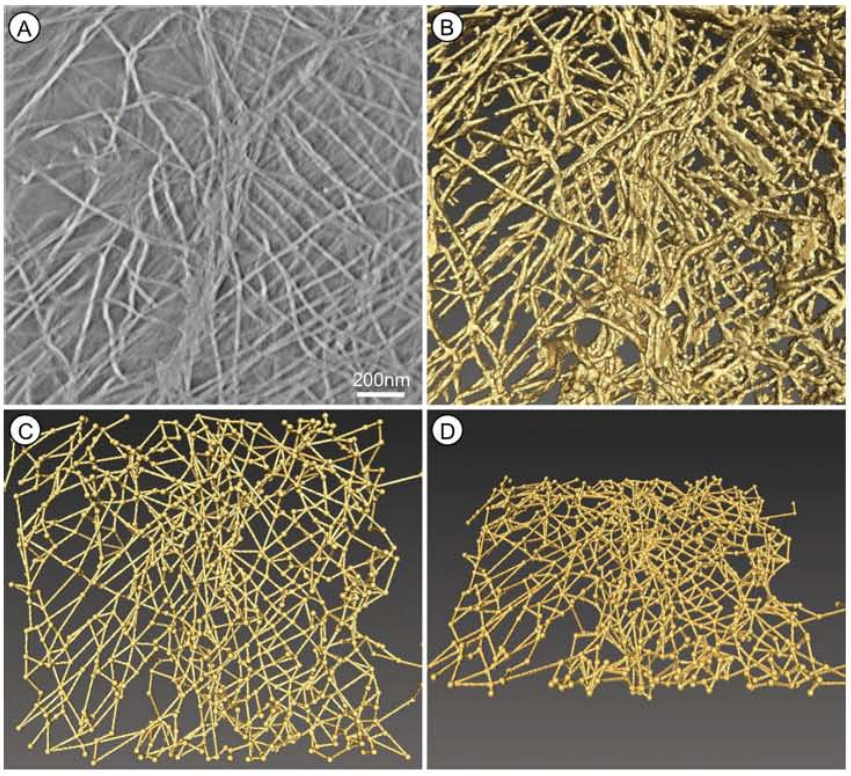

Figure 4. **A:** One layer of a reconstructed tomogram of the region PP2 in Figure 3B. **B:** The tomogram after thresholding. **C,D:** The network graph calculated from the thresholded tomogram, visualized under different tilt angles.

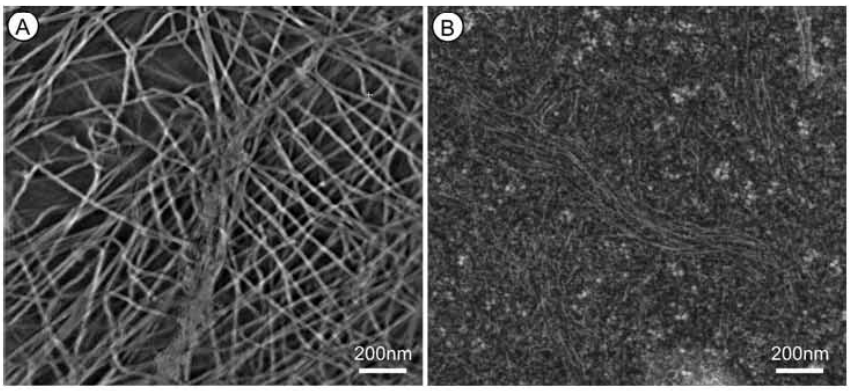

Figure 5. **A:** An artificially generated section (about 80 nm thick) of tomogram PP2, from a detergent extracted and critical-point-dried sample. **B:** An image of an ultrathin section (thickness about 80 nm) of a high-pressure frozen and freeze substituted Panc 1 cell, imaged with an SEM at 30 kV with a dark-field STEM detector. Both images visualize the same field size and the same thickness after different preparation and visualization methods. The filaments in the secondary electron SEM image **(A)** appear thicker than the ones in the transmission electron image **(B)**. This is due to carbon coating, as explained in Figure 1E. Besides this difference, both images show similar appearance of the filaments.

signal as described by Walther (2008) (Fig. 6B,C). The data are compared with a sample of *in-vitro* polymerized F-actin that has been frozen, freeze dried, and coated with tungsten like the samples described above (Walther, 2008) (Fig. 6A).

Results and Discussion

Here we present different electron microscopical approaches for the 3D morphological data aquisition of keratin intermediate filament networks. In earlier work we quantitatively analyzed the keratin filament network of pancreatic cancer cells in two dimensions (Beil et al., 2005, 2006) and are ready to expand these studies to 3D datasets as we have started in Lück et al. (2010). One motivation for this study is the influence of the structure of the keratin filament network on cell mechanics, an important factor for tumor cell migration (Beil et al., 2003).

STEM Tomography

To visualize the cytoskeleton in the full context of all cell components, we performed high-pressure freezing, freeze substitution, and STEM tomography. It is generally acknowledged that cryo-fixation is the best immobilization method to preserve the structural integrity of a cell (e.g., Echlin, 1992; Hohenberg et al., 2003; Dubochet, 2007). The most widely established protocol is to process a cryo-fixed sample by freeze substitution (Humbel, 2009). The samples are afterward embedded in plastic, thin sectioned, and can be investigated by regular TEM, low-voltage STEM, or by (S)TEM tomography. Figure 1A,B show virtual sections of 300 kV STEM tomograms of 500 nm sections of Panc 1 cells. Figure 1A depicts the perinuclear area of a cell, where many keratin filaments are expected. Beside other well-preserved structural features such as mitochondria, densely packed filament strands are observed. It is difficult, however, to track a single filament through the whole tomogram. It is not absolutely clear whether the observed filaments represent intermediate filaments or F-actin. Figure 1B shows filaments in microvilli, which must represent F-actin (Alberts et al., 2008).

Improvements by Low-Voltage STEM and SEM

Since it was difficult to track the filaments with 300 kV STEM tomography, we switched to an alternative method: low-voltage STEM. It is expected that contrast is enhanced at low accelerating voltages (30 kV compared to 300 kV). Figure 1C,D are low-voltage STEM dark-field images of ultrathin sections from the perinuclear area of Panc 1 cells. The recorded cell area in Figure 1C is similar in size to Figure 1A,B, but the thickness of the section is only 80 nm. The contrast of the filaments is reasonably good, but obviously 3D information is missing in the ultrathin section. Performing tomography at 30 kV is difficult with our equipment for technical reasons, and in addition we assume that spreading of the primary beam would make tomographic imaging of semithin sections at 30 kV unsatisfactory. Therefore, we used the extraction protocol, where most of the cellular compounds are washed out and basically only the keratin filament network remains (Svitkina & Borisy, 1998; Svitkina, 2007) unless F-actin is stabilized by adding phalloidin. Figure 1E,F shows the same area of an extracted Panc 1 cell recorded simultaneously. Figure 1E is an image of the transmission dark-field (STEM) signal, and Figure 1F is the image of the conventional secondary electron signal. The

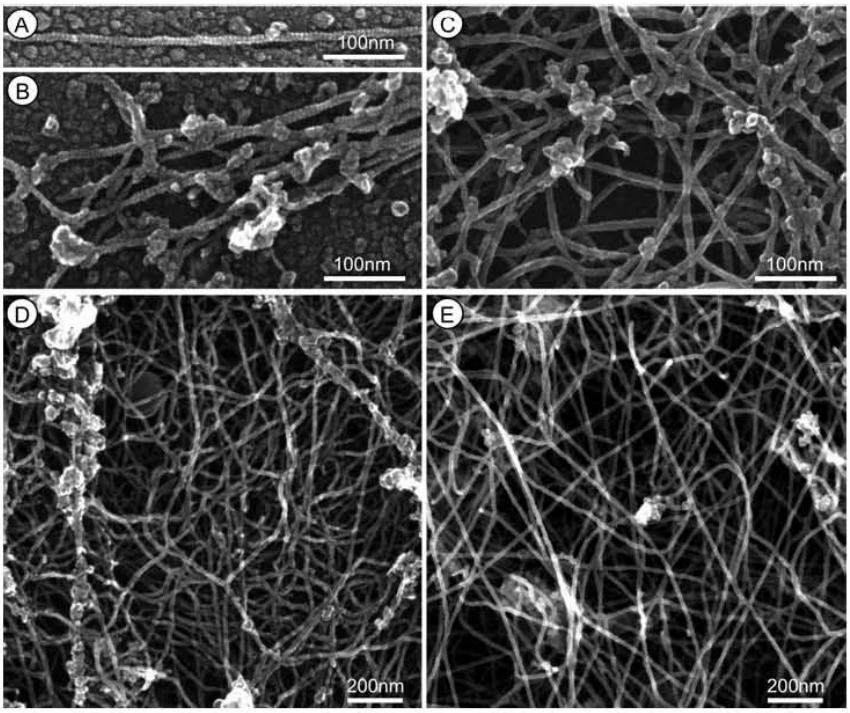

Figure 6. **A:** An isolated actin filament after freeze drying. The typical helical arrangement of the individual G-actin subunits can be seen clearly and give the filament the typical saw-toothlike appearance. **B,C:** Different areas from the same extracted Panc 1 cell preparation after freeze drying. Panel **B** is from the cell periphery, where mainly actin filaments are expected. Indeed, most of the filaments in this area exhibit saw-toothlike surface structures. Panel **C** is from a perinuclear area, where we mainly expect keratin (intermediate) filaments. Most of the filaments show a smooth appearance. **D,E:** SEM images of (**D**) freeze-dried and (**E**) critical-point-dried extracted networks. Both images show similar branching and directional distribution of the filaments. All images were recorded with an SEM using the secondary electron signal.

diameter of the filaments is about 10 nm in the transmitted image and about 20 nm in the secondary electron image. This is due to the carbon coat that is transparent for the transmitted electrons but produces secondary electrons. The bright dots, which most likely represent contaminations due to incomplete extraction, are imaged with about the same contrast in both pictures, but obviously the thin filaments are best visualized using the secondary electron signal because they have a small volume, but a large surface area. The electrons used for contrast formation in bright-field and dark-field transmission imaging are scattered in function of the mass density, which is low in these thin filaments. Contrast in transmission mode, therefore, is low, and the filaments are almost vanishing beside unextracted cell compounds, which have a large volume and therefore high contrast (Fig. 1E). The secondary electron signal, however, is primarily a function of the surface area exposed to the electron beam (Seiler, 1967). The secondary electron emission of the filaments is high because their surface is large compared to the volume (Fig. 1F). Figure 2A shows an overview of an extracted Panc 1 cell imaged at an accelerating voltage of 5 kV with the secondary electron signal. It turned out that in our hands an accelerating voltage of 5 kV gave the best results with extracted samples at low and intermediate magnifications because the contrast was even more increased and charging problems were reduced compared to 30 kV (compare with Fig. 1F). This is in agreement with data from the literature (Pawley, 2008). The marked area is displayed at a higher magnification in Figure 2B. Figure 3A represents an overview of several Panc 1 cells grown on a sapphire disc.

SEM Tomography of Keratin Intermediate Filament Networks

The principle of computed tomography was first discovered by Radon (1917) in his work on the reconstruction of a function from projection data. The most essential assumption arising from this mathematical foundation of tomographic reconstruction is that the input data consist of line

integrals of some image property through the volume of interest. The single projection images serving as input for reconstruction algorithms such as weighted backprojection or algebraic reconstruction techniques (Buzug, 2008) are obtained by parallel scanning of the sample with a line while taking the integrals. The Radon transform of an object is the collection of these projections that is obtained by tilting the sample in the interval $[-90°, +90°)$ with respect to a central axis. Computed tomography deals with the problem of inverting the Radon transform.

At the level of resolution needed to study keratin networks, the signal collected in STEM mode by a HAADF detector can be directly related to the projection of the density through the specimen along the path of the electron beam, thus approximating line integration by an integral over the electron probe (Hawkes, 2005). However, the secondary electron signal recorded as the input data for SEM tomograms is of quite different nature. The escape probability of secondary electrons decreases exponentially with the depth of the location where the secondary electron is generated (Goldstein et al., 2007). Therefore, the secondary electron signal primarily maps surfaces and contains a rather negligible amount of information on deeper layers of the specimen. As a consequence, in usual situations secondary electron imaging does not yield projections of the specimen that could be used as input for tomographic reconstruction algorithms. However, detergent extracted samples of keratin filaments only contain the fine network structure surrounded by vacuum. As a consequence, single surface locations along the filaments are freely accessible to the electron probe under most tilt angles. Thus, even under high tilt angles, filaments in deeper areas are clearly visible (Fig. 3C,D), and the secondary electron signal closely resembles projection data of the specimen. Compared to real projection data, the contrast of filaments in lower network components is decreased by shadowing effects of network parts (Fig. 3C). In comparison to STEM, the crucial advantage of secondary electron imaging is the enhanced contrast of the filaments (Fig. 1E versus Fig. 1F). This high contrast got transferred to tomograms computed from secondary electron tilt series, which were recorded by tilting in the interval $[-60°, 60°]$ at an angular increment of 2° and computed by weighted backprojection (Buzug, 2008) (Fig. 4A). Thus, the tomograms were generated by a standard algorithm for the reconstruction of TEM or STEM data.

A specific artifact in SEM tomograms is that shadowing of filaments in deeper layers by upper network components decreases contrast and leads to stretched filament profiles. The oval stretch of reconstructed filament profiles in SEM tomograms is a well-known artifact from tomographic reconstructions with a missing wedge of tilt angles, which also occurs in computed tomography from regular TEM tilt series (Midgley & Dunin-Borkowski, 2009). However, in SEM tomograms these effects are more pronounced due to mutual shadowing of the image components. As a consequence, SEM tomography for the 3D analysis of filamentous networks is not primarily limited by sample thickness but by network density, which controls visibility of single filaments during tilting. For more details we refer to Lück et al. (2010).

Quantitative Analysis of Network Structure Based on SEM Tomograms

Based on high-contrast SEM tomograms, the graph structure of the networks can be extracted by techniques from image analysis. Figure 4B depicts the tomogram after thresholding. Figure 4C,D visualizes the network graph extracted from the thresholded tomogram by means of an algorithm discussed in Lück et al. (2010). Apart from the segmentation of the foreground phase by thresholding, the algorithm applied to generate Figure 4C,D is fully automatic and thus reduces potential bias from user interaction. Given the extracted network graph, statistical analysis of network characteristics such as network density, filament length, and cross-link topology can be conducted. Since such characteristics are related to the mechanical behavior of the network, these techniques represent promising approaches to quantitatively link network morphology to mechanical properties of the cytoplasm and the migration ability of cells, which can be measured in biophysical experiments (Marti et al., 2008; Lautenschläger et al., 2009).

Preparation Artifacts

Possible artifact formation of extraction and critical point drying protocols have been described in the literature, such as surface tension artifacts caused by traces of water during critical point drying (Ris, 1985) as well as fracturing of actin filaments, leading to branch-like structures (Resch et al., 2002; Vignal & Resch, 2003). To obtain more confidence in our preparation protocol, we compared extracted samples with the results of freeze substitution (Fig. 5) and freeze-drying experiments (Fig. 6).

In Figure 5 we compare two different preparation and visualization methods for a similar volume in a Panc 1 cell. Figure 5A is an artificially generated section (about 80 nm) of tomogram PP2 (the sample was detergent extracted), whereas Figure 5B is an image of an ultrathin section (thickness about 80 nm) of a high-pressure frozen and freeze substituted Panc 1 cell. Both images, therefore, represent the same surface area and the same thickness after different preparation and visualization methods. Taking into account that the filaments appear thicker in the secondary electron SEM image (Fig. 5A) due to the carbon coating, as explained above, both images show similar variation of filament density. Moreover, under both preparation methods the filaments form rather long tracks, which are partially organized in parallel strands. We conclude, therefore, that fracturing of filaments as postulated by Resch et al.

(2002) for F-actin in critical point dried samples does not occur in these intermediate filament samples.

In Figure 6 we compared our results for critical-point-dried samples with freeze-dried controls. We added phalloidin to the extraction medium to better preserve the actin filament structure. As described earlier (Walther, 2003, 2008), the helical arrangement of individual actin subunits is well visible in isolated actin filaments after freeze drying and coating with a very thin layer of tungsten (Fig. 6A), but not after critical point drying. Figure 6B,C shows different areas from the same extracted and freeze-dried Panc 1 cell preparation. Figure 6B is from the cell periphery where mainly actin filaments are expected, and, indeed, we find saw toothlike surface structures on most of the filaments in this area. Figure 6C is from a perinuclear area, where we mainly expect keratin (intermediate) filaments. In fact, most of the filaments in this image show a smooth appearance.

Figure 6D,E shows SEM images of freeze-dried (Fig. 6D) and critical-point-dried (Fig. 6E) networks. Comparing central regions after freeze drying (Fig. 6D) and after critical point drying (Fig. 6E), the keratin filament network appeared similar after both preparations and, most notably, we could not observe more branching in critical-point-dried samples. Based on these results we suppose that the keratin filament network is more stable than the actin network and, therefore, less affected by chemical and mechanical disturbance during extraction, fixation, dehydration, and drying.

Conclusions

In an earlier work (Lück et al., 2010), we performed statistical analysis of 3D keratin filament networks. These samples had been prepared by the extraction protocol combined with critical point drying and imaged by SEM tomography. These techniques yield a high level of contrast in tomograms, which is necessary for the extraction and analysis of the network structure by means of image analysis and spatial statistics but cannot be achieved by the other methods discussed in the present study. Here we confirmed that the network structure of keratin (intermediate) filaments appears similar after being prepared by different preparation protocols. This gives confidence that the 3D structure of the network is well preserved by all of the different preparation protocols used in this work, including SEM tomography of extracted cells.

Acknowledgments

We thank Renate Kunz, Elke Wolff-Hieber, Eberhard Schmid, and Reinhard Weih for excellent technical assistance. We thank Guido Adler for continuous support. This work was supported by the DFG SFB 518, projects B21 and B22.

References

Alberts, B., Johnson, A., Lewis, L., Raff, M., Roberts, K. & Walter, P. (2008). *Molecular Biology of the Cell*, 5th Ed. New York: Garland Publishing.

Baumeister, W. (2004). Mapping molecular landscapes inside cells. *Biol Chem* **385**, 865–872.

Beil, M., Braxmeier, H., Fleischer, F., Schmidt, V. & Walther, P. (2005). Quantitative analysis of keratin filament networks in scanning electron microscopy images of cancer cells. *J Micros* **220**, 84–95.

Beil, M., Eckel, S., Fleischer, F., Schmidt, H., Schmidt, V. & Walther, P. (2006). Fitting of random tessellation models to keratin filament networks. *J Theor Biol* **241**, 62–72.

Beil, M., Micoulet, A., von Wichert, G., Paschke, S., Walther, P., Omary, M.B., Van Veldhoven, P.P., Gern, U., Wolff-Hieber, E., Eggermann, J., Waltenberger, J., Adler, G., Spatz, J. & Seufferlein, T. (2003). Sphingosylphosphorylcholine regulates keratin network architecture and visco-elastic properties of human cancer cells. *Nat Cell Biol* **5**, 803–811.

Buser, C. & Walther, P. (2008). Freeze-substitution: The addition of water to polar solvents enhances the retention of structure and acts at temperatures around −60 °C. *J Mircrosc* **230**, 268–277.

Buzug, T.M. (2008). *Computed Tomography*. Berlin: Springer.

Coulombe, P.A. & Omary, M.B. (2002). "Hard" and "soft" principles defining the structure, function and regulation of keratin intermediate filaments. *Curr Opin Cell Biol* **14**, 110–122.

Dubochet, J. (2007). The physics of rapid cooling and its implications for cryoimmobilization of cells. *Methods Cell Biol* **79**, 7–21.

Echlin, P. (1992). *Low-Temperature Microscopy and Analysis*. New York, London: Plenum Press.

Fuchs, E. & Weber, K. (1994). Keratin (intermediate) filaments: Structure, dynamics, function and disease. *Annu Rev Biochem* **63**, 345–382.

Goldstein, J., Newbury, D., Joy, D., Lyman, C., Echlin, P., Lifshin, E., Sawyer, L. & Michael, J. (2007). *Scanning Electron Microscopy and X-Ray Microanalysis*, 3rd Ed. New York: Springer.

Hatzfeld, M. & Franke, W.W. (1985). Pair formation and promiscuity of cytokeratins: Formation in vitro of heterotypic complexes and keratin (intermediate)-sized filaments by homologous and heterologous recombinations of purified polypeptides. *J Cell Biol* **101**, 1826–1841.

Hawkes, P.W. (2005). The electron microscope as a structure projector. In *Electron Tomography*, 2nd Ed., Frank, J. (Ed.), pp. 83–107. New York: Springer.

Herrmann, H., Hesse, M., Reichenzeller, M., Aebi, U. & Magin, T.M. (2003). Functional complexity of keratin (intermediate) filament cytoskeletons: From structure to assembly to gene ablation. *Int Rev Cytol* **223**, 83–175.

Hohenberg, H.H., Müller-Reichert, T., Schwarz, H. & Zierold, K. (2003). Foreword, special issue on high pressure freezing. *J Microsc* **212**, 1–2.

Höhn, K., Pusapati, G.V., Seufferlein, T., Adler, G. & Walther, P. (2009). 3D reconstruction of Golgi stacks in Brefeldin A treated cells. First results using STEM tomography. In *Proceedings of MC2009*, vol. 2, Life Science, Pabst, M.A. & Zellnig, G. (Eds.), pp. 43–44. Graz, Austria: Verlag der TU.

Hoppe, W., Gassmann, J., Hunsmann, N., Schramm, H.J. & Sturm, M. (1974). Three-dimensional reconstruction of individual negatively stained yeast fatty-acid synthetase molecules from tilt series in the electron microscope. *Z Physiol Chem* **355**, 1483–1487.

Humbel, B.M. (2009). Freeze substitution. In *Handbook of Cryo-Preparation Methods for Electron Microscopy*, Cavalier, A., Spehner, D. & Humbel, B.M. (Eds.), pp. 319–341. Boca Raton, FL: CRC Press.

Kremer, J.R., Mastronarde, D.N. & McIntosh, J.R. (1996). Computer visualization of three-dimensional image data using IMOD. *J Struct Biol* **116**, 71–76.

Lautenschläger, F., Paschke, S., Schinkinger, S., Bruel, A., Beil, M. & Guck, J. (2009). The regulatory role of cell mechanics for migration of differentiating myeloid cells. *Proc Natl Acad Sci USA* **106**, 15696–15701.

Lück, S., Sailer, M., Schmidt, V. & Walther, P. (2010). Three-dimensional analysis of intermediate filament networks using SEM tomography. *J Microsc* **236**, 1–16.

Marti, O., Holzwarth, M. & Beil, M. (2008). Measuring the nanomechanical properties of cancer cells by digital pulsed force mode imaging. *Nanotechnology* **19**, 384015.

Midgley, P.A. & Dunin-Borkowski, R.E. (2009). Electron tomography and holography in materials science. *Nat Mater* **8**, 271–280.

Midgley, P.A., Weyland, M., Thomas, J.M. & Johnson, B.F.G. (2001). Z-contrast tomography: A technique in 3-dimensional nanostructural analysis based on Rutherford scattering. *Chem Comm* **18**, 907–908.

Pawley, J. (2008). LVSEM for biology. In *Biological Low-Voltage Scanning Electron Microscopy*, Schatten, H. & Pawley, J.B. (Eds.), pp. 27–106. New York: Springer.

Radon, J. (1917). Über die Bestimmung von Funktionen längs gewisser Mannigfaltigkeiten. *Berichte der math.-phys. Kl. Sächsischen Gesellschaft der Wissenschaften* **59**, 262–277.

Resch, G.P., Goldie, K.N., Krebs, A., Hoenger, A. & Small, J.V. (2002). Visualisation of the actin cytoskeleton by cryo-electron microscopy. *J Cell Sci* **115**, 1877–1882.

Ris, H. (1985). The cytoplasmic filament system in critical point-dried whole mounts and plastic-embedded sections. *J Cell Biol* **100**, 1474–1487.

Sailer, M., Lück, S., Schmidt, V., Beil, M., Adler, G. & Walther, P. (2008). Three-dimensional analysis of the keratin (intermediate) filament network using SEM-tomography. In *Proceedings of EMC 2008*, Aretz, A., Hermanns-Sachweh, B. & Mayer, J. (Eds.), pp. 91–92. Berlin, Heidelberg: Springer.

Sailer, M., Lück, S., Schmidt, V., Beil, M., Adler, G. & Walther, P. (2009). Three-dimensional analysis of the keratin (intermediate) filament network using SEM-tomography. In *Proceedings of MC2009*, Pabst, M.A. & Zellnig, G. (Eds.), pp. LI.P603–LI.P604. Graz, Austria: Verlag der TU.

Seiler, H. (1967). Einige aktuelle Probleme der Sekundärelektronenemission. *Z Angew Phys* **22**, 249–263.

Svitkina, T.M. (2007). Electron microscopic analysis of the leading edge in migrating cells. *Methods Cell Biol* **79**, 295–319.

Svitkina, T.M. & Borisy, G.G. (1998). Correlative light and electron microscopy of the cytoskeleton of cultured cells. *Method Enzymol* **298**, 570–592.

Vignal, E. & Resch, G. (2003). Shedding light and electrons on the lamellipodium: Imaging the motor of crawling cells. *Biotechniques* **34**, 780–784, 786, 788–789.

Walther, P. (2003). The potential of high resolution cryo-SEM in life science. *Hitachi Instrument News* **40**, 3–8.

Walther, P. (2008). High-resolution cryo-SEM allows direct identification of F-actin at the inner nuclear membrane of Xenopus oocytes by virtue of its structural features. *J Microsc* **232**, 379–385.

Walther, P. & Ziegler, A. (2002). Freeze substitution of high-pressure frozen samples: The visibility of biological membranes is improved when the substitution medium contains water. *J Microsc* **208**, 3–10.

Windoffer, R., Wöll, S., Strnad, P. & Leube, R.E. (2004). Identification of novel principles of keratin filament network turnover in living cells. *Mol Biol Cell* **5**, 2436–2448.

Yakushevska, A.E., Lebbink, M.N., Geerts, W.J., Spek, L., van Donselaar, E.G., Jansen, K.A., Humbel, B.M., Post, J.A., Verkleij, A.J. & Koster, A.J. (2007). STEM tomography in cell biology. *J Struct Biol* **159**, 381–391.

Journal of Microscopy, 2009
Received 17 June 2009, accepted 1 October 2009
doi: 10.1111/j.1365-2818.2009.03348.x

Three-dimensional analysis of intermediate filament networks using SEM tomography

S. LÜCK*, M. SAILER†, V. SCHMIDT* & P. WALTHER†
**Institute of Stochastics, Ulm University, Ulm, Germany*
†*Electron Microscopy Facility, Ulm University, Ulm, Germany*

Key words. Cytoskeleton, intermediate filaments, network morphology, SEM tomography.

Summary

We identified tomographic reconstruction of a scanning electron microscopy tilt series recording the secondary electron signal as a well-suited method to generate high-contrast three-dimensional data of intermediate filament (IF) networks in pancreatic cancer cells. Although the tilt series does not strictly conform to the projection requirement of tomographic reconstruction, this approach is possible due to specific properties of the detergent-extracted samples. We introduce an algorithm to extract the graph structure of the IF networks from the tomograms based on image analysis tools. This allows a high-resolution analysis of network morphology, which is known to control the mechanical response of the cells to large-scale deformations. Statistical analysis of the extracted network graphs is used to investigate principles of structural network organization which can be linked to the regulation of cell elasticity.

Introduction

The cytoskeleton of eucaryotic cells is composed of three biopolymer systems: the network of actin filaments, the system of microtubuli and the network of intermediate filaments (IFs). This study focusses on the network of IFs, which have a diameter of between 10 and 12 nanometres (nm) (Coulombe & Omary, 2002) and are formed by a heterogenous group of proteins with a tissue-specific expression. In epithelial cells and their tumours like the human pancreatic cancer cells considered in this study, IFs mainly consist of keratins K8 and K18 (Fuchs, 1994).

IFs possess a particularly high extensibility and resistance to breakage (Herrmann *et al.*, 2007 and references therein). Therefore, they govern the elastic properties of a cell when it is exposed to deformations of large scale and override the impact of the actin network (Beil *et al.*, 2003; Suresh *et al.*, 2005). IF as well as actin networks are formed of semi-flexible polymers. It is known from numerical simulations and experimental studies that networks composed of semi-flexible polymers exhibit a much stronger interplay between network morphology and elasticity than observed in flexible polymer networks (Gardel *et al.*, 2004; Heussinger & Frey, 2006, 2007). It is therefore of interest to develop methods for the visualization and image analysis of IF networks, which allow for detailed assessment of morphological network characteristics. In previous studies, this was done based on two-dimensional (2D) scanning electron microscopy (SEM) (Beil *et al.*, 2005, 2006). This is an appropriate technique for networks observed in the cell periphery, which exhibit an almost planar structure. Nevertheless, in other cellular compartments IF networks can possess a genuinely three-dimensional (3D) architecture. Numerical simulations revealed that the mechanical behaviour of 3D biophysical networks can be intrinsically tied to morphological characteristics of 3D nature (Huisman *et al.*, 2007). These characteristics comprise connectivity and segment length, which for non-planar networks can only be adequately assessed from 3D image data. In this study, we introduce a method that allows to monitor the 3D structure of IF networks and we statistically investigate the interplay of certain mechanically relevant network characteristics in pancreatic cancer cells.

Since the diameter of IFs and interfilament distances are smaller than the diffraction limit of light microscopy, an analysis of network morphology at the level of single filaments and their cross-links cannot be achieved by fluorescence imaging of living cells (Windoffer *et al.*, 2004; Wöll *et al.*, 2007). A widely applied electron microscopical method to visualize cytoskeletal filament networks such as IFs is detergent extraction of the cells, followed by chemical fixation

The first two authors contributed equally.

Correspondence to: S. Lück, Institute of Stochastics, Ulm University, D-89069 Ulm, Germany. Tel: +49 731 502 3555; fax: +49 731 502 3649; e-mail: sebastian.lueck@uni-ulm.de

and critical point drying. The samples are then coated with a thin layer of heavy metal or carbon and can be visualized either in the SEM or, after replication, in the transmission electron microscope (TEM; e.g. Svitkina & Borisy, 1999).

The natural approach to obtain 3D image data of IF networks would be tomographic reconstruction of a TEM or scanning TEM (STEM) tilt series. Transmission images are appropriate for tomography since they are projections of the specimen as required by all tomographic reconstruction algorithms. However, the volume-dependent transmission electron signal yields rather low contrast of the thin filaments in comparison to the strong signal of non-IF cytoplasmic components that are not completely removed during extraction. We therefore suggest an approach using the surface-dependent secondary electron signal, which is relatively strong from the filaments. Due to the extraction protocol, single filaments are visible on secondary electron images under most tilt angles. Thus, these tilt images can be viewed as good approximations for projections of a modified density, which highlight the filamentous structures. Reconstructions of secondary electron tilt series yielded substantially increased filament contrast in comparison to TEM and STEM.

Although SEM also comprises techniques which do not use secondary electrons such as STEM, for the ease of wording, we will sometimes replace the term 'secondary electron' by the simple prefix 'SEM'. Thus, in this work, whenever the term 'SEM' is used, we refer to secondary electron data such as single tilt images or tomograms.

Analysis of network morphology requires the extraction of the network connectivity graph from the tomograms. For this purpose, we combined standard techniques from image analysis, namely thresholding and skeletonization, with a specifically designed algorithm that reduces artefacts arising from errors in continuity tracking and tomographic reconstruction of secondary electron tilt series. Based on this data, we statistically investigated the morphology in different samples of IF networks. This statistical analysis revealed principles of network organization, which can be linked to the regulation of cell elasticity.

Material and methods

Cell culture

Panc 1 human pancreatic cancer cells (American Type Culture Collection, Manassas, VA, USA) were grown as a monolayer on glow discharged sapphire discs coated with carbon as described by Buser *et al.* (2007).

Cell preparation

The preparation of cells to visualize the keratin network by high-resolution SEM by a prefixation extraction method (Ris, 1985) was partially based on the protocol of Svitkina & Borisy (1998). After washing with phosphate-buffered saline (PBS; pH 7.3), the cells were extracted for 25 min at around 8°C with 1% Triton-X 100 (in PBS). Cells were washed again with PBS and fixed with 2.5% glutar aldehyde (in PBS, with distilled water and 1% saccharose) for 1 h at room temperature. After washing with PBS, the cells were contrasted with OsO_4 (2% in PBS) for 1 h at room temperature. After another washing step with PBS, the samples were gradually dehydrated in 30%, 50%, 70%, 90% and 100% propanol (for 5 min at each step). Then the cells were critical-point dried using carbon dioxide as translation medium (Critical Point Dryer CPD 030, BalTec, Principality of Liechtenstein). Finally, the samples were perpendicularly coated with a thin layer of carbon by electron beam evaporation (5 nm; BalTec Baf 300).

Electron microscopy

To analyze the filamentous structure of the keratin network, the samples were imaged with a Hitachi S-5200 in-lens SEM (Tokyo, Japan) at an accelerating voltage of 5 kilovolts (*kV*) using the secondary electron signal. Since the stage of the SEM allows only a maximal tilt of 40°, we mounted the samples on a pretilted (35°) specimen holder. After having recorded the series from +60° to 0°, the sample was rotated by 180° and remounted in order to record the second series from 0° to −60°. (At tilt angles above 60° contrast became very poor most likely due to self-shadowing effects.) Tilt series were recorded with 2° step size at a magnification of 50,000. In total, 11 tomograms were recorded. Tomograms were reconstructed by weighted backprojection (WBP) with the IMOD software (Kremer *et al.*, 1996) (Figs 5(a) and (b)).

Image segmentation

Image processing in Avizo

As a first step towards extracting the graph structure of the IF network from the tomograms, image filters provided by the Avizo software package (Mercury computer systems, 2008) were applied. Noise was reduced by an edge-preserving smoothing algorithm which consists of Gaussian filtering followed by an anisotropic diffusion, which guarantees that diffusion stops at edges within the image. Afterwards, the image was binarized by thresholding and subsequent elimination of small islands in the foreground phase as well as some smoothing of the boundary (Figs 1(a) and 5(d)). Since due to shadowing effects the secondary electron signal from filaments in lower layers of the cell tends to be weaker than the signal from upper parts of the network, thresholding was done semi-automatically, i.e. thresholds were adapted manually to the brightness level of the different network components, which were then automatically identified based on connectivity. In the next

Fig. 1. Extraction of the graph structure from a detailed section of a secondary electron tomogram. (a) Detail of a tomogram after thresholding. (b) Skeleton of the foreground phase. (c) Extracted network graph after all processing steps, cross-links highlighted by spheres.

step, a homotopic, i.e. connectivity-preserving, skeleton of the filamentous phase was computed by the skeletonization package of Avizo (Fourard *et al.*, 2006) (Fig. 1(b)). The skeletonization result was reduced to its graph structure and exported as vector data, where the filament trajectories were represented as polygon tracks. The subsequent steps of image processing were based upon the graph of the skeletonization result obtained in this way and implemented in the Geostoch software library (Mayer *et al.*, 2004). An example of a final segmentation result can be seen in Fig. 1(c). Several corrections were applied to the graph structure obtained from the Avizo software in order to compensate for artefacts resulting from binarization, skeletonization or missing information which would have been needed for unbiased tomographic reconstruction.

Removal of loops and linearization of filaments

The images of the tilt series suggested that loops, i.e. filaments starting and ending at the same point had to be regarded as artefacts. Therefore, all loops were removed from the network graph. Moreover, since filaments exhibited only negligible curvature, network vertices of degree 2, i.e. nodes joining exactly two edges, were removed from the graph unless the corresponding line segments enclosed an angle of less than 270°. Whenever a vertex of degree 2 was removed, the corresponding connection was replaced by a single line segment.

Optimization of segment positions

Although the filaments on the tilt series images exhibited hardly any curvature, the line segments of the graph representing the filaments still had to be regarded as linear approximations of the actual filament shapes. Since they were constructed as straight connections between filament linking points their position did possibly not optimally resemble the filament trajectories in the threshold images. An algorithm was designed in order to improve the position of all line segments within the filamentous phase of the tomograms. Details are given in Appendix A. The algorithm takes particular care to centre the extracted network segments in z-direction within the filamentous phase since binarized tomograms exhibited some filament profiles whose height exceeded their width by up to factor 3, although in reality the profile of IFs is circular. This inaccuracy of the resolution in z-direction is a consequence of the limited tilt range in electron tomography (the missing wedge problem, see e.g. Bartesaghi *et al.* (2008) and Midgley & Dunin-Borkowski (2009)) and a certain oversegmentation in upper network layers, which could not be avoided if threshold values were used which still allowed for identification of lower network components exhibiting reduced contrast. The optimization algorithm for segment positioning was repeated after each step of graph modification described below.

Merging of closely located cross-links

Since some filaments are entangled in such a way that they enclosed small angles, filament links located very closely to each other were regarded as artefacts. Therefore, as suggested in Beil *et al.* (2005), such pairs of filament links were merged into a single one located in their centre of gravity (Fig. 2). Taking into account that after carbon coating filaments had a diameter between 20 nm and 25 nm merging was performed

Fig. 2. Merging of closely located cross-links.

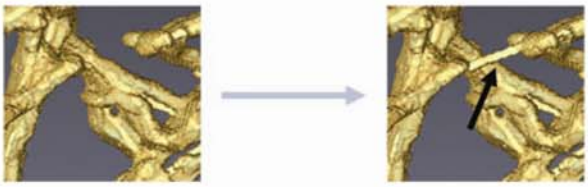

Fig. 3. Extrapolation of a dead end.

for network nodes of a distance less than $d = 36$ nm apart in ascending sequence, i.e. link pairs of smaller distance were merged first. Afterwards segment positions were optimized as described in the preceding section.

Dead ends

In SEM images of IF networks, one hardly observes filament ends which are not connected to other network components. In spite of this, in the network graphs extracted from the SEM tomograms such dead ends occurred. A certain fraction of these were well-known artefacts of the skeletonization algorithm (Soille, 1999). However, some dead ends also resulted from principle limitations of the technique of SEM tomography. In contrast to TEM, the SEM tilt series does not consist of projections of the specimen but measures the surface-dependent secondary electron signal. As a consequence, due to shadowing effects in areas of dense network structure lower filament layers were partially not visible or only at less contrast. Therefore, some trajectories of lower level filaments were truncated in the binarized tomograms (Fig. 3). These artefacts were reduced by an algorithm which establishes extrapolations of dead ends within the network graph and checks them for plausibility. A detailed description of the algorithm can be found in Appendix B. Dead ends, which did not have a plausible extrapolation as defined by this algorithm, were regarded as skeletonization artefacts and removed from the network graph unless they were close to the boundary of the observation window.

Statistical analysis of network morphology

By means of 3D numerical finite element simulations of semi-flexible polymer networks, correlations between network stiffness and the three morphological characteristics network density, defined in terms of filamentous polymer concentration in the system, average segment length and connectivity have been demonstrated (Huisman *et al.*, 2007). These results motivated our choice of network characteristics for the analysis of IF network morphology. Their definitions will now be made precise. Since after preparation of the cells and tomographic reconstruction the actual 3D volume of the cellular compartments is hard to be estimated, we defined network density as the total network length per base area. It should be emphasized that this definition of network density purely focusses on the amount of polymers forming the network and not on network architecture. Since the amount of filamentous polymers is controlled by synthesis and phosphorylation status of IF proteins (Coulombe & Omary, 2002), network density defined in this way can be directly linked to biological processes. Other measures of density such as cross-link density are not only tied to the amount of polymers but to structural characteristics of network architecture, which in this study are assessed separately by mean segment length and connectivity.

If mean segment length is measured as the total network length divided by the number of segments, one obtains a biased estimator. This is due to the fact that the length of filaments protruding the observation window is underestimated. In order to avoid these edge effects, the mean was only taken with respect to segments whose centre was located in a smaller sampling window. The base of this sampling window was chosen as the central $1.84 \times 1.2\ \mu m^2$ of the observation window, its height was not restricted since filaments did not protrude the observation window in the third dimension.

Network connectivity was measured by considering the mean vertex degree of the network, where the degree of a vertex (i.e. a cross-link in the network) is defined as the number of segments emanating from it.

Network density, mean segment length and mean vertex degree were computed for 11 tomograms of IF networks in pancreatic cancer cells. Our statistical analysis primarily focusses on the interplay of these characteristics, namely their mutual correlations. These can be exploited to infer the relation of different principles applied by the cells in order to vary network architecture, and thus change their elasticity. When working with relatively small sample sizes, estimated values for correlation coefficients of two random variables can be misleading due to stochastic variability. Meaningful results concerning the correlation of different morphological network characteristics can however be obtained by testing if the measure of correlation significantly differs from zero. Standard tests for correlation exploit the distribution of Pearsons's correlation coefficient. However, the latter depends on the bivariate distribution of the sample vectors to be investigated, which at small sample sizes can hardly be inferred. Naturally, for small sample sizes also asymptotic tests are inappropriate. As a remedy, instead of Pearson's correlation coefficient we considered Spearman's rank order correlation coefficient ρ_S and Kendall's coefficient of concordance τ (for a definition, see e.g. Sheskin, 2000). Under the assumption of uncorrelated, identically and continuously distributed sample vectors $(X_1, Y_1), \ldots, (X_n, Y_n)$ the distributions of Spearman's ρ_S and Kendall's τ do not depend on the distribution of the sample vectors. Therefore, for both of these measures of correlation nonparametric statistical tests are available, which can already be applied at small sample sizes (Sheskin, 2000). The detailed construction of the tests can be found in Hollander &

Wolfe (1973). The tests can be used to detect dependencies of the following type:

(a) There is a tendency of the larger values of $X_1, \ldots, X_n$ to be paired with the larger values of $Y_1, \ldots, Y_n$.
(b) There is a tendency of the larger values of $X_1, \ldots, X_n$ to be paired with the smaller values of $Y_1, \ldots, Y_n$.

The null hypothesis of the tests is 'no correlation between the two samples', i.e. $H_0 : \rho_S = 0$ or $H_0 : \tau = 0$, respectively. H_0 can be tested against the one-sided alternative of positive correlation (i.e. (a)), against the alternative of negative correlation (i.e. (b)) or against the two-sided alternative (i.e. (a) or (b)).

Results

We investigated several preparation and imaging protocols for preservation and recording of the 3D IF network. The first one was high-pressure freezing, freeze substitution, embedding and thin sectioning. We analyzed these samples with regular TEM, 300 kV Scanning TEM (STEM) and 30 kV STEM (Sailer *et al.*, 2009). It turned out, however, that on these samples it was difficult to track the individual filaments in the very complex context of all the retained cellular structures of unextracted cells. We analyzed, therefore, IF networks from detergent-extracted cells. When imaging these samples with a 300 kV STEM, the signal of the thin filaments was relatively poor, it could be increased by using a 30 kV STEM, but still the signal of the filaments was insufficient compared to the strong signal of non-IF cytoplasmic components that were not completely removed during extraction (Fig. 4(a)). Therefore, we used the secondary electron signal, which is surface-dependent and relatively strong from thin filaments (Fig. 4(b)). As a consequence of detergent extraction, even single filaments in some depth are clearly visible under most tilt angles. Therefore, they are captured by tomographic reconstructions of secondary electron tilt series (Fig. 5(c)). The data sets were recorded by tilting the sample similar to TEM-tomography. Weighted backprojection (WBP) was then used to construct a 3D model from the tilt series.

In our setting, the input signal of the reconstruction algorithm was not a projection of the specimen as required by the mathematical theory of WBP, but a surface-dependent signal (Joy & Pawley, 1992). Simulated signals were used to clarify the impact of the violated projection requirement on the reconstruction of single filaments. In the parallel beam geometry of single-axis electron tomography, the reconstruction of a 3D volume is done by separate reconstruction of parallel 2D slices from their one-dimensional (1D) projections. In most orientations of a filament with respect to the tilt axis, its intersection with a 2D slice of the considered volume is an ellipse. Therefore, we simulated the surface-dependent and the projection signal of a 2D circle and compared the corresponding WBP reconstructions. The diameter was chosen as 11 pixel lengths, which is comparable to the diameter of an IF at the resolution used for this study. The surface-dependent signal at a pixel of a tilt image was modelled to be proportional to the boundary length hit by a beam whose width was chosen as one pixel length. The value of a simulated projection at a particular pixel was chosen to be proportional to the area within the circle that got projected onto the pixel. Both signals were normalized in order to obtain the same total signal strength for projections and surface rendering.

Figure 6 illustrates that the WBP reconstruction based on a surface dependent signal (Fig. 6(b)) does not differ substantially from the reconstruction obtained from projection data (Fig. 6(a)). The main difference is a slightly more faded interior of the circle in the reconstruction based on the surface signal in comparison to the one obtained from projections. In backprojections of experimental SEM tilt series, the fading in the interior of the filaments was less noticeable than for the simulated data. This is plausible since in the WBP reconstruction of an imperfectly aligned tilt series the relatively

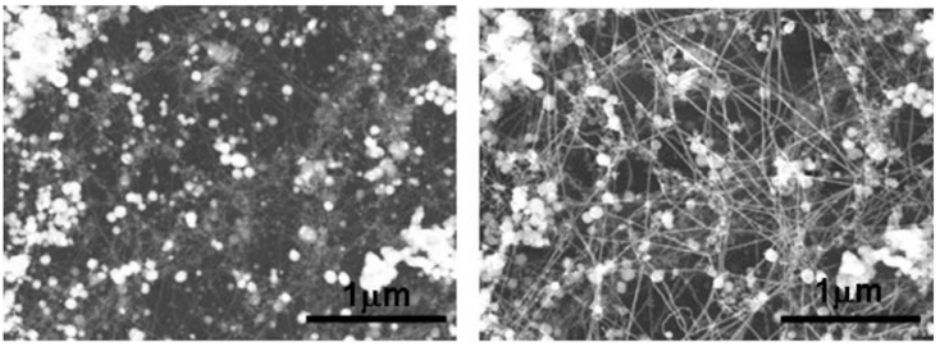

Fig. 4. STEM dark field and SEM secondary electron images taken from the same intracellular location at 0° tilt. STEM images provided a rather low signal of IFs in comparison to the strong signal of non-IF cytoplasmic leftovers after extraction of the cells. Secondary electron imaging enhanced the signal of IFs. (a) STEM dark field image at 30 kV. (b) SEM image at 30 kV.

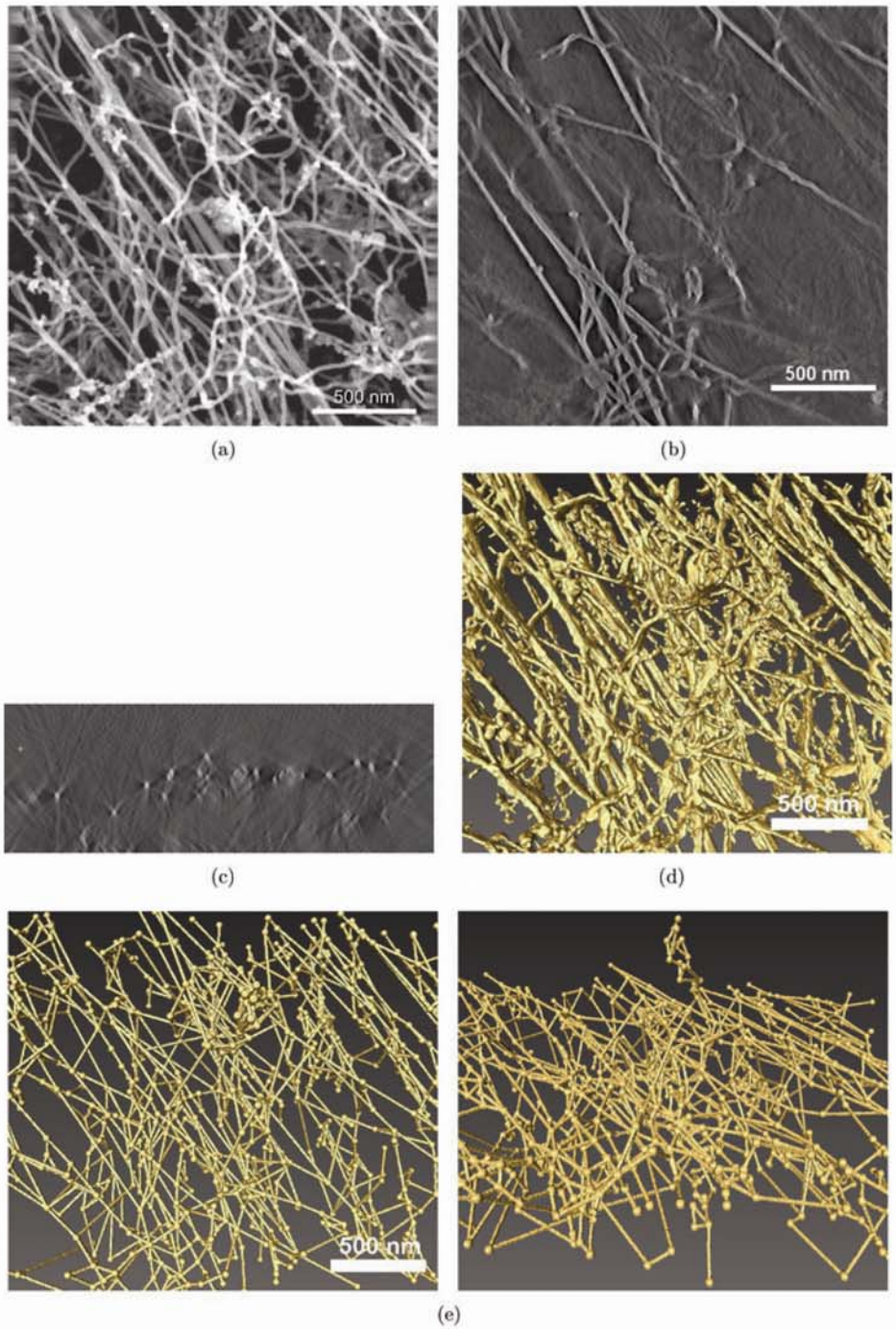

Fig. 5. IF network in a detergent-extracted Panc 1 cell visualized at a magnification of 50,000. Filaments in some depth are clearly visible at good contrast in the secondary electron tomogram. The graph extracted from the tomogram exhibits a genuinely 3D structure. (a) SEM image at 0° tilt. (b) Horizontal cut through an SEM tomogram. (c) Vertical cut through an SEM tomogram. (d) Tomogram after binarisation (top view). (e) Network graph extracted from the tomogram, top view (left), rotated by 40° around central axis (right).

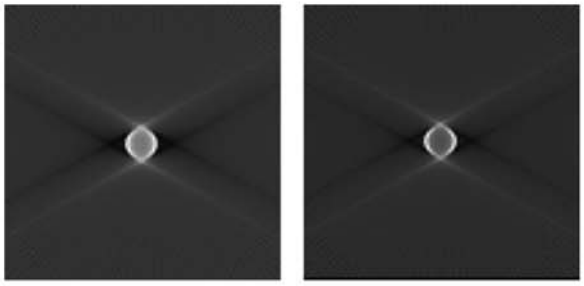

(a) (b)

Fig. 6. WBP reconstructions of a circle (diameter 11 pixel lengths) from simulated projections (corresponding to TEM) and from a simulated surface dependent signal (corresponding to the secondary electron signal of SEM). The tilt range was chosen from $-60°$ to $+60°$ at an increment of $2°$. (a) WBP from simulated TEM signal. (b) WBP from simulated secondary electron signal.

high density, which under ideal alignment is found along the boundary of the reconstructed object, is spread over a larger area. This is a consequence of the superposition of backprojections under different tilt angles in the WBP algorithm (Buzug, 2008).

In order to monitor the impact of shadowing effects, WBP reconstructions were computed from the simulated SEM tilt series of the circle where the signal was set to zero over a variety of tilt ranges. Figures 7(d), (e) and (f), illustrate the effect of shadowing for the central part of the tilt range, where the information of the central $40°$, $60°$ and $80°$ is missing, respectively. The missing information results in decreased contrast. Furthermore, the reconstruction of the circle approaches a square. Figures 7(a), (b) and (c) depict the most frequent shadowing scenario occurring for filaments in deeper network layers of our experimental data, namely shadowing at high tilt angles. In this setting, the reconstruction of the circle exhibited an oval shape at decreased contrast to the background. The loss in contrast was more extreme than observed in the experimental data, where WBPs were computed from tilt series with small imperfections in alignment. As discussed above, density was therefore more evenly spread over the filament profiles than on a WBP under ideal alignment such that contrast was increased.

Morphological network characteristics were computed for 11 tomograms, where sampling regions were chosen at random throughout the entire cytoplasm. Network densities varied between $0.0082\,\mathrm{nm}^{-1}$ and $0.0133\,\mathrm{nm}^{-1}$ with mean $0.01\,\mathrm{nm}^{-1}$ and standard deviation $0.0019\,\mathrm{nm}^{-1}$ (Fig. 8(a)). The spread between minimal and maximal network density observed was thus equivalent to 51% of the mean value of the network densities.

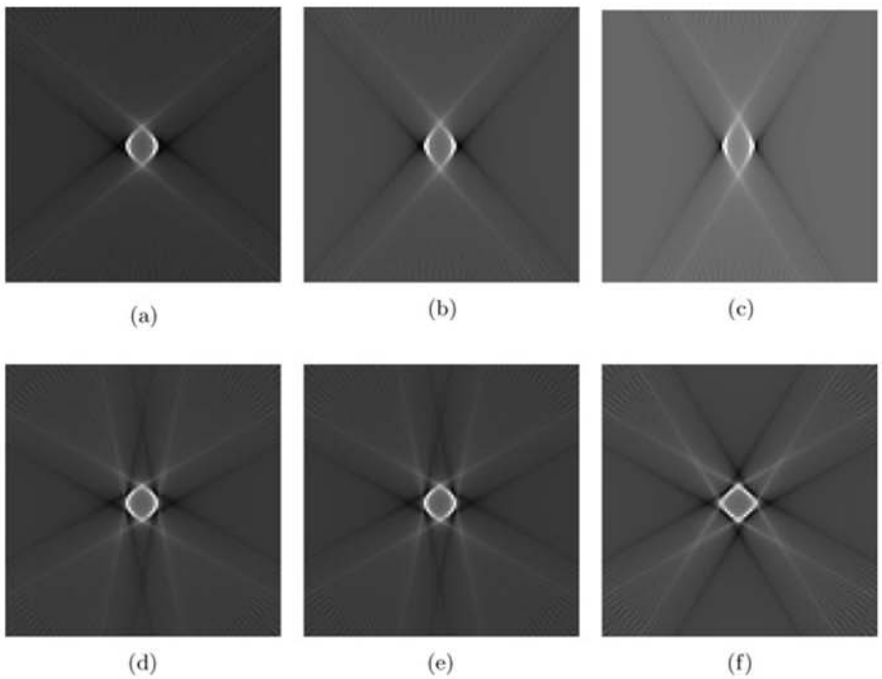

(a) (b) (c)

(d) (e) (f)

Fig. 7. WBP reconstructions of a circle (diameter 11 pixel lengths) from a simulated secondary electron signal with shadowing effects. The tilt range was chosen from $-60°$ to $+60°$ at an increment of $2°$. (a) Shadowing for tilt angles in $(-60°, -50°)$ and $(50°, 60°)$. (b) Shadowing for tilt angles in $(-60°, -40°)$ and $(40°, 60°)$. (c) Shadowing for tilt angles in $(-60°, -30°)$ and $(30°, 60°)$. (d) Shadowing for tilt angles in $(-20°, 20°)$. (e) Shadowing for tilt angles in $(-30°, 30°)$. (f) Shadowing for tilt angles in $(-40°, 40°)$.

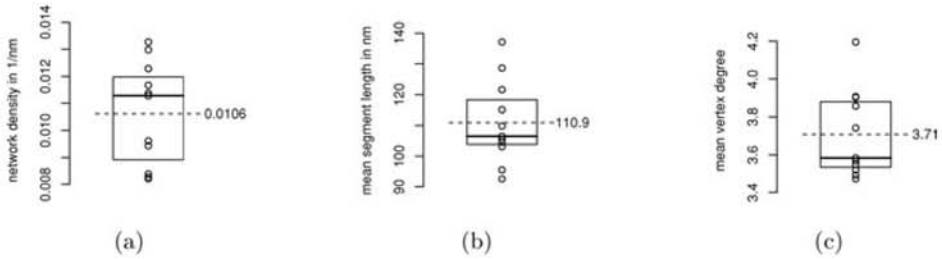

Fig. 8. Boxplots of network density, mean segment length and mean vertex degree that were computed for 11 tomograms. Bold lines depict medians, whereas dashed lines indicate the sample means, whose values can be found to the left of the boxes. (a) Network density. (b) Mean segment length. (c) Mean vertex degree.

The mean segment length in the tomograms varied between 93 nm and 137 nm, its mean and standard deviation being 111 nm and 13.6 nm, respectively. The spread between maximum and minimum mean segment length corresponds to 40% of the average mean segment length (Fig. 8(b)).

Measurements of the mean vertex degree indicated substantial variability of network connectivity. Values varied between 3.5 and 4.2 with a standard deviation of 0.23. This spread corresponds to 20% of the average mean vertex degree with respect to all tomograms, which was 3.7. Maximum connectivity was measured for tomogram 3, which exhibited increased relative frequencies of vertices of degree 4 and even higher (Fig. 9(a)). Vertex degrees above 4 were observed if several IFs were linked by microgel structures (Fig. 10). Degree distributions with pronounced increases in relative frequencies of higher vertex degrees could also be observed in tomograms 4, 10 and 11 (Fig. 9). On the other hand, tomograms with extremely low connectivity such as samples 1, 2 exhibited a high frequency of vertices of degree 3 (Fig. 9).

Since connectivity was assessed by vertex degrees it was important to monitor if the results were distorted by the merging parameter d in the segmentation algorithm, which ensures that network vertices of less than a distance d apart are replaced by a single cross-link (see 'Image segmentation' section). Figure 11 shows that the mean vertex degree depended on the merging parameter. However, ranking of the

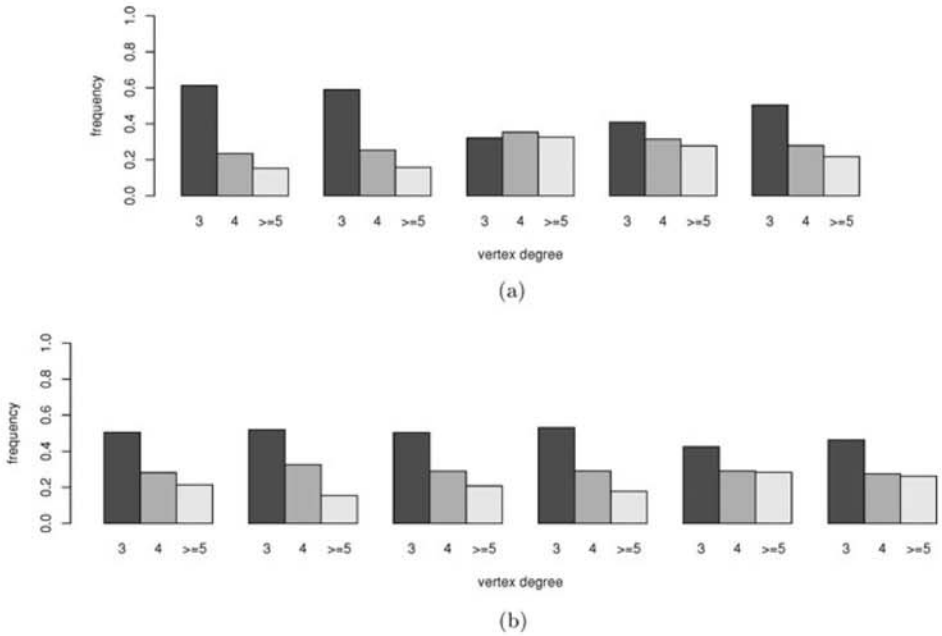

Fig. 9. Fractions of vertices with degree 3, 4 and ≥ 5 (with respect to all vertices of degree at least 3). (a) Tomograms 1–5 (from left to right). (b) Tomograms 6–11 (from left to right).

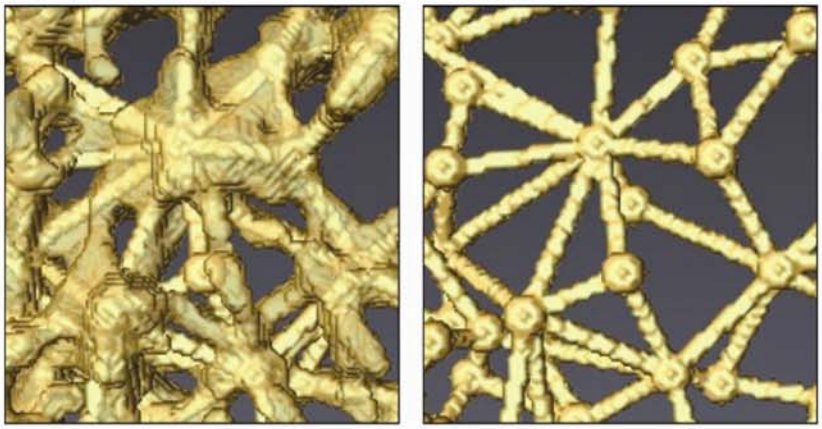

Fig. 10. Filaments connected by a microgel structure. (a) Section of a thresholded tomogram. (b) Extracted graph structure.

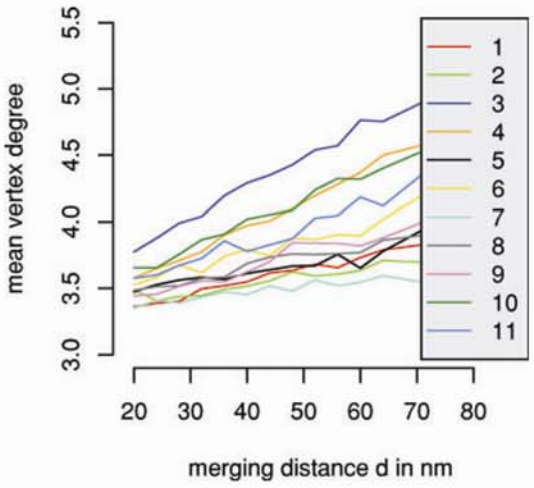

Fig. 11. Mean vertex degree as a function of the merging distance d in the segmentation algorithm.

different tomograms with respect to the mean vertex degree was rather stable. As a consequence, the test results for the rank-based correlation coefficients ρ_S and τ discussed below were hardly affected by the merging parameter. For these investigations d was not chosen smaller than 20 nm, since this would be less than the filament diameter after carbon coating and thus, shorter network segments can clearly be regarded as segmentation artefacts.

In order to assess whether changes of network density, mean segment length and connectivity exhibit interdependencies, two statistical tests were performed for each pair of characteristics. The first one tested the null hypothesis that Spearman's rank-order correlation coefficient ρ_S was equal to 0 whereas the second one tested the analogous hypothesis for Kendall's τ. In both tests, the alternative hypothesis was chosen as two-sided, i.e., any kind of correlation no matter if positive or negative leads to a rejection. As also suggested by the scatterplot in Fig. 12(a) the hypothesis that there is no significant correlation of network density and mean segment length is not rejected for Spearman's $\rho_S (P = 0.99)$ and for Kendall's $\tau (P = 1.0)$. The tests also did not reject the hypothesis of uncorrelated changes of network density and mean vertex degree (Table 1, see also Fig. 12(b)). At the level of significance $\alpha = 0.1$ variations of the merging parameter d did not change test results (all P-values were above 0.29). Thus, independently of d the correlation coefficients did not significantly differ from 0.

Tests however indicated a significant negative correlation between mean segment length and mean vertex degree (Fig. 12(c)). More precisely, the null hypothesis of correlation coefficients being equal to zero was rejected at the 10% level although not at the 5% level (Table 1). The tests for correlation of mean segment length and mean vertex degree were also applied in their one-tailed version for negative correlation, i.e., H_0 was rejected if and only if the correlation coefficient (which was either ρ_S or τ) was less than its α quantile. In that case, H_0 was even rejected at the 5% level ($p = 0.026$ and $p = 0.043$ for ρ_S and τ, respectively).

At the 10% level, significant correlation was found for all merging distances $d \geq 28$ nm. For $d = 24$, P-values increased to 0.16 for ρ_S and to 0.1 for τ. A merging distance of $d = 20$ did not exhibit significant correlation of mean segment length and mean vertex degree. Since we identified $d = 36$ nm as a reasonable merging parameter to suppress artefact formation, one can conclude that test results behaved stable for suitable choices of d.

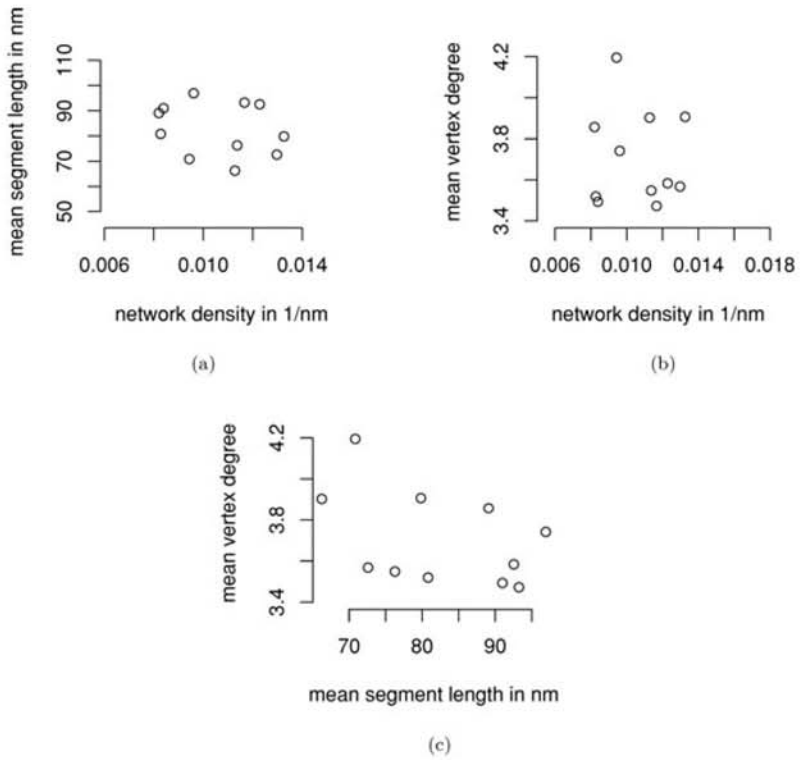

Fig. 12. Scatterplots displaying the correlation between network characteristics. (a) Network density vs. mean segment length. (b) Network density vs. mean vertex degree. (c) Mean segment length vs. mean vertex degree.

Table 1. Test results for the hypothesis of uncorrelated changes in the depicted pairs of network characteristics. The table contains p-values of tests for $H_0 : \rho_S = 0$ (upper values) and $H_0 : \tau = 0$ (lower values) against the two-sided alternative. The hypothesis of uncorrelated variation of two characteristics is rejected at a level of significance α, once the corresponding p-value does not exceed α. Hence both tests detect a significant correlation of mean segment length and mean vertex degree at the level of $\alpha = 0.1$, whereas there is no significant correlation between network density and each of the other two characteristics.

p-values	Mean segment length	Mean vertex degree
Network density	0.99 1.0	0.85 1.0
Mean segment length		0.05 0.09

Discussion

The architecture of the IF network plays a pivotal role for cell migration by regulating cell viscoelasticity (Beil *et al.*, 2003). In networks formed by semi-flexible polymers such as IF, even small alterations of network architecture can significantly change the elasticity of the network and, hence, the mechanical properties of cellular compartments (Morse, 1998; Gardel *et al.*, 2004). Numerical studies and physical models for networks in 2D can provide valuable information on the relation between 2D network morphology and the elastic shear modulus of the networks (Head *et al.*, 2003; Heussinger & Frey, 2006, 2007; Fleischer *et al.*, 2007). Nevertheless, although IF networks in the cell periphery often exhibit an almost planar structure (Beil *et al.* 2005), in less flat cellular compartments the IF cytoskeleton can clearly form a genuinely 3D biophysical network (Fig. 5(c)), which in comparison to the 2D case possesses additional degrees of freedom with respect to morphology and mechanical behaviour (Huisman *et al.*, 2007). The methodology of this study allows one to investigate IF network morphology in 3D at high resolution. This way, we were able to compute network characteristics from a tomographic data set, which for non-planar networks can only be assessed from 3D image data. These comprise connectivity and the length of network segments, which in a correlative numerical study have been identified as relevant parameters for the elasticity of semi-flexible polymer networks (Huisman *et al.*, 2007).

There exist a number of papers discussing detergent extraction for TEM replicas (e.g. Svitkina, 2007). These data sets still represent the generally accepted standard on which

the textbook models of cytoskeleton structures as e.g. in Alberts *et al.* (2008) are based. For actin networks artefact formation caused by detergent extraction, such as filament branching and visibility of the helical arrangement of G-actin subunits has been discussed in Resch *et al.* (2002) and Walther (2008). Therefore, alternative methods, such as cryo-TEM were introduced. In pioneering work by Medalia *et al.* (2002), the actin filament network in a very thin protrusion of the slime mould dictyostelium was tomographically visualized by cryo-TEM. This method is currently restricted to very thin samples; compartments of Panc 1 cells with non-planar IF networks would be too thick. In future work, we plan to combine detergent extraction with freeze drying methods (Walther, 2008) in order to reduce the danger of artefact formation. Data obtained by detergent extraction and critical point drying need to be interpreted with care. However, first experiments with freeze-dried samples do not show obvious differences with respect to network structure.

A notable phenomenon on our images is that filaments appear considerably thicker (20 to 25 nm) than described in the literature (10 to 12 nm) (Coulombe & Omary, 2002). This could be due to a number of factors. The samples are fixed with glutaraldehyde and osmium tetroxide. Parts of this fixatives could attach on to the filaments and increase the measured thickness. Carbon coating was done perpendicular to the sample, without rotation. The thickness of 5 nm was measured by a quartz crystal thickness monitor, which is a flat object. If carbon coating would be purely geometrical, the 5 nm would be added only at the top of the filaments and not influence the measured thickness, at least at 0° tilt angle. However, carbon is reflected during coating by the objects, so that it sticks to the filaments and increases the filament diameter by a not fully predictable amount. Finally, SEM imaging itself bears some error, since the electron probe is not infinitely small but has a certain diameter, and as in any kind of scanned imaging, the structure visible in the picture is a convolution of the sample and the imaging probe.

At first sight, tomogram generation based on an SEM tilt series may appear counterintuitive, since the input data is surface dependent and thus violates the projection requirement of tomographic reconstruction. Nevertheless, the contrast in STEM projections of the keratin networks in detergent-extracted cells turned out to be so low that continuity tracking of the filaments in the reconstructed tomograms was hardly possible. Since for this study detergent-extracted cells were investigated, single filaments were clearly visible at most tilt angles and could therefore be mapped by the surface-dependent secondary electron signal yielding high contrast images. Thus, the single images of the SEM tilt series could be viewed as good approximations for projection images of a modified density distribution within the observed volume. These modifications were such that filaments were highlighted and the grey level of non-IF cytoplasmic components, which had not been removed during extraction, was decreased. Shadowing effects as illustrated in Fig. 7 weakened contrast in lower levels of the tomograms and posed a certain difficulty for segmentation of the image in filamentous and background phase. This was therefore not done by a global thresholding procedure but semi-automatically by means of the Avizo software package, where thresholds were selected manually for different parts of the network that were then identified automatically based on connectivity. Imperfections of the segmentation resulting in dead ends within the network graph were additionally reduced by the extrapolation algorithm discussed in Appendix B. For the extraction of the network graph from the thresholded tomogram it was also taken into account that the missing tilt wedge and shadowing effects lead to ovally stretched filament profiles in the binarized tomograms. This was compensated for by an algorithm centring the extracted line segments within the filamentous phase (Appendix A). It should be emphasized that after semi-automatic binarization of the tomograms into filamentous phase and background, network graphs were extracted by a fully automatic algorithm. This way potential bias introduced by manual segmentation was minimized.

The thickness of the networks, investigated in this study was up to 550 nm, not taking into account single filaments protruding from the main network body. The method of SEM tomography for detergent extracted samples is not primarily limited by sample thickness but by network density. In our samples, we could detect up to three filaments on top of each other. Nevertheless, for denser networks this may not be possible if shadowing of deeper network components leads to a more limited visibility during tilting. On the other hand, in less dense networks even more layers of filaments may be reliably reconstructed in the tomograms.

Analysis of the extracted network graphs revealed a substantial morphological variability of IF networks in cultured human pancreatic cancer cells. For our analysis, we focussed on morphological network characteristics that can influence the elastic modulus of semi-flexible polymer networks (Huisman *et al.*, 2007), namely network density, mean segment length and mean vertex degree. All of these are spatial averages of morphological characteristics and can thus be assumed to possess a stable behaviour in the sense of ergodic limits. This makes them appropriate for statistical analysis at small sample sizes. Although the mean vertex degree depended on the merging parameter d of the segmentation algorithm, the latter being necessary to remove skeletonization artefacts in image segmentation, highly and weakly connected networks could clearly be distinguished independently of the choice for d (Fig. 11).

Tomograms did not only exhibit substantial variations in network density but also in their mean segment length and connectivity as measured by the mean vertex degree. Tests for correlation between these characteristics revealed that there is no significant correlation between network density and mean vertex degree as well as between network density

and mean segment length. On the other hand, tests indicated negative correlation between mean segment length and mean vertex degree. Test results were similar when connectivity was assessed by an approach based on the relative length of minimum spanning trees (MST), that has been suggested in Beil *et al.* (2009). Since relative MST length and mean vertex degree were strongly correlated these results were not included in favour of a more concise presentation. Our results suggest that the mechanically relevant structural characteristics connectivity and mean segment length cannot be viewed as a function of network density, which in our definition primarily measures the amount of filamentous protein in the network independently of network architecture. Thus, in addition to controlling the amount of IF protein forming the networks, Panc 1 cells apparently possess a second degree of freedom for adjusting network architecture in a way that influences the elastic modulus of the network. Since variations of mean segment length and connectivity do not require protein syntheses they are possibly used as energy-efficient means for fine-tuning of mechanical properties. To the best of our knowledge, there is currently no universal physical model that would allow for a computation of the elastic shear modulus of a 3D semi-flexible polymer network based on morphological measurements and the material properties of single filaments. Since results of numerical correlation studies are dependent on specific material properties and the models used to generate virtual network data, they do not allow for immediate quantitative conclusions in other settings. They can however reveal principles defining the interplay between network morphology and mechanics, and hence yield substantial indications for mechanical effects caused by morphological variability. Independently from numerical simulations, experiments can be designed in order to combine micro- and nanomechanical measurements on fixed and living cells (Atakhorrami *et al.*, 2006; Marti *et al.*, 2008) with the method of SEM tomography and image segmentation proposed in this study. This presents a promising experimental approach to correlate mechanical properties of the cells and 3D morphological characteristics of their IF network.

Acknowledgements

This work was funded by a grant from Deutsche Forschungsgemeinschaft (SFB 518 project B21). We would like to thank Michael Beil for helpful discussions and Guido Adler for constant support of the project.

References

Alberts, B., Johnson, A., Lewis, L., Raff, M., Roberts, K. & Walter, P. (2008) *Molecular Biology of the Cell*. 5th ed. Garland Publishing, New York.

Atakhorrami, M., Sulkowska, J.I., Addas, K.M., *et al.* (2006) Correlated fluctuations of microparticles in viscoelastic solutions: quantitative measurement of material properties by microrheology in the presence of optical traps. *Phys. Rev. E* **73**, 061501.

Bartesaghi, A., Sprechmann, P., Liu, J., Randall, G., Sapiro, G. & Subramaniam, S. (2008) Classification and 3D averaging with missing wedge correction in biological electron tomography. *J. Struct. Biol.* **162**, 436–450.

Beil, M., Micoulet, A., von Wichert, G., *et al.* (2003) Sphingosylphosphorycholine regulates keratin network architecture and visco-elastic properties of human cancer cells. *Nat. Cell Biol.* **5**, 803–811.

Beil, M., Braxmeier, H., Fleischer, F., Schmidt, V. & Walther, P. (2005) Quantitative analysis of keratin filament networks in scanning electron microsopy images of cancer cells. *J. Microsc.* **220**, 84–95.

Beil, M., Eckel, S., Fleischer, F., Schmidt, H., Schmidt, V. & Walther, P. (2006) Fitting of random tessellation models to cytoskeleton network data. *J. Theor. Biol.* **241**, 62–72.

Beil, M., Lück, S., Fleischer, F., Portet, S., Arendt, W. & Schmidt, V. (2009) Simulating the formation of keratin filament networks by a piecewise-deterministic Markov process. *J. Theor. Biol.* **256**, 518–532.

Buser, C., Walther, P., Mertens, T. & Michel, D. (2007) Cytomegalovirus primary envelopment occurs at large infoldings of the inner nuclear membrane. *J. Virol.* **81**, 3042–3048.

Buzug, T.M. (2008) *Computed Tomography*. Springer, Berlin.

Coulombe, P.A. & Wong, P. (2002) 'Hard' and 'soft' principles defining the structure, function and regulation of keratin intermediate filaments. *Curr. Opin. Cell Biol.* **14**, 110–122.

Fleischer, F., Ananthakrishnan, R., Eckel, S., *et al.* (2007) Actin network architecture and elasticity in lamellipodia of melanoma cells. *New J. Phys.* **9**, 420.

Fourard, C., Malandain, G., Prohaska, S. & Westerhoff, M. (2006) Blockwise processing applied to brain microvascular network study. *IEEE Trans. Med. Im.* **25**, 1319–2006.

Fuchs, E. (1994) Intermediate filaments: structure, dynamics, function and disease. *Annu. Rev. Biochem.* **63**, 345–382.

Gardel, M.L., Shin, J.H., MacKintosh, F.C., Mahadevan, L., Matsudaira, P. & Weitz, D.A. (2004) Elastic behavior of cross-linked and bundled actin networks. *Science* **304**, 1301–1305.

Head, D.A., Levine, A.J. & MacKintosh, F.C. (2003) Deformation of cross-linked semiflexible polymer networks. *Phys. Rev. Lett.* **91**, 108102.

Herrmann, H., Bär, H., Kreplak, L., Strelkov, S.V. & Aebi, U. (2007) Intermediate filaments: from cell architecture to nanomechanics. *Nat. Rev. Mol. Cell Biol.* **8**, 562–573.

Heussinger, C. & Frey, E. (2006) Stiff polymers, foams, and fiber networks. *Phys. Rev. Lett.* **96**, 017802.

Heussinger, C. & Frey, E. (2007) Role of architecture in the elastic response of semiflexible polymer and fiber networks. *Phys. Rev. E Stat. Nonlin. Soft. Matter. Phys.* **75**, 011917.

Hollander, M. & Wolfe, D.A. (1973) *Nonparametric Statistical Methods*. J. Wiley & Sons, New York.

Huisman, E.M., van Dillen, T.M., Onck, P.R. & Van der Giessen, E. (2007) Three-dimensional cross-linked F-actin networks: relation between network architecture and mechanical behavior. *Phys. Rev. Lett.* **99**, 208103.

Joy, D.C. & Pawley, J.B. (1992) High-resolution scanning electron microscopy. *Ultramicroscopy* **47**, 80–100.

Kremer, J.R., Mastronarde, D.N. & McIntosh, J.R. (1996) Computer visualization of three-dimensional image data using IMOD. *J. Struct. Biol.* **116**, 71–76.

Marti, O., Holzwarth, M. & Beil, M. (2008) Measuring the nanomechanical properties of cancer cells by digital pulsed force mode imaging. *Nanotechnology* **19**, 384015.

Mayer, J., Schmidt, V. & Schweiggert, F. (2004) A unified simulation framework for spatial stochastic models. *Simul. Model. Pract. Th.* **12**, 307–326.

Medalia, O., Weber I., Achilleas, S., Frangakis, D.N., Gerisch, G. & Baumeister, W. (2002) Macromolecular architecture in eukaryotic cells visualized by cryoelectron tomography. *Science* **298**, 1209–1213.

Midgley, P.A. & Dunin-Borkowski, R.E. (2009) Electron tomography and holography in materials science. *Nat. Mater.* **8**, 271–280.

Morse, D.C. (1998) Viscoelasticity of concentrated isotropic solutions of semiflexible polymers. 1. Model and stress tensors. *Macromolecules* **31**, 7030–7043.

Resch, G.P., Goldie, K.N., Krebs, A., Hoenger, A. & Small, J.V. (2002) Visualisation of the actin cytoskeleton by cryo-electron microscopy. *J. Cell Sci.* **115**, 1877–1882.

Ris, H. (1985) The cytoplasmic filament system in critical-point dried whole mounts and plastic embedded sections. *J. Cell Biol.* **100**, 1474–1478.

Sailer M., Lück, S., Schmidt, V., Beil, M., Adler, G. & Walther, P. (2009) Three-dimensional analysis of the intermediate filament network using SEM-tomography. *9th Multinational Conference on Microscopy*, Graz, Austria.

Sheskin, D.J. (2000) *Handbook of Parametric and Nonparametric Statistical Procedures*, 2nd ed. Chapman & Hall/CRC, New York.

Soille, P. (1999) *Morphological Image Analysis, Principles and Applications*. Springer, Berlin.

Suresh, S., Spatz, J., Mills, J.P., *et al.* (2005) Single-cell biomechanics and human disease states: gastrointestinal cancer and malaria. *Acta Biomaterial.* **1**, 15–30.

Svitkina, T.M. & Borisy, G.G. (1998) Correlative light and electron microscopy of the cytoskeleton of cultured cells. *Method. Enzymol.* **298**, 570–592.

Svitkina, T.M. & Borisy, G.G. (1999) Arp2/3 complex and actin depolymerizing factor/cofilin in dendritic organization and treadmilling of actin filament array in lamellipodia. *J. Cell Biol.* **145**, 1009–1026.

Svitkina, T. (2007) Electron microscopic analysis of the leading edge in migrating cells. *Method. Cell Biol.* **79**, 295–319.

Walther, P. (2008) High-resolution cryo-SEM allows direct identification of F-actin at the inner nuclear membrane of Xenopus oocytes by virtue of its structural features. *J. Microsc.* **232**, 379–385.

Windoffer, R., Wöll, S., Strnad, P. & Leube, R.E. (2004) Identification of novel principles of keratin filament network turnover in living cells. *Mol. Biol. Cell* **15**, 2436–2448.

Wöll, S., Windoffer, R. & Leube, R.E. (2007) p38 MAPK-dependent shaping of the keratin cytoskeleton in cultured cells. *J. Cell Biol.* **177**, 795–807.

Appendix A Algorithm for the optimization of segment positions

The algorithm discussed in this section has been designed to centre the line segments of an extracted network graph within the filamentous phase of the binarized tomograms (see 'Image segmentation' section). In the following for a voxel $k = (k_1, k_2, k_3) \in IN^3$ the third coordinate will denote height in the image stack and will be referred to as the z-coordinate, whereas k_1 and k_2 are the planar coordinates at 0° tilt. After binarization by thresholding a tomogram can be viewed as a map $T : V \to \{0, 1\}$ with bounded discrete domain $V = \{0, \ldots, N_1\} \times \{0, \ldots, N_2\} \times \{0, \ldots, N_3\}$, where the integers N_1, N_2 and $N_3 \in IN$ define the size of the volume. A voxel k such that $T(k) = 1$ will be called a filament voxel, i.e. it is part of the foreground of the binarized tomogram, whereas background voxels have the value $T(k) = 0$. In the following for a given tomogram T we will consider a 3D distance transform $d_T : V \to \mathbb{Z}$ which is defined as

$$d_T(k) = \begin{cases} \min\left\{\sqrt{\sum_{i=1}^{3}(k_i - m_i)^2} : \; T(m) = 0\right\} & \text{if } T(k) = 1, \\ -\min\left\{\sqrt{\sum_{i=1}^{3}(k_i - m_i)^2} : \; T(m) = 1\right\} & \text{if } T(k) = 0, \end{cases}$$

i.e., each filament voxel is mapped to its Euclidian distance from the background, whereas each background voxel is mapped to the negative of its distance from the foreground. The 2D analogue of this distance transform is illustrated in Fig. 13. The position of a line segment S with respect to the foreground, i.e. the filamentous phase, can now be evaluated based on its average length-weighted distance

$$D_T(S) = \frac{1}{|S|} \sum_{k \in V} |Q_k \cap S| d_T(k), \qquad \text{(A.1)}$$

where $|\cdot|$ is 1D length and

$$Q_k = \left[k_1 - \frac{1}{2}, k_1 + \frac{1}{2}\right] \times \left[k_2 - \frac{1}{2}, k_2 + \frac{1}{2}\right] \times \left[k_3 - \frac{1}{2}, k_3 + \frac{1}{2}\right]$$

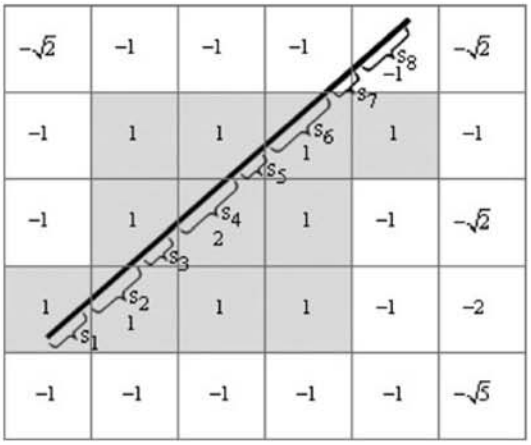

Fig. 13. Illustration of the distance transform and the computation of average length-weighted distance for the 2D case. In the setting displayed one obtains $D_T(S) = (s_1 + s_2 + s_3 + 2s_4 + s_6 - s_7 - s_8)/\sum_{j=1}^{8} s_j$, where each weight s_j corresponds to one of the intersection lengths $|Q_k \cap S|$ in (A.1).

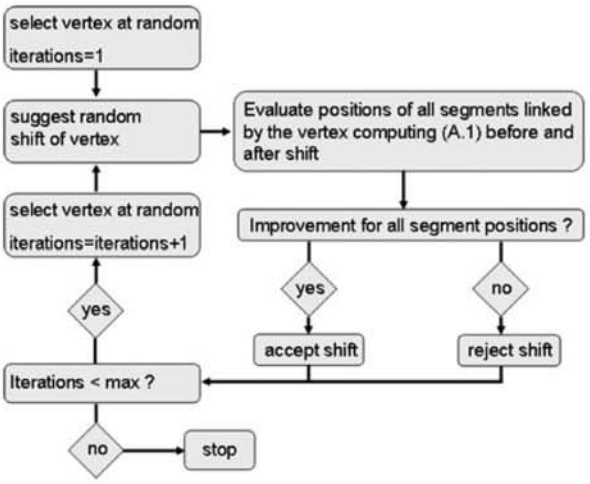

Fig. 14. Algorithm for centring the line segments in the filamentous foreground phase.

denotes the voxel k viewed as a volume element. The illustration for (A.1) in Fig. 13 shows that large values of $D_T(S)$ imply that the segment S is located rather centred within the foreground phase, whereas small values occur, once S is close to or within the background phase. Notice that $D_T(S)$ can be interpreted as a normalized line integral of the distance transform along S.

In order to optimize the position of the line segments representing the filaments, the algorithm summarized in Fig. 14 was applied. The idea of the optimization procedure is to randomly shift the positions of vertices. Such a shift is accepted as update of the network graph if the positions of the line segments connected by the vertex have improved in the sense of (A.1). If not, the shift is rejected. The algorithm consists of the following steps:

1. Define a maximum number *max* of iterations.
2. Select a network vertex at random.
3. Suggest independent and normally distributed shifts with mean 0 and standard deviation 8 nm in each of the three directions.
4. Evaluate the position of all segments linked by the vertex before and after shifting by (A.1).
5. If the position of all segments linked has improved after shifting, update the network graph by shifting the vertex to the new position.
6. If the number of iterations is less than *max*, select a new vertex and continue with step 3. With probability 0.9 the new vertex is chosen randomly among the neighbours of the current node, with probability 0.1 it is picked randomly among all vertices.

For our data on average 300 shifts were suggested for each vertex.

As discussed in the 'Image segmentation' section, a specific flaw in data quality was the inaccurate resolution of the segmented tomograms in z-direction. This resulted from the limited tilt range and a certain oversegmentation in upper network layers, which could not be avoided if threshold values were used which still allowed for identification of lower network components exhibiting decreased contrast. Thus, the segmented tomograms exhibited some filament profiles whose height exceeded their width by up to factor 3. In order to optimally centre the line segments in z-direction within the filamentous phase, the above optimization algorithm was also implemented for a modified distance map, defined by

$$\widetilde{d}_T(k) = \begin{cases} \min\{|k_3 - m_3| : \ T(m) = 0\} & \text{if } T(k) = 1, \\ -\min\{|k_3 - m_3| : \ T(m) = 1\} & \text{if } T(k) = 0. \end{cases}$$

Thus, foreground voxels are mapped to their distance from the background in z-direction and background voxels to the negative of their z-distance to the foreground. This way, certain centre voxels of z-stretched ovally profiled filaments are mapped to higher values than in case of a regular 3D-distance transform and so the random shift algorithm can be used to centre the segments within the ovale filament profiles with respect to the z-axis.

Since some filaments presumably not touching each other were stretched in z-direction in the tomograms and thus overlapping, computation of a skeleton resulted in an artificial link between these filaments. In order to remove these artefacts, the algorithm monitors all segments shorter than 60 nm which enclose an angle of no more than 45° with the z-axis. Such a segment is removed if each of the segment ends is integrated into a network vertex of T-shaped topology. This means that at least two more line segments are emanating from the vertex in a such a way that an angle of more than 90° is enclosed.

The two consecutive steps to improve filament positions based on the two different distance transforms were repeated after each step of graph modification described in the 'Image segmentation' section.

Appendix B Algorithm for the extrapolation of dead ends

Skeletons computed from binarized tomograms (Fig. 1(b)) frequently exhibit dead ends, which are well-known artefacts from skeletonization and should be removed (Soille, 1999). However, in binarized SEM tomograms of IF networks some dead ends result from errors in continuity tracking of filaments. In this case, they should be extrapolated as shown in Fig. 3 for the IF network data and illustrated in Fig. 15. In the following, we describe an algorithm constructing extrapolations of dead ends. The algorithm computes possible extrapolations and ranks them according to certain quality criteria. Following the order of this ranking, a plausibility check is performed, investigating whether the trajectory of the extrapolation was

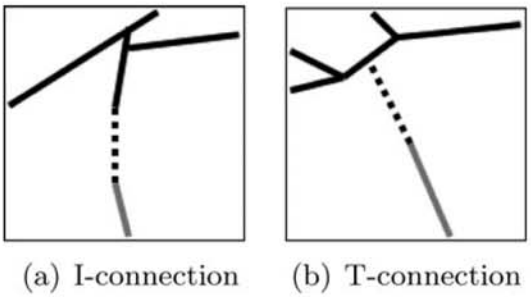

Fig. 15. Different extrapolation types. Dead ends are marked in grey, extrapolations are depicted by dotted lines.

affected by shadowing during recording of the SEM tilt series. In this case, the extrapolation can be assumed to compensate for a network component that is missing in the segmented 3D image due to its insufficient contrast in the tomogram. The dead end is extrapolated by the highest-ranked connection that passes the plausibility check. If all extrapolations are classified as implausible, the dead end is regarded as a skeletonization artefact and removed from the network graph. The details discussed in the following are summarized in Fig. 16.

Potential extrapolations considered by the algorithm can be of two different types. If the dead end is extrapolated to another dead end in the network graph, an I-connection is established (Fig. 15(a)). Alternatively, the dead end can be extrapolated to a network edge that is integrated into the network with both ends. In this case, the algorithm considers the connections to the point on the edge closest to the dead end to be extrapolated. Thus, a T-connection is formed (Fig. 15(b)).

For the potential extrapolations, their directional deviation from the orientation of the dead end and their length serve as criteria for a ranking to assess their quality. Directional deviations of more than $\pi/8$ and lengths of more than $0.4\ \mu m$ are rejected *a priori*. The remaining extrapolations are then ordered in two different ways, first by directional deviation and secondly by their length. In both cases, small values are considered as desirable. A total score for an extrapolation is now computed as the weighted mean of these two ranks, where the directional rank is weighted by 0.7 and the distance rank by 0.3. By ordering the potential extrapolations in ascending order of their score, a list is obtained where the quality of extrapolations decreases in list position.

Dead ends, which are the result of interrupted filament trajectories due to shadowing effects, often possess a dead

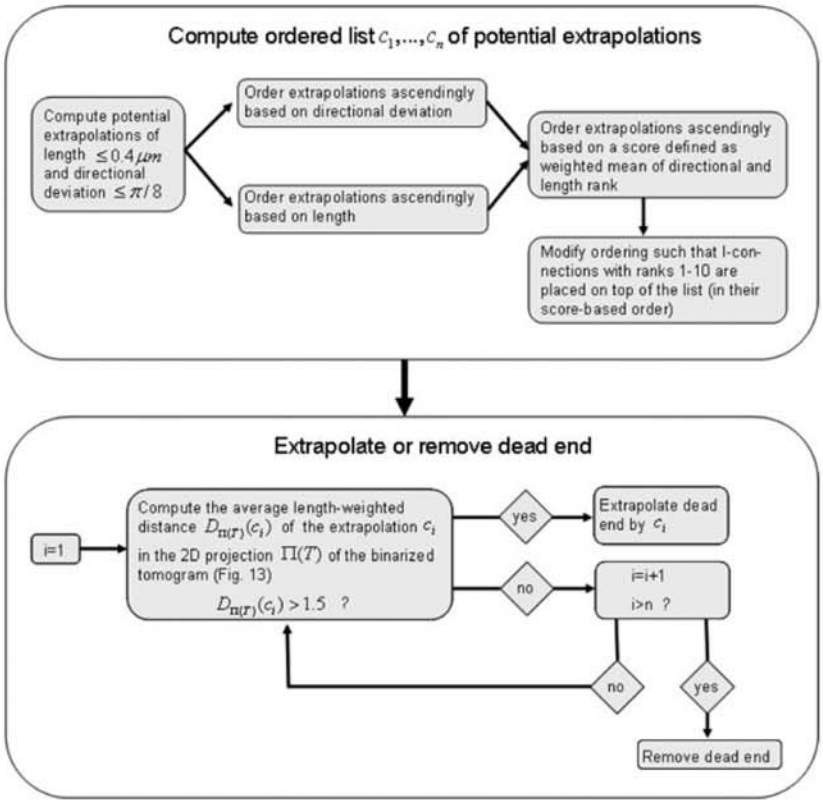

Fig. 16. Algorithm for the extrapolation or removal of dead ends.

 Journal of Microscopy

end counterpart. Thus, I-connections should be regarded as favourable. Therefore, the score-based ranking of the potential extrapolations is modified by moving the I-connections with ranks 1 to 10 to the top of the list (in the internal order of their score-based ranking).

Given the ordered list of potential links it is left to decide whether the extrapolations compensate for shadowing effects in the data or the dead end has to be considered as a skeletonization artefact. For this purpose a binarized 2D projection $\Pi(T)$ of the 3D tomogram T after thresholding is computed where a pixel (k_1, k_2) is set to 1 whenever there is some $k_3 \in \{0, \ldots, N_3\}$ such that $T((k_1, k_2, k_3)) = 1$. Otherwise, the pixel is set to 0. Filaments whose projections are covered by $\Pi(T)$ are likely to be affected from shadowing effects. In order to assess the degree of coverage of a potential extrapolation c, its average length-weighted distance $D_{\Pi(T)}(c)$ with respect to $\Pi(T)$ is computed (the principle is illustrated in Fig. 13, the formal definition is analogously to the 3D case discussed in Appendix A). Assuming that all dead ends needing extrapolation are caused by shadowing effects, an extrapolation is accepted once its normalized line integral of the 2D distance transform exceeds 1.5. The dead end is extrapolated by the connection of highest rank that is accepted by this criterion. In case none of the potential extrapolations is accepted, the dead end is considered as an artefact and removed from the network graph unless it is close to the boundary of the observation window.

Histochem Cell Biol
DOI 10.1007/s00418-010-0765-z

ORIGINAL PAPER

Preparation of cryofixed cells for improved 3D ultrastructure with scanning transmission electron tomography

Katharina Höhn · Michaela Sailer · Li Wang · Myriam Lorenz · Marion E. Schneider · Paul Walther

Accepted: 9 November 2010

Abstract Scanning transmission electron tomography offers enhanced contrast compared to regular transmission electron microscopy, and thicker samples, up to 1 µm or more, can be analyzed, since the depth of focus and inelastic scattering are not limitations. In this study, we combine this novel imaging approach with state of the art specimen preparation by using novel light transparent sapphire specimen carrier for high-pressure freezing and a freeze substitution protocol for better contrast of membranes. This combination allows for imaging membranes and other subcellular structures with unsurpassed quality. This is demonstrated with mitochondria, where the inner and outer mitochondrial membranes as well as the membranes in the cristae appear in very close apposition with a minimal intermembrane space. These findings correspond well with old observations using freeze fracturing. In 880-nm thick sections of hemophagocytes, the three-dimensional structure of membrane sheets could be observed in the virtual sections of the tomogram. Microtubules, actin and intermediate filaments could be visualized within one sample. Intermediate filaments, however, could even be better observed in 3D using surface scanning electron tomography.

Keywords STEM tomography · High-pressure freezing · Membrane · Cytoskeleton · Mitochondrium · Autophagosome · Autophagy

Introduction

Transmission electron microscopical (TEM) tomography is a method of acquiring three-dimensional data of biological samples at a nanometer scale of resolution (reviewed by Baumeister 2004). Thereby, a small sample is tilted gradually in the TEM and images are recorded at different tilt angles. This procedure results in an image series, which can be back projected into a three-dimensional model (Hoppe et al. 1974).

In this paper, we improve sample preparation for scanning transmission electron microscopical tomography (STEM tomography). STEM is a type of transmission electron microscopy where no projective lenses are used for image formation, but the sample is scanned by a very fine focused electron beam (similar to surface scanning electron microscopy). The scattered electrons are recorded with a detector and an image is formed on a monitor by integrating the signal over time. In life science, STEM has been used for mass determination of biomacromolecules (e.g., Engel et al. 1976; Müller and Engel 2001) and for X-ray microanalysis (e.g., Zierold and Steinbrecht 1987). The potential of using STEM for tomography has been pioneered by Midgley et al. (2001) for material sciences. STEM tomography has been introduced to the life sciences by Yakushevska et al. (2007). They showed that with STEM tomography, contrast and signal-to-noise ratio of

Electronic supplementary material The online version of this article (doi:10.1007/s00418-010-0765-z) contains supplementary material, which is available to authorized users.

K. Höhn · M. Sailer · L. Wang · P. Walther (✉)
Electron Microscopy Facility, Ulm University,
Ulm, Germany
e-mail: paul.walther@uni-ulm.de

L. Wang
Institute of Virology, University Hospital Ulm,
Ulm, Germany

M. Lorenz · M. E. Schneider
Section of Experimental Anesthesiology,
University Hospital Ulm, Ulm, Germany

Published online: 27 November 2010

plastic-embedded biological samples were considerably better compared to conventional bright-field TEM tomography, when using the same electron dose. STEM tomography is especially well suited for thick samples up to 1 µm (Aoyama et al. 2008) for several reasons. One such reason is the possibility of using dynamic focus, preventing the peripheral areas of a section from being out of focus at high tilt angles. The more important reason, however, is chromatic aberration due to inelastically scattered electrons, which is a limitation in TEM, but not in STEM. Aoyama et al. (2008; Fig. 5) showed an electron energy loss spectrum of a 300-keV beam passing through a 1-µm thick section at 0° and at 70° tilt. At 70° tilt (when the path of the electrons through the sample is about 3 µm), almost all electrons experienced inelastic scattering events leading to energy loss and to chromatic aberration and poor image quality in the TEM mode. In the STEM imaging mode, however, the scattered electrons will not form an image, but eventually hit the detector. Since these electrons are not focused by lenses after having lost energy, chromatic aberration is not an issue and inelastically scattered electrons may also contribute to image formation. Hohmann-Marriott et al. (2009) experimentally demonstrated that STEM is superior to TEM and EFTEM for tomography of 1-µm thick samples. They also pointed out the advantage of using axial (bright field) STEM tomography. Biskupek et al. (2010) introduced "parallel beam STEM tomography". By aligning the three-condenser system of an FEI Titan (FEI, Eindhoven, The Netherlands) such that the semi convergence angle became as small as 0.6 mrad compared to 10 mrad in regular STEM mode, the depth of focus was increased by a factor of 17. It turned out that this parallel beam mode greatly facilitates tomogram collection, since even at low magnification the sample is never out of focus and the tedious dynamic focus mode is no longer required.

Even the best microscopical imaging method, however, can only image structures that are retained during specimen preparation. For this study, we optimized high-pressure freezing, freeze substitution, plastic embedding and thin sectioning, a preparation protocol that can be applied to many different biological systems (reviewed by McDonald 2007). Some recent improvements of the method include the release of new high-pressure freezing machines (HPF Compact 01, Engineering Office M. Wohlwend GmbH, Sennwald, Switzerland; EM PACT, and EM HPM 100, Leica, Vienna, Austria), use of sapphire discs without aluminum cover for faster handling of the specimen before freezing, improvement of high-pressure freezing quality (Hawes et al. 2007) and stronger membrane contrast by adding water to the substitution medium (Walther and Ziegler 2002; Buser and Walther 2008).

The aim of this study was to record three-dimensional subcellular structures in a life-like situation using the better contrast and the possibility to work with thicker sections provided by STEM tomography. This shall be achieved by high-pressure freezing of the samples in a physiologically defined state, thereby minimizing the risk of artifact formation before freezing and of preparation-dependent artifacts. The contrast in the samples shall be improved by novel freeze substitution protocols to enhance heavy metal staining in membranes and in cytoskeletal elements. Using different kinds of STEM and SEM tomography, high-quality data sets shall be recorded from samples as thick as 1 µm.

Materials and methods

Sapphire discs

Two different types of sapphire discs (Engineering Office M. Wohlwend GmbH, Sennwald, Switzerland) were used as support for the different types of cells in culture. The standard discs (for *protocol A*) had a thickness of 0.05 mm and the new discs (for *protocol B*) had a thickness of 0.17 mm, so that they could also serve as coverslips for standard light microscopes in correlative microscopy. The sapphire discs were cleaned by sonication for 15 min each in 60% sulfuric acid, soap water and twice in absolute ethanol, and allowed to dry. The discs were then coated with approximately 20 nm carbon by electron beam evaporation and dried for 8 h or overnight in an oven at 120°C to increase the stability of the carbon film. The coated sapphire discs were then carefully immersed in complete medium and the cells were seeded on top.

Cell cultures

Monocyte-derived macrophages (Fig. 1) were differentiated from monocytes as previously described (Frascaroli et al. 2009). Monocytes were isolated from PBMC by negative selection with magnetic microbeads (Monocyte Isolation Kit II; Miltenyi Biotec, Bergisch Gladbach, Germany). One day before high-pressure freezing, the macrophages were seeded on the thin sapphire discs (1.5×10^5 cells/well).

Hemophagocytes (Fig. 2) were specifically enriched by adherent cell cultures from patients suffering from hemophagocytic lymphohistiocytosis (Schneider et al. 2002, Blood) as well as other hyperinflammatory diseases. After cell culture, the floating cells were plated onto sapphire discs and were high-pressure frozen.

Panc 1 (Figs. 3, 4) human pancreatic cancer cells (American Type Culture Collection, Manassas, VA, USA) were seeded (8×10^4 cells/ml) on carbon-coated, glow-discharged sapphire discs (thickness 170 µm) and cultivated in DMEM with 10% (v/v) FCS, 100 U/ml penicillin and

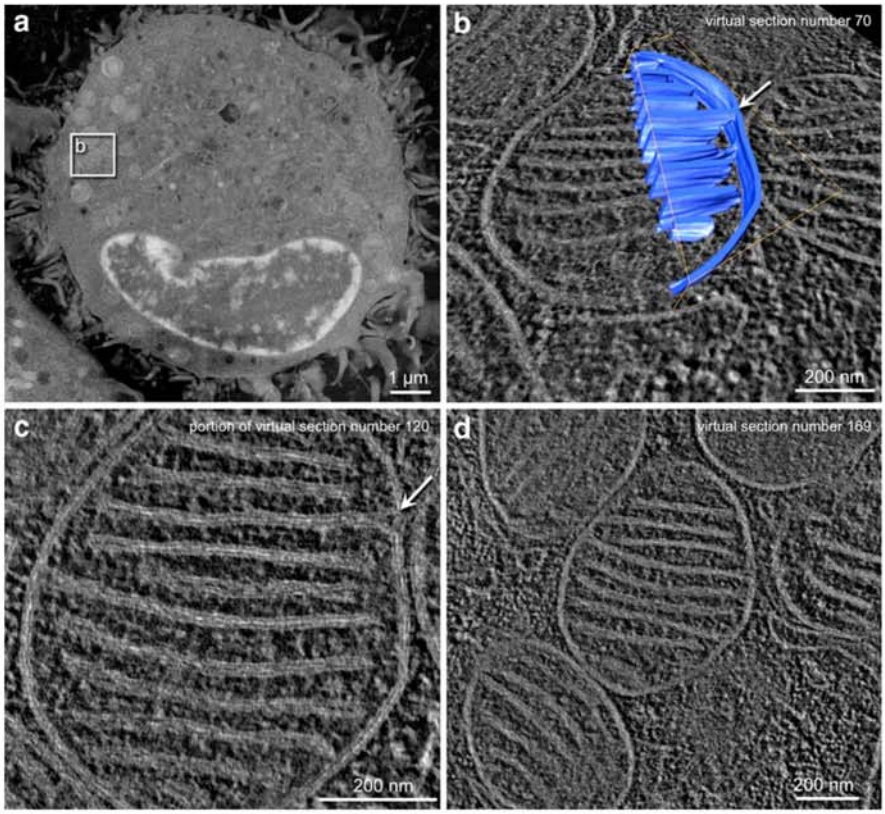

Fig. 1 Macrophage. **a** An overview image of a macrophage, prepared following protocol A. The section thickness is about 375 nm as measured with the microscope. The tilt series for the tomogram (**b**, **c**, **d**) were recorded using convergent beam STEM and show a mitochondrion; part of this was manually segmented (**b** in *blue*). **c**, **d** Computed sections with a virtual thickness of 2 nm (one voxel). In the mitochondrial membranes, the two leaflets of the bilayer are well visible. Inner and outer membranes and the membranes of the cristae are in close apposition to each other. The sheet-like cristae are in touch with the inner mitochondrial membrane only at a few points (*white arrows*). In most areas, the membrane bends at the end of the cristae, leaving a gap between the cristae and the inner mitochondrial membrane

100 mg/ml streptomycin in a humidified atmosphere containing 5% CO_2 at 37°C. Confluent cell monolayers were achieved after 2 days.

High-pressure freezing and freeze substitution

The cells on sapphire discs were frozen using a Wohlwend HPF Compact 01 high-pressure freezer (Engineering Office M. Wohlwend GmbH, Sennwald, Switzerland).

The samples were high-pressure frozen according to two different protocols.

For *protocol A*, 50-µm thick sapphire discs with the cells grown on them were clamped in between two aluminum planchettes so that the cells were protected in a 100-µm cavity on one planchette as described earlier (Buser and Walther 2008). The cavities were filled with hexadecene as introduced by Studer et al. (1989).

For *protocol B*, a 50-µm gold spacer ring (diameter 3.05 mm, central bore 2 mm; Plano GmbH, Wetzlar, Germany) was mounted in between two 170-µm thick sapphire discs with the cells grown on them, similar to the protocol introduced by Hawes et al. (2007). These sandwiches were high-pressure frozen without aluminum planchettes and without the use of hexadecene.

Freeze substitution was performed as described in Walther and Ziegler (2002) with a substitution medium consisting of acetone with 0.2% osmium tetroxide, 0.1% uranyl acetate and 5% of water for good contrast of the membranes. During 17 h, the temperature was exponentially raised from −90°C to 0°C. After substitution, the samples were kept at room temperature for 1 h and then washed twice with acetone. After stepwise embedding of the samples in epon (polymerization at 60°C within 72 h), they were cut with a microtome (Leica Ultracut UCT ultramicrotome) using a diamond knife (Diatome, Biel, Switzerland) to semi-thin sections with a nominal thickness of 500 nm or 1 µm, as measured from the readout of the microtome.

The sections were collected on bare copper grids with parallel grid bars in one direction only, to prevent the grid bars from hiding the biological structures at high tilt angles (grids for tomography, diameter 3.05 mm, 300 bars per inch, Plano GmbH, Wetzlar, Germany). For tomography, it is essential that the sections are mounted as flat as possible. It turned out to be rather difficult to attach the relatively thick sections on the grid bars. Therefore, the copper grids were coated with poly-L-lysine (10% in water) before the sections were attached. The grids were then warmed on a

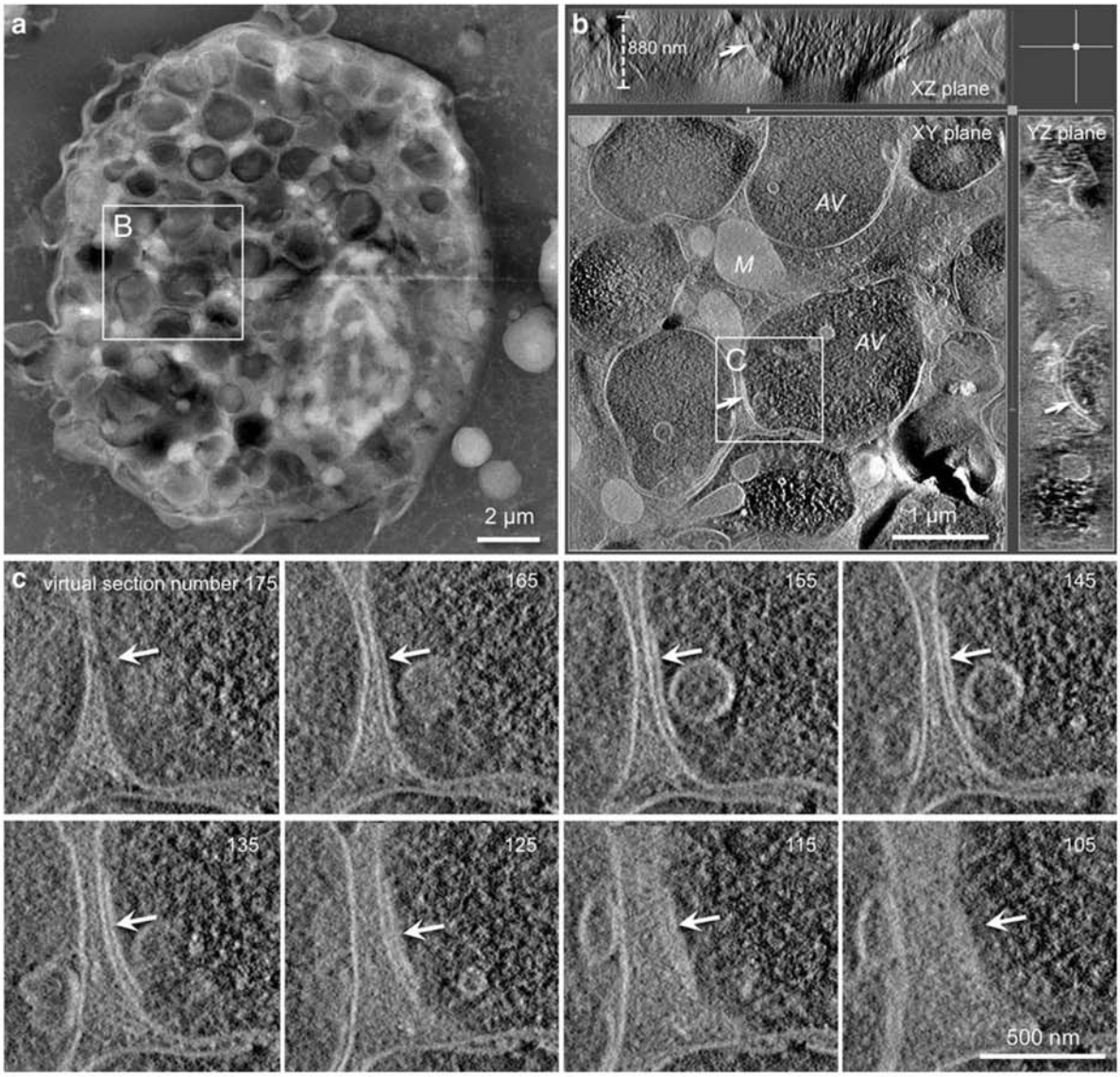

Fig. 2 **a** Whole hemophagocyte. **b** Tomogram showing autophagic vacuoles (AV) and mitochondria (M). The thickness of the section, measured with the microscope, is 880 nm as can be seen in the XZ plane. The arrows depict an isolated membrane sheet that is visible in all three planes. **c** Several virtual sections of a portion of the tomogram showing appearance (165–125) and disappearance (175 and 105) of the isolated membrane sheet. The resolution of structural details, e.g., the membrane bilayers, is slightly decreased when compared with Fig. 1

heating table to a temperature of 60°C to flatten the sections. Afterward, the sections were again coated with poly-L-lysine to attach the 15-nm colloidal gold particles (Aurion, The Netherlands) on both sample sides. These gold particles served as fiducial markers for the calculation of the tomograms. Finally, the mounted sections were carefully coated with 5-nm carbon from both sides by electron beam evaporation to increase electrical conductivity and mechanical stability. Improving electrical conductivity helps to reduce mass loss caused by ionization due to inelastic scattering (Walther et al. 1995). Also, drift is reduced when electrical conductivity is enhanced by carbon coating. Before imaging, the samples were plasma cleaned for 10 s.

STEM tomography

The tilt series (−72° to +72°; 2° increment) were recorded with a 300-kV field emission STEM (Titan 80–300 TEM, FEI, Eindhoven) using an annular dark-field detector

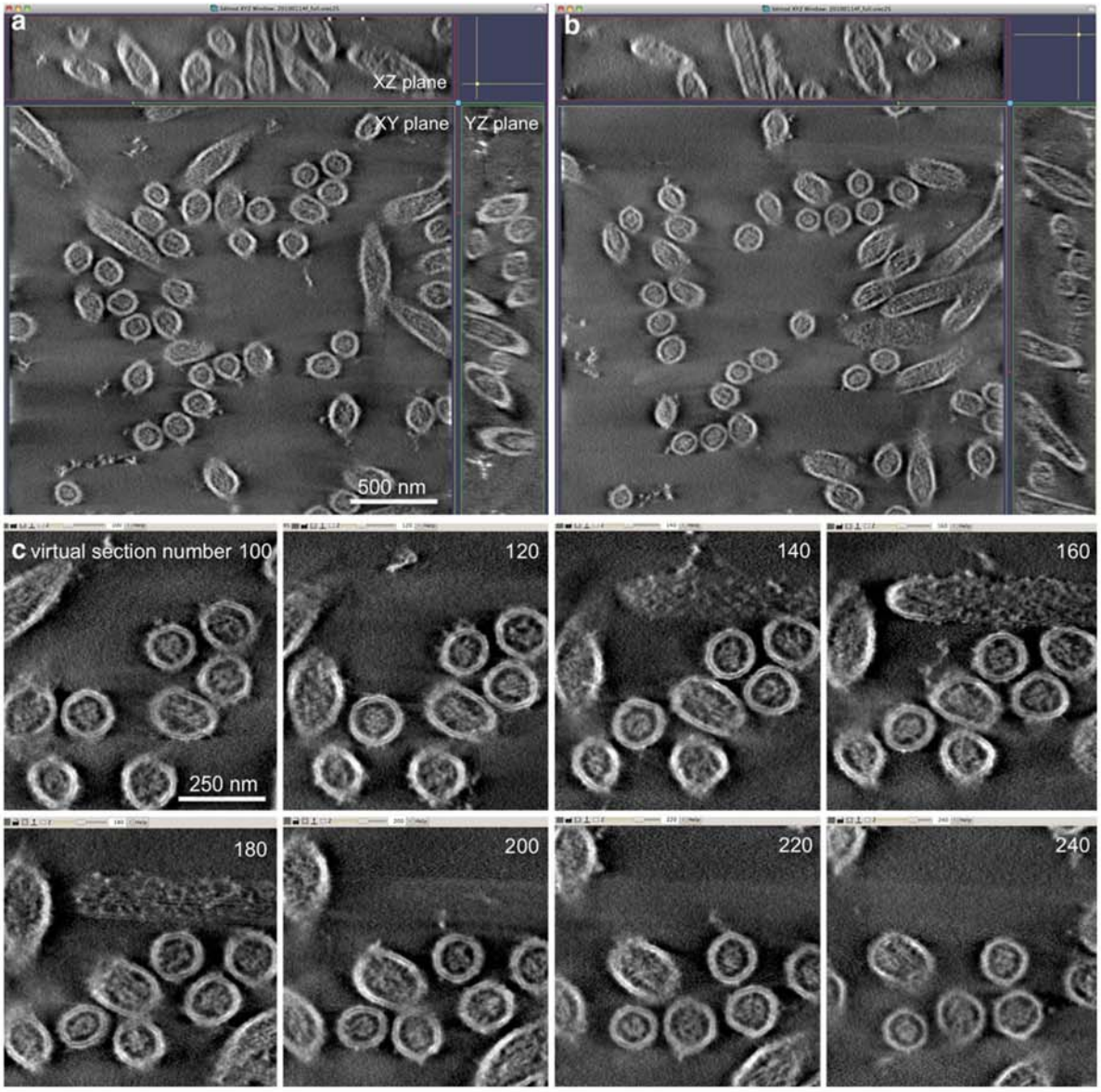

Fig. 3 Tomogram of a Panc 1 cell's microvilli prepared by protocol B and recorded using parallel beam STEM. The bilayer structure of the membranes is well resolved in all areas of the 435-nm thick section (measured with the electron microscope) and visible as two parallel *white lines*. Besides the membrane, the internal structure of the microvilli, consisting of actin and actin-related proteins, is also well preserved. The actin bundles keep a constant distance (about 20 nm) from the membrane. It is difficult to clearly resolve the thin (about 7 nm) actin filaments, which seem to be hidden by the actin-related proteins. A glimpse of individual filaments can be seen in the cross-sectioned microvillus in virtual section number 180

(Fischione, Export, PA, USA) with a camera length of 301 mm. Illumination time per 1,024 × 1,024 pixel image was 18 s. So, a total of 73 images per tomogram were recorded. The tomograms were either recorded in "convergent beam mode" (Fig. 1) with a semi-convergence angle of 10 mrad, or in "parallel beam mode" with a very small semi-convergence angle of 0.58 mrad (Figs. 2, 3 and 4 a–d) as outlined in Biskupek et al. (2010).

Tomograms were reconstructed by weighted back projection (WBP) or by simultaneous iterative reconstruction technique (SIRT) with 25 iterations using the standard settings of the IMOD software package (Kremer et al. 1996)

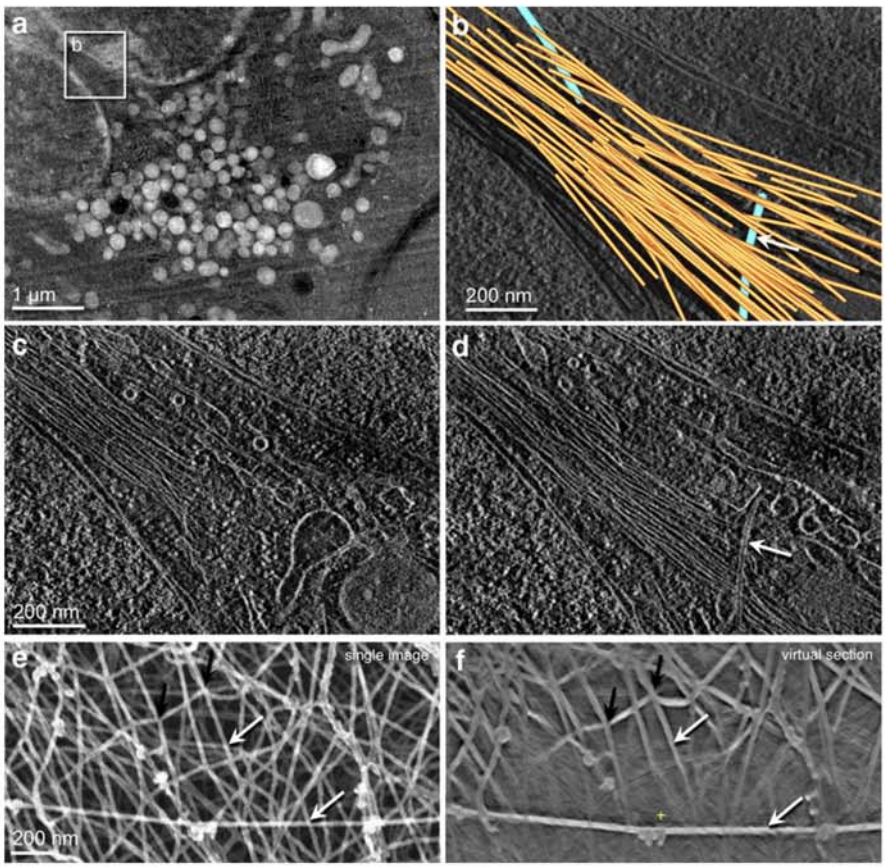

Fig. 4 Intermediate filaments in Panc 1 cells. **a**–**d** Tomogram of a portion of a Panc 1 cell, prepared according to protocol B and recorded with parallel beam STEM. The tomogram shows an area of the cytoplasm bounded on two sides by a kidney-shaped nucleus. In the cytoplasm, a bundle of densely packed filaments is visible that most likely represent intermediate filaments. The three-dimensional arrangement of these filaments and two crossing microtubules were visualized by manual segmentation (Fig. 2b, not all filaments were segmented). Using SEM tomography (**e**, **f**), filaments are imaged with higher contrast and, in a virtual section (**f**), it can be clearly decided whether the filaments cross at different planes (*white arrows*) or touch each other (*black arrows*)

version 4.1.2. For segmentation and data display, the AMIRA (Fig. 1b) and the IMOD (Fig. 4b) software were used.

Extraction preparation for SEM tomography

For comparison, intermediate filaments of Panc 1 cells were also prepared by a detergent extraction protocol (Sailer et al. 2010), using 1% of Triton X-100 so that basically all structures except intermediate filaments were removed, and afterward critical point dried and carbon coated. These samples were then imaged in a Hitachi S-5200 (Hitachi, Tokyo, Japan) scanning electron microscope (SEM) at an accelerating voltage of 5 kV using the secondary electron signal for SEM tomography at tilt angles from −60° to +60° at an increment of 2° (Fig. 4e, f), as described by Sailer et al. (2010).

Results

Using a scanned electron beam for microscopy instead of regular TEM requested adaptation of the preparation protocol in order to minimize sample damage. From earlier STEM studies, as well as from high-resolution surface SEM studies, it is known that damage can be threefold: one effect is the charge-up caused by the scanned beam. We reduced charge-up by coating the sections with 5-nm carbon from both sides, making the surface electrically conductive. Another effect is mass loss due to beam-induced ionization processes (also referred to as "etching", Müller and Engel (2001). This effect was also reduced by the carbon coating (Walther et al. 1995). On the other hand, mass can build up on the scanned area due to hydrocarbon molecules migrating over the sample surface. These are ionized and bound to the surface by the scanned beam (a process that is usually referred to as "contamination"; Müller and Engel 2001). The amount of contamination was tremendously reduced by short plasma cleaning, thereby removing hydrocarbon molecules from the sample surface immediately before microscopy, as explained in "Materials and methods".

First, we wanted to inspect the conservation and visualization of membranous structures. We therefore inspected a macrophage attached on thin sapphire discs. It was high-pressure frozen and freeze substituted according to *protocol*

A on thin sapphire discs in between two aluminum planchettes using hexadecane to fill the extracellular cavities (Fig. 1). The tilt series were recorded using convergent beam tomography. The nominal section thickness (readout at the ultramicrotome) was 500 nm. The value measured by the electron microscope, however, was about 375 nm. Figure 1a is an overview showing good overall structural preservation and visibility of ultrastructural details. Figure 2b–d shows computed sections from a tomogram with a virtual thickness of 2 nm (one voxel). For best contrast, the tomogram was reconstructed by weighted back projection (WBP) and simultaneous iterative reconstruction technique (SIRT) using the IMOD software (Kremer et al. 1996) and both virtual sections were overlaid as explained in "Materials and methods". In the mitochondrial membranes, the two leaflets of the bilayer were well discernable. The thickness of the intermembrane space including both membranes was <20 nm. The membranes of the cristae were also in close contact with each other. The sheet-like cristae were connected to the inner mitochondrial membrane only at a few points (white arrows). This is visible in the manual segmentation (Fig. 1b, in blue) as well as in the original data (Fig. 1c, white arrow). In most areas, the membrane bent at the end of the cristae, leaving a gap between the cristae and the inner mitochondrial membrane (video in supplementary material).

To investigate the potential of parallel beam STEM, we prepared a hemophagocyte by the standard freezing *protocol A* (Fig. 2). The sections were cut with 1,000 nm readout at the microtome and the thickness measured in the microscope was 880 nm. The hemophagocyte contains many autophagic vacuoles (*AV*). In addition, mitochondria (*M*) can be identified (Fig. 4a, b). An isolated piece of a membrane lies in parallel to the vacuole's membrane (arrows, Fig. 4b) and is visible in all three virtual section planes (XY, XZ and ZY). Figure 4c shows series of virtual sections with a thickness of 4 nm. The distance from one pictured section to the next is 40 nm. The membrane sheet is limited to the inner part of the thick section, since it cannot be seen in the outermost virtual sections 175 and 105. This sample demonstrates that tomography of sections as thick as 880 nm is still possible. The resolution, however, slightly decreases, so that the two leaflets of the membrane bilayer can no longer be resolved in contrast to the thinner sections in Figs. 1 and 3.

Finally, we wanted to check the potential of STEM tomography to visualize the cytoskeletal elements. For this purpose, Panc 1 cells were prepared by *protocol B* (Figs. 3, 4). In general, the freezing quality of cultivated cells frozen with this new approach that does not require hexadecane appears to be as good as with the standard *protocol A*. The tilt series were recorded using parallel beam STEM. Figure 3 shows microvilli of a Panc 1 cell. The tomogram was recorded using parallel STEM and reveals good structural preservation of membranes and cytoskeletal elements. The bilayer structure of the membranes is well resolved in all areas of the 435-nm thick section (measured in the electron microscope). Besides the membrane, the internal structure of the microvilli, consisting of actin bundles and actin related proteins, is also well preserved.

The tomogram of Fig. 4 shows an area of the cytoplasm bounded on two sides by a kidney-shaped nucleus. In the cytoplasm, a boundle of densely packed filaments is present, most likely representing intermediate filaments. The three-dimensional arrangement of these filaments and two crossing microtubules has been visualized by manual segmentation in Fig. 4b. Not all filaments were segmented, since the filaments were extremely densely packed. Figure 4e is an image and Fig. 4f is a virtual section from an SEM tomogram recorded using secondary electrons. This sample was detergent extracted. The individual filaments were imaged with very high contrast, allowing to clearly discern the virtual section between real crosslinks (black arrows) and filaments just passing each other at a short distance (white arrows).

Discussion

In previous studies, it has been implied that STEM tomography was a powerful alternative to TEM tomography in life science (Yakushevska et al. 2007; Aoyama et al. 2008; Hohmann-Marriott et al. 2009). In the present study, we combined this novel approach with the best protocols for high-pressure freezing and freeze substitution. For enhancing contrast by increased heavy metal staining, it was helpful to leave the samples in the freeze substitution medium at room temperature for an additional hour. In addtition, we optimized the samples for STEM imaging by carbon coating and plasma cleaning. This allowed us to image membranes and other macromolecular structures with high contrast in thick sections.

We found inner and outer mitochondrial membranes in close apposition with a very small intermembrane space (Fig. 1). This structure is different from the generally accepted model with a wide intermembrane space (Sun et al. 2007; Rabl et al. 2009), but in agreement with old cryofixation and freeze fracturing studies of mitochondria (Lang and Bronk 1978; Knoll and Brdiczka 1983), where it is stated that the membranes in "energized" mitochondria are in close apposition, whereas they separate when the mitochondria are "de-energized". It also fits well with our earlier studies using freeze substitution (Walther and Ziegler 2002) as well as using high-pressure freezing and freeze fracturing (Walther et al. 2009). We therefore assume that the tomogram represents the situation in a

healthy, energized mitochondrion, whereas the intermembrane space is enlarged when the mitochondria are de-energized, e.g., due to inappropriate treatment of the cells during chemical fixation or prior to freezing. The cristae we observed in macrophages were of the lamellar type (reviewed by Zick et al. 2009). They were connected to the inner mitochondrial membrane only at a few points (video in supplementary material). This fits with the "cristae junction model" originally proposed by Daems and Wisse (1966) and confirmed in several newer studies based on electron tomography (Rabl et al. 2009; Zick et al. 2009; van Driel et al. 2009; Perkins et al. 2010; Péranzi et al. 2010).

In a very thick section of a hemophagocyte (Fig. 2), it was still possible to unambiguously track an isolated membrane fragment (arrows). It is supposed that those membrane fragments occur in the context of autophagy (Liou et al. 1997). The elaborate membrane structures of newly formed phagophores and autophagic vesicles have been recently reviewed by Hsieh et al. (2009). TEM is an important qualitative approach to monitor autophagy. It obviously needs to be supported by additional techniques to unambiguously quantify autophagic flux (Barth et al. 2010).

The samples frozen in between two sapphire discs without aluminum planchettes and without using hexadecene (*protocol B*) showed the same freezing quality as samples frozen with the standard *protocol A*. The new *protocol B* bears the potential for new correlative light and electron microscopical approaches that need to be explored in future studies. In Fig. 3, the actin distribution in microvilli indicates good freezing with minimal ice crystal formation, since the actin bundles keep a constant distance (about 20 nm) from the membrane. According to the textbook (Alberts et al. 2008, Fig. 16–50), this is caused by bridging formed by actin-related proteins such as myosin I or calmodulin that connects the actin filaments to the membrane. In samples with ice crystal damage, the actin distribution in the microvilli is uneven and no space between membrane and the filaments is visible (data not shown).

Even better visibility of intermediate filaments can be achieved by secondary electron SEM tomography (Sailer et al. 2010). The electrons used for contrast formation in transmission imaging are scattered approximately in function of the mass density, which is low in thin filaments. The secondary electron signal, however, is a function of the surface area exposed to the electron beam (Seiler 1967), which is high because the surface of the filament is large compared to the volume (Fig. 4e). Using this method, we could clearly discern between filaments crossing at near distance and real crosslinks (Fig. 4e, f). For this approach, the filaments need to be exposed to the surface and extraction protocols that are not yet fully tested for artifact formation need to be used.

Hohmann-Marriott et al. (2009) pointed out the advantage of using axial (bright field) STEM tomography. For technical reasons, we were not able to implement this improved approach to our microscope and had to use dark-field imaging for this study. Nevertheless, tomography using a scanned electron beam as probe still bears a large potential for novel signal collection and specimen preparation methods.

Acknowledgments We thank Johannes Biskupek for help with the Titan electron microscope and especially for the parallel beam alignment, Eberhard Schmid for excellent technical support and for developing the important procedure of properly mounting the thick sections on the special copper grids, and Ganesh V. Pusapati for help with the cell cultures. This work was supported by the *DFG Sonderforschungsbereich 518, project A15* and *B21*, by the *DFG Einzelantrag WA 1458/3-1* and by The Histiocytosis Association of America.

References

Alberts B, Johnson A, Lewis L, Raff M, Roberts K, Walter P (2008) Molecular biology of the cell, 5th edn. Garland Publishing, New York

Aoyama K, Takagi T, Hirase A, Miyazawa A (2008) STEM tomography for thick biological specimens. Ultramicroscopy 109:70–80

Barth S, Glick D, Macleod KF (2010) Autophagy: assays and artifacts. J Pathol 221:117–124

Baumeister W (2004) Mapping molecular landscapes inside cells. Biol Chem 385:865–872

Biskupek J, Leschner J, Walther P, Kaiser U (2010) Optimization of STEM tomography acquisition–a comparison of convergent beam and parallel beam STEM tomography. Ultramicroscopy 110:1231–1237

Buser C, Walther P (2008) Freeze-substitution: the addition of water to polar solvents enhances the retention of structure and acts at temperatures around 60°C. J Mircrosc 230:268–277

Daems WT, Wisse E (1966) Shape and attachment of the cristae mitochondriales in mouse hepatic cell mitochondria. J Ultrastruct Res 16:123–140

Engel A, Dubochet J, Kellenberger E (1976) Some progress in the use of a scanning transmission electron microscope for the observation of biomacromolecules. J Ultrastruct Res 57:322–330

Frascaroli G, Varani S, Blankenhorn N, Pretsch R, Bacher M, Leng L, Bucala R, Landini MP, Mertens T (2009) Human cytomegalovirus paralyzes macrophage motility through down-regulation of chemokine receptors, reorganization of the cytoskeleton, and release of macrophage migration inhibitory factor. J Immunol 182:477–488

Hawes P, Netherton CL, Mueller M, Wileman T, Monaghan P (2007) Rapid freeze-substitution preserves membranes in high-pressure frozen tissue culture cells. J Microsc 226:182–189

Hohmann-Marriott MF, Sousa AA, Azari AA, Glushakova S, Zhang G, Zimmerberg J, Leapman RD (2009) Nanoscale 3D cellular imaging by axial scanning transmission electron tomography. Nat Methods 6:729–731

Hoppe W, Gassmann J, Hunsmann N, Schramm HJ, Sturm M (1974) Three-dimensional reconstruction of individual negatively stained yeast fatty-acid synthetase molecules from tilt series in the electron microscope. Z Physiol Chem 355:1483–1487

Hsieh YC, Athar M, Chaudry IH (2009) When apoptosis meets autophagy: deciding cell fate after trauma and sepsis. Trends Mol Med 15:129–138

Knoll G, Brdiczka D (1983) Changes in freeze-fractured mitochondrial membranes correlated to their energetic state dynamic interactions of the boundary membranes. Biochim Biophys Acta 733:102–110

Kremer JR, Mastronarde DN, McIntosh JR (1996) Computer visualization of three-dimensional image data using IMOD. J Struct Biol 116:71–76

Lang RD, Bronk JR (1978) A study of rapid mitochondrial structural changes in vitro by spray-freeze-etching. J Cell Biol 77:134–147

Liou W, Geuze HJ, Geelen MJH, Slot JW (1997) The autophagic and endocytic pathways converge at the nascent autophagic vacuoles. J Cell Biol 136:61–70

McDonald K (2007) Cryopreparation Methods for Electron Microscopy of Selected Model Systems. In: McIntosh JR (Ed) Cellular Electron Microscopy. (Method Cell Biol) Elsevier 79: 23–56

Midgley PA, Weyland M, Thomas JM, Johnson BFG (2001) Z-contrast tomography: a technique in three-dimensional nanostructural analysis based on Rutherford scattering. Chem Commun 10:907–908

Müller SA, Engel A (2001) Structure and mass analysis by scanning transmission electron microscopy. Micron 32:21–31

Péranzi G, Messaoudi C, Issop L, Lacapère JJ (2010) Electron microscope tomography of native membranes. In: (Lacapère Jean-Jacques. Ed) Membrane protein structure determination: methods and protocols. Methods in molecular biology, vol. 654. Springer, pp 221–235

Perkins GA, Tjong J, Brown JM, Poquiz PH, Scott RT, Kolson DR, Ellisman MH, Spirou GA (2010) The micro-architecture of mitochondria at active zones: electron tomography reveals novel anchoring scaffolds and cristae structured for high-rate metabolism. J Neurosc 30:1015–1026

Rabl R, Soubannier V, Scholz R, Vogel F, Mendl N, Vasiljev-Neumeyer A, Körner C, Jagasia R, Keil T, Baumeister W, Cyrklaff M, Neupert W, Reichert AS (2009) Formation of cristae and crista junctions in mitochondria depends on antagonism between Fcj1 and Su e/g. J Cell Biol 185:1047–1063

Sailer M, Höhn K, Lück S, Schmidt V, Beil M, Walther P (2010) Novel electron tomographic methods to study the morphology of keratin filament networks. Microsc Microanal 16:462–471

Schneider EM, Lorenz I, Müller-Rosenberger M, Steinbach G, Kron M, Janka-Schaub GE (2002) Hemophagocytic lymphohistiocytosis is associated with deficiencies of cellular cytolysis but normal expression of transcripts relevant to killer-cell-induced apoptosis. Blood 100:2891–2898

Seiler H (1967) Einige aktuelle Probleme der Sekundärelektronenemission. Z angew Phy 22:249–263

Studer D, Michel M, Müller M (1989) High pressure freezing comes of age. Scanning Microsc Suppl 3:253–268

Sun MG, Williams J, Munoz-Pinedo C, Perkins GA, Brown JM, Ellisman MH, Green DR, Frey TG (2007) Correlated three-dimensional light and electron microscopy reveals transformation of mitochondria during apoptosis. Nat Cell Biol 9:1057–1065

Van Driel LF, Valentijn JA, Valentijn KM, Koning RI, Koster AJ (2009) Tools for correlative cryo-fluorescence microscopy and cryo-electron tomography applied to whole mitochondria in human endothelial cells. Cell Biol 88:669–684

Walther P, Ziegler A (2002) Freeze substitution of high-pressure frozen samples: the visibility of biological membranes is improved when the substitution medium contains water. J Microsc 208:3–10

Walther P, Wehrli E, Hermann R, Müller M (1995) Double layer coating for high resolution low temperature SEM. J Microsc 179:229–237

Walther P, Höhn K, Krisp H (2009) What is the true size of the mitochondrial intermembrane space? A study using high-pressure freezing and STEM tomography. In: Pabst MA and Zellnig G (eds), Proceedings of MC2009, vol. 2 Life Science. Verlag der TU Graz, pp 49–50

Yakushevska AE, Lebbink MN, Geerts WJ, Spek L, van Donselaar EG, Jansen KA, Humbel BM, Post JA, Verkleij AJ, Koster AJ (2007) STEM tomography in cell biology. J Struct Biol 159:381–391

Zick M, Rabl R, Reichert AS (2009) Cristae formation–linking ultrastructure and function of mitochondria. Biochim Biophys Acta 1793:5–19

Zierold K, Steinbrecht A (1987) Cryofixation of diffusible elements in cells and tissues for electron probe microanalysis. In: Steinbrecht RA, Zierold K (eds) Cryotechniques in Biological Electron Microscopy. Springer, Heidelberg, pp 3–34